LBL-38165
UC-411

Lawrence Berkeley Laboratory
UNIVERSITY OF CALIFORNIA

CHEMICAL SCIENCES DIVISION

Quantum Effects in Unimolecular Reaction Dynamics

J.D. Gezelter
(Ph.D. Thesis)

December 1995

REFERENCE COPY
Does Not
Circulate
Bldg. 50 Library.
LBL-38165
Copy 1

Prepared for the U.S. Department of Energy under Contract Number DE-AC03-76SF00098

DISCLAIMER

This document was prepared as an account of work sponsored by the United States Government. While this document is believed to contain correct information, neither the United States Government nor any agency thereof, nor the Regents of the University of California, nor any of their employees, makes any warranty, express or implied, or assumes any legal responsibility for the accuracy, completeness, or usefulness of any information, apparatus, product, or process disclosed, or represents that its use would not infringe privately owned rights. Reference herein to any specific commercial product, process, or service by its trade name, trademark, manufacturer, or otherwise, does not necessarily constitute or imply its endorsement, recommendation, or favoring by the United States Government or any agency thereof, or the Regents of the University of California. The views and opinions of authors expressed herein do not necessarily state or reflect those of the United States Government or any agency thereof or the Regents of the University of California.

Quantum Effects in Unimolecular Reaction Dynamics

Joshua Daniel Gezelter
Ph.D. Thesis

Department of Chemistry
University of California

and

Chemical Sciences Division
Lawrence Berkeley National Laboratory
University of California
Berkeley, California 94720

December, 1995

This work was supported in party by the Director, Office of Basic Energy Sciences, Chemical Sciences Division of the U.S. Department of Energy under Contract No. DE-AC03-76SF00098, and in part by the National Science Foundation.

Quantum Effects in Unimolecular Reaction Dynamics

Copyright © 1995
by
Joshua Daniel Gezelter

The U.S. Department of Energy has the right to use this thesis for any purpose whatsoever including the right to reproduce all or any part thereof.

Abstract

Quantum Effects in Unimolecular Reaction Dynamics

by

Joshua Daniel Gezelter

Doctor of Philosophy in Chemistry

University of California at Berkeley

Professor William H. Miller, Chair

This work is primarily concerned with the development of models for the quantum dynamics of unimolecular isomerization and photodissociation reactions. We apply the rigorous quantum methodology of a Discrete Variable Representation (DVR)[1] with Absorbing Boundary Conditions (ABC)[2] to these models in an attempt to explain some very surprising results from a series of experiments on vibrationally excited ketene.[3] Within the framework of these models, we are able to identify the experimental signatures of tunneling and dynamical resonances in the energy dependence of the rate of ketene isomerization. Additionally, we investigate the step-like features in the energy dependence of the rate of dissociation of triplet ketene to form $^3B_1$ CH_2 + $^1\Sigma^+$ CO that have been observed experimentally. These calculations provide a link between *ab initio* calculations of the potential energy surfaces and the experimentally observed dynamics on these surfaces.

Additionally, we develop an approximate model for the partitioning of energy in the products of photodissociation reactions of large molecules with appreciable barriers to

1. D. T. Colbert and W. H. Miller, *J. Chem. Phys.* 97, 1982 (1992).
2. T. Seideman and W. H. Miller, *J. Chem. Phys.* 97, 2499 (1992).
3. E. R. Lovejoy and C. B. Moore, *J. Chem. Phys.* 98, 7846 (1993); S. K. Kim, E. R. Lovejoy, and C. B. Moore, *J. Chem. Phys.* 102, 3202 (1995).

recombination. In simple bond cleavage reactions like $CH_3COCl \rightarrow CH_3CO + Cl$, the model does considerably better than other impulsive and statistical models in predicting the energy distribution in the products.[1]

We also investigate ways of correcting classical mechanics to include the important quantum mechanical aspects of zero-point energy. The method we investigate[2] is found to introduce a number of undesirable dynamical artifacts including a reduction in the above-threshold rates for simple reactions, and a strong mixing of the chaotic and regular energy domains for some model problems.

We conclude by discussing some of the directions for future research in the field of theoretical chemical dynamics.

1. S. W. North, D.A. Blank, J. D. Gezelter, C. A. Longfellow, and Y. T. Lee, *J. Chem. Phys.* **102**, 4447 (1995).

2. J.M. Bowman, B. Gazdy, and Q. Sun, *J. Chem. Phys.* **91**, 2859 (1989); W. H. Miller, W. L. Hase, and C. L. Darling, *J. Chem. Phys.* **91**, 2863 (1989).

Dedication

To my parents,
Joseph and Diane Gezelter,

and to my wife,
Carey Gaudern.

Acknowledgments

I would like to thank my advisor, Professor William H. Miller for his guidance, his expertise, and for allowing me the opportunity to learn from one of the truly great minds in our field. Interacting with Professor Miller has been an exhilarating and humbling experience, and it has always been rewarding. I would also like to thank Professor C. Bradley Moore for providing the reasons that much of the research in this dissertation was carried out, Professor Robert G. Littlejohn for his insightful comments at my preliminary examination, and Professor Richard A. MacPhail at Duke University for sparking an interest in physical chemistry that has never waned. I would also like to thank the Oracle at Berkeley, Professor Robert Harris, for increasing my understanding of the world (although it often took me a while to realize what I had learned).

I have had the pleasure of knowing some extremely bright graduate students, post-docs and visiting faculty while in the Miller group. I would like to acknowledge the help, guidance and friendship of Prof. Scott Auerbach, Prof. Gerrit Grönenboom, Dr. Hans Karlsson, Prof. Claude Leforestier, Dr. Srihari Keshavamurthy, and Ward Thompson.

I would also like to thank various members of the Miller Group, past and present: Dr. Yan-Tyng "Sherry" Chang, Dr. Daniel Colbert, Åke Edlund, Dr. Lionel F.X. Gaucher, Dr. Tim Germann, Prof. Nick Handy, Dr. Rigoberto Hernandez, Dr. Stefan Krempl, Dr. Uwe Manthe, Dr. Camilla Minichino, Johannes Natterer, Pamela Ohara, Dr. Uri Peskin, Bill Poirier, Prof. Hannah Reisler, Dr. Peter Saalfrank, Dr. Guenter Schmid, Dr. Tamar Seideman, David Skinner, Kathy Sorge, Bruce Spath, Dr. Gerhard Stock, Sean Sun, Dr. Agathe Untch, Prof. David Wardlaw, and Dr. Joshua Wilkie for providing such a stimulating environment during my stay in Berkeley.

It is with great pleasure that I acknowledge Mrs. Cheryn Gliebe's friendship and assistance throughout my graduate career. I do not know what I would have done without her help.

Many thanks are due to my scientific partner-in-crime, Dr. Simon North, who created the position of "adjunct theorist" on his molecular beam machine and forced me to learn more about statistical models than I thought I wanted to know. I hereby designate Dr. North the "adjunct experimentalist" on my workstation, which will never need to have its skimmers aligned.

A number of other graduate student friends made Berkeley a wonderful place to grow intellectually. In alphabetical order, they are: Dr. Joel Bader, Dave Blank, Alan Bracker, Dr. John Gehlen, Nicola Hill, Dr. Eric Hiller, Marilyn Kamna, Dr. Michele McMahon Holcomb, Dr. Sang Kyu Kim, Dr. Ned Lovejoy, Dr. Chris Mundy, Dr. Phil Reilly, Dr. Tim Robinson, and Marc Schrier.

Thanks also to my friends on 'spaugh-net for being my closest friends, and for distracting me for hours on end when we all should have been working.

I would also like to acknowledge the organizations which provided funding for the research contained in this dissertation, and whose financial support made the completion of my doctoral research possible. In particular, I would like to thank the National Science Foundation for a graduate research fellowship, and much of this research has been supported by the Director, Office of Energy Research, Office of Basic Energy Sciences, Chemical Sciences Division of the U.S. Department of Energy under Contract No. DE-AC03-76SF00098.

Most of all, I must thank my family: My parents, Joseph and Diane Gezelter, for establishing my love of science, knowledge and learning; my siblings, Marcia and Lisa Gezelter, for putting up with their know-it-all brother; and my wife, Carey Gaudern, for everything that she is and does. They laid the foundation on which this thesis rests.

Table of Contents

Dedication v

Acknowledgements vii

Table of Contents ix

List of Figures xiii

List of Tables xv

CHAPTER 1. Introduction 1

1.1. A Philosophical Overview 1
1.1.1. The Creation of Scientific Models 2
1.1.2. A Reduction to the Essentials 3
1.2. Unimolecular Reactions 4
1.3. Theoretical Methods 6
1.3.1. Corrections to Classical Trajectory Methods 6
1.3.2. Quantum Reactive Scattering 7
1.3.3. Impulsive and Statistical Models 8
1.4. Overview of the Following Work 9

CHAPTER 2. On the Zero-Point Energy Problem 11

2.1. The origins of Zero-Point Energy 11
2.2. Using Classical Mechanics to study large systems 12
2.3. The ZPE Problem 13
2.3.1. Evidence for the problem 14
2.4. Proposed Solutions to the ZPE Problem 15
2.4.1. Partial ZPE inclusion methods 15
2.4.2. Trajectory rejection methods 16
2.4.3. Initial and Final state sampling methods 17
2.4.4. Dynamics-altering Methods 18
2.4.4.1. The Bowman-Miller-Hase (BMH) method 18
2.5. Undesirable dynamical effects - the Hénon-Heiles potential 23
2.5.1. Model and Methods 23
2.5.2. Results and discussion 26
2.6. Undesirable effects on observables: H + HF(v=2,3) -> F + H_2(v=0) 30
2.6.1. Model and Methods 30
2.6.2. Results and Discussion 33
2.6.3. Future directions for the BMH model 36
2.7. Other Dynamics-Altering Methods 40
2.8. Conclusions 42

CHAPTER 3. **Resonant Features in the Energy Dependence of the Rate of Ketene Isomerization** 43

3.1. Introduction 43
3.2. Summary of Theoretical and Computational Specifics 47
3.2.1. The Cumulative Reaction Probability 47
3.2.2. The Potential Energy Surface 49
3.2.3. Absorbing Boundary Conditions 53
3.2.4. The Basis Set 54
3.2.5. Evaluation of the Trace 56
3.2.6. Methods for Solving Sparse Linear Systems 57
3.3. Results 61
3.3.1. Isomerization Rate using one degree of freedom 61
3.3.2. Isomerization Rate using two degrees of freedom 63
3.3.3. Isomerization Rate using three degrees of freedom 66
3.4. Discussion 68

CHAPTER 4. **Dynamics of the Photodissociation of Triplet Ketene** 71

4.1. Introduction 71
4.2. Summary of Theoretical and Computational Specifics 75
4.2.1. The Potential Energy Surface 75
4.2.2. The coordinate system 79
4.2.3. The Basis Set 81
4.2.4. Evaluation of the Trace 82
4.2.5. Hindered Internal Rotation 84
4.3. Results 87
4.3.1. One degree of freedom 88
4.3.2. Two degrees of freedom 92
4.4. Discussion 92

CHAPTER 5. **The Barrier Impulsive Model: A new method for predicting the distribution of energy in photodissociation reactions** 95

5.1. Introduction 95
5.2. The Impulsive Model 98
5.2.1. The Soft Fragment Limit 99
5.2.2. The Rigid Fragment Limit 102
5.2.3. Modified Impulsive Models 103
5.3. Statistical Models 104
5.3.1. A new statistical method for partitioning fragment energy 105
5.4. The Barrier Impulsive Model 109
5.5. Results and Discussion 109
5.5.1. Acetone Dissociation 110
5.5.2. Acetic Acid Dissociation 112
5.6. Conclusions 113

CHAPTER 6. Concluding Remarks 115

6.1. The Zero-Point Energy Problem 115
6.2. The Unimolecular Reactions of Ketene 116
6.3. The Barrier Impulsive Model 118
6.4. Future Directions 119
6.4.1. On Potential Energy Surfaces 119
6.4.2. Approximate Theories 120
6.4.3. Reduced Dimensionality Models 121

Bibliography 123

List of Figures

CHAPTER 1. 1

CHAPTER 2. 11

Figure 2-1. Schematic illustrating the BMH method 19
Figure 2-2. The BMH method's effects on harmonic mode energies 27
Figure 2-3. The BMH method's effects on the power spectrum. 28
Figure 2-4. How BMH effects trajectories 29
Figure 2-5. The BMH results for the $P_{3,0}$ 33
Figure 2-6. The BMH results for $P_{2,0}$ 34
Figure 2-7. The BMH results for $P_{n,0}$ 35
Figure 2-8. Sketch of the BMH barrier crossing problem 36
Figure 2-9. Zero Point Corrections for the Eckart Barrier 37
Figure 2-10. Zero Point corrections for a Realistic Barrier 38
Figure 2-11. Sketch of the TRAPZ constraint method 41

CHAPTER 3. 43

Figure 3-1. Sketch of the energetics along the reaction coordinate 45
Figure 3-2. The 1-d potential energy surface 50
Figure 3-3. 1-d $N(E)$ 62
Figure 3-4. 1-d $k_{iso}(E)$ 63
Figure 3-5. 2-d potential energy surface 64
Figure 3-6. 2-d $k_{iso}(E)$ 65
Figure 3-7. 2-d $k_{iso}(E)$ 66
Figure 3-8. 3-d $k_{iso}(E)$ 67

CHAPTER 4. 71

Figure 4-1. The energetics of the ketene dissociation experiments 73
Figure 4-2. The coordinate system for ketene triplet dissociation 77
Figure 4-3. $N_{1d}(E)$ for ketene triplet dissociation 88
Figure 4-4. The one-dimensional $k_d(E)$ for ketene triplet dissociation 90
Figure 4-5. The effect of lowering the barrier frequency 91
Figure 4-6. The 2-D surface for ketene triplet dissociation 93
Figure 4-7. The two-dimensional $k_d(E)$ for ketene triplet dissociation 94

CHAPTER 5. 95

Figure 5-1. Sketch showing the energetic reservoirs. 97
Figure 5-2. Sketch of the masses involved in the Soft-fragment impulsive model 101

Figure 5-3. Energy partitioning in the statistical reservoir 106
Figure 5-4. Comparison with other impulsive and statistical theories 111

CHAPTER 6. 115

List of Tables

CHAPTER 1. 1

CHAPTER 2. 11

Table 2-1. LEPS parameters for the M5 surface 31

CHAPTER 3. 43

Table 3-1. Properties of the best-fit 1-d potential surface 52
Table 3-2. Parameters of the best-fit potential energy surface..... 53
Table 3-3. Parameters of the Absorbing potential 55

CHAPTER 4. 71

Table 4-1. Energies and frequencies for the critical points along the reaction coordinate. Energies are relative to the transition state structure 78
Table 4-2. Parameters of the best-fit potential energy surface..... 79
Table 4-3. Parameters used in the calculation of hindered internal rotation energy levels of the transition state. 87
Table 4-4. The *ab initio* Vibrational frequencies of the C_s^{II} transition state.. 89

CHAPTER 5. 95

Table 5-1. Comparison of theoretical predictions to experiments on Acetic Acid photodissociation 113

CHAPTER 6. 115

1 Introduction

1.1. A Philosophical Overview

Theoretical chemistry presents a very different approach to the scientific method than is practiced in other parts of the scientific food chain. Theoretical Biology and Physics share a reductionist approach to theory construction. Theorists in these fields develop theories whose entities exist on a smaller level than the observations carried out by the experimentalists in their fields. This way of making theories has had great success, particularly with quantum mechanics and with the molecular biological model for how living things work.

Theoretical chemistry presents a different set of problems. We already have a theory that we believe to be "right" (quantum mechanics) and it works on a microscopic scale relative to the things that experimental chemists measure. Unfortunately, at the level of complexity of many atoms and molecules, quantum mechanics (although it is the "correct" theory) is not a particularly "good" theory for chemical dynamics. I say this because it doesn't allow for a simple understanding of how the chemical reactions work, and because it can't give predictions in a reasonable amount of time and/or effort for systems with more than a moderate number of degrees-of-freedom.

We also have at our disposal the "wrong" theory (classical mechanics) which can be used for complex systems. This is also not a particularly "good" theory for chemical dynamics; although it provides a means of understanding the phenomena being observed, and predictions can be made with a reasonable amount of time and effort, the predictions are simply wrong when compared to experimental evidence.

So, theoretical chemists are stuck with two theories that are lacking for very different reasons. The compromises that seem to be working themselves out as the primary occupation of theoretical chemists are 1) reduced-dimensionality or "model" systems for chemical processes, and 2) hybrid theories for systems in their full dimensionality. The work in this dissertation is primarily concerned with the first of these approaches, and it will be helpful to review the positions of some philosophers of science who have had (somewhat controversial) things to say about this approach.

1.1.1. The Creation of Scientific Models

Nancy Cartwright touches on the subject of model building in her book "How the Laws of Physics Lie". [3] Like many philosophers, she takes an extreme position; nature is fundamentally messy and intractable to scientific model-building, so all scientific models are merely useful fictions. Constructing models, according to Cartwright, is a balancing act; the more general your model is, the more idealizations you have to make, so the further it is from applying to any real-world situations. And Cartwright extrapolates this all the way down to quantum mechanics, which is very general, but is still a useful fiction or a "big lie."

So Cartwright would say that the field of theoretical chemical dynamics just brings a universal feature of scientific theories to the fore. In any field, scientists balance generality with applicability when they're constructing models; it's just more evident in theoretical chemistry. (Physicists, according to Cartwright, don't realize this is what they're doing.) She would say that what makes one model better than another is purely a pragmatic thing which depends upon what kind of understanding is sought from the theory. Sometimes you want a very general framework that's applicable to a whole range of situations. Sometimes you want a very particular model that just applies to one or two situations, but applies very straightforwardly. And neither is "better" or "more fundamental" or "a more accurate description of the world."

I'd like to take exception with Cartwright's position that since all theories are useful fictions, they are all equivalently false descriptions of the inner workings of the natural

world. I'd like to think that a full quantum mechanical treatment of the systems we deal with is a better and more fundamental description of the world than a reduced-dimensionality treatment. This is not to say that model building is a less important part of science, however. It does, after all, make up a large part of this dissertation. I find myself agreeing with Ian Hacking when he argues that model building is the *fundamental* step in doing science. [4] That is, theories are always too complex for us to discern their consequences, so we simplify them in mathematically tractable models. He conceives of models as the comprehensible intermediaries between incomprehensible phenomena and inapplicable theories; the aim of science is not a theory of everything which is *true*, but a plethora of usable models which *approximate* the truth.

1.1.2. A Reduction to the Essentials

In the early 1980's the debate in the philosophy of science shifted from an argument over reductionism to a pitched battle between *realists* who think that scientific theories and entities have real physical significance [5] and the *empiricists* who believe them to be simply useful fictions without any truth value. [6, 3] The original debate was probably more fruitful for those of us who participate in doing the science, however. Is a theory of biological life that requires knowledge of subatomic particles a useful theory? Or is this reduction necessary for understanding the phenomena? Can explanations of observable phenomena really be reduced to a small number of "essentials"?

These questions are answered in the affirmative by most theoretical chemists. We have had great success in using quantum mechanics to connect observable phenomena to potential energy surfaces that are obtained from first principles. This is reductionism in one of its purest and most successful forms. Starting at the bottom with particles and a general theory like quantum mechanics, we are able to make predictions about observable phenomena.

In his Ph.D. thesis, Scott Auerbach argued for a strongly reductionist view of science with one major exception; he claimed that he could not conceive of *himself* as "nothing more than a bag of particles," [7] and took an anti-reductionist position of the biological

sciences for this reason. If nothing else, the work carried out in this dissertation will show that even exceedingly small "bags of particles" can exhibit rich behaviors under the right conditions. I find myself taking this as support for a much stronger reductionist view of science; I do not conceive of myself as a bag of particles, but feel that *what I am* is simply the *behaviors* exhibited by a very complex bag of particles, and is not the particles themselves. The essential aspects of biological systems may be at the particle level, but the behavior exhibited by the particles is not necessarily simple. This is an important philosophical distinction, and one that allows me to maintain simultaneously the strong reductionist position and a sense of wonder about human intelligence.

1.2. Unimolecular Reactions

A large portion of our understanding of the dynamics of chemical reactions has been a consequence of the development of crossed molecular beam techniques. [8] In a molecular beam experiment, the reactants are prepared in known internal states, and the internal states and translational energy distributions of the products are measured at a variety of scattering angles, yielding the differential cross section, which is the most detailed information we can hope to obtain for a bimolecular reaction.

Quantum effects have been observed relatively few times in molecular beam studies. In a set of experiments, Neumark *et al.* [9] were able to use crossed molecular beams to observe resonances in a scattering experiment on the $F + H_2$ reaction. In general, however, it is nearly impossible to control the impact parameter between the colliding reactant molecules, and the wide range of impact parameters has the effect of averaging the cross section over a distribution of values of the total angular momentum. This can often obscure the experimental signatures of interesting quantum effects like resonances.

Unimolecular reactions, however, can be prepared in well-defined initial states with very cold rotational distributions. This allows the experimental chemist to obtain extremely detailed information about the reaction. Indeed, C. Bradley Moore's group has prepared ketene and formaldehyde molecules in nearly mono-energetic distribu-

tions with rotational temperatures at or below 4 K, and has measured detailed product-state distributions for the photodissociation reactions of these molecules.

Much of the work presented in this dissertation is carried out to explain the results of some of the Moore group's experiments on ketene. [10, 11, 12, 13, 14, 15, 16, 17, 18, 19] In particular, we try to explain a series of observations of what appear to be resonances in the energy dependence of the rate of ketene isomerization. We also investigate a series of steps in the dissociation rate of ketene on the triplet surface that look like they are coming from quantized levels at the transition state. In both of these experiments, vibrationally excited (but rotationally cold) ketene molecules were prepared by exciting ketene from the ground state surface to the first excited singlet electronic surface. The system then undergoes internal conversion or intersystem crossing onto the ground state and first excited triplet surfaces, and the reaction proceeds. The products of the dissociation are measured by laser-induced fluorescence (LIF) of the CH_2 or CO fragments.

The unimolecular reactions of ketene happen at energies very far above the ground state energy of the ketene molecule. In the limit that the energy is rapidly randomized between the available vibrational modes, we can treat the arrival at and passage through the transition state statistically. [20, 21, 22, 23] The rate constant when the reaction is carried out at total energy E with angular momentum J is given by

$$k(E,J) = \frac{N(E,J)}{h\rho(E,J)}, \tag{1-1}$$

where $\rho(E,J)$ is the reactant density of states, $N(E,J)$ is the cumulative reaction probability at the transition state, and h is Planck's constant. In most statistical theories, $N(E,J)$ is taken to be the number of orthogonal ro-vibrational levels at the transition state with energy less than E. Differing statistical theories make different assumptions about $N(E,J)$, which contains all of the dynamics of the reaction. What we attempt to do in our calculations is to obtain $N(E,J)$ quantum mechanically, in as rigorous a fashion as possible.

Ketene has 9 vibrational degrees of freedom, and the current computational limit on quantum dynamics calculations is around 6 coupled degrees of freedom. We must therefore make the simplifying assumption that some of the vibrational degrees of freedom are uncoupled from the rest. This is often called the reduced-dimensionality approximation, [24] and if taken to the limiting case where *all* vibrational modes are decoupled from the reaction coordinate, we recover the one-dimensional tunneling corrections to microcanonical transition state theory, [25] where we approximate the cumulative reaction probability,

$$N(E,J) \approx \sum_{n} P\left(E - \varepsilon_{\underset{\sim}{n}}^{\ddagger}, J\right), \tag{1-2}$$

where E is the total energy of the molecule, $\varepsilon_{\underset{\sim}{n}}^{\ddagger}$ is the energy level of the transition state with quantum numbers $\underset{\sim}{n}$, and $P(E,J)$ is the one-dimensional tunneling probability along the reaction coordinate. The reduced dimensionality approximation is used extensively in Chapters 3 and 4 of this dissertation.

1.3. Theoretical Methods

The calculations presented in this dissertation stand on the shoulders of a large body of theoretical methodology. It will be useful to review briefly some of these methods before forging ahead.

1.3.1. Corrections to Classical Trajectory Methods

Classical trajectories have long been used to study the dynamics of chemical reactions.[1] One of the unfortunate limitations of using classical trajectories is that they cannot replicate tunneling, resonance, and interference effects that are inherently quantum phenomena. Another similar limitation is that trajectories can have less than the zero-point vibrational energy in the vibrational modes. This subtle problem has been addressed in recent years in simultaneous papers by Bowman *et al.* [26] and Miller, Hase, and Darling. [27] Their method for correcting zero-point energy involves a local normal-mode

1. For good reviews of classical trajectory methods, see Refs. 1 and 2.

expansion about the instantaneous location of the trajectory on the potential energy surface. If the trajectory falls below the zero-point energy in any of these vibrational modes, the momentum in that mode is reversed, effectively keeping the trajectory out of the "forbidden" ($n < 1/2$) region. Although their method was tested extensively for bound systems, it has never (to our knowledge) been used in a trajectory simulation of a reactive chemical system. For this reason, we wanted to investigate how this method would compare to reaction probabilities calculated using un-modified classical trajectories as well as a fully quantum mechanical treatment.

1.3.2. Quantum Reactive Scattering

Until very recently, problems in gas phase chemistry involving quantum scattering were solved using techniques based on one of the well-known propagation methods for elastic or inelastic scattering, [28] or via the Kohn variational principle (KVP) for reactive scattering. [29, 30] The problem with using the KVP method for the kind of unimolecular reactions carried out by Moore's group is that it requires a basis set expansion in the reaction coordinate. At the energies of interest, ketene has millions of available vibrational levels in both the reactant and product regions, which would make the calculation of reaction probabilities using the KVP method impractical.

A number of recent developments made by Miller and co-workers have allowed us to concentrate on the region immediately surrounding the transition state; we can now calculate the reaction probability directly, i.e. without having to obtain the immense number of state-to-state reaction amplitudes that make up the scattering matrix (the S-matrix). Seideman and Miller [31] developed a formalism for obtaining the cumulative reaction probability (CRP) using absorbing boundary conditions (ABCs). The ABCs are negative imaginary potentials added to the Hamiltonian just outside the interaction region. They allow us to construct a Green's function which has the correct outgoing wave boundary conditions by absorbing the flux that leaves the barrier region. This is really the piece of theoretical methodology that made calculating rates for ketene isomerization a feasible undertaking.

A discrete variable representation (DVR) basis set developed by Colbert and Miller [32] allows for further advances in calculating the reaction probabilities in multiple degrees-of-freedom. The matrix representation of the multi-dimensional Hamiltonian is sparse in a DVR, [33, 34] and the integrals required to construct this matrix representation are analytic. This allows us to construct the Hamiltonian for a very large problem "on-the-fly" and using a minimal amount of computer storage. Since the Green's function is the inverse of $E\underset{\sim}{I} - \underset{\sim}{H} + i\underset{\sim}{\epsilon}$, we can use one of a number of algorithms for inverting sparse linear systems. The efficient solution of sparse linear systems is a small industry in the applied mathematics community, and a number of techniques have been recently developed that are quite good at inverting the Hamiltonian matrices we create. Among them are the GMRES [35] and QMR [36] algorithms, which are used extensively in the following chapters.

Manthe and Miller [37] introduced a reaction probability operator, $\hat{P}(E)$, which has only a few non-zero eigenvalues which correspond to the reaction probabilities for individual vibrational levels of the transition state. The cumulative reaction probability is simply the trace of $\hat{P}(E)$, or the sum of these eigenvalues (the "eigenreactionprobabilities"), and all of the closed channels at the transition state correspond to eigenvalues of $\hat{P}(E)$ which are equal to 0. This discovery was quite advantageous, as we need only find the non-zero eigenvalues of $\hat{P}(E)$ to obtain the cumulative reaction probability. This task is ideally suited to an iterative Lanczos diagonalization technique, [38, 39, 40] which converges the outlying eigenvalues very rapidly. Using $\hat{P}(E)$ can save one or two orders of magnitude in the amount of computer time required to obtain the CRP.

1.3.3. Impulsive and Statistical Models

Two easily-applied theories are in widespread use by experimental chemists who want to model the partitioning of the total available energy in photodissociation reaction. The first of these, the impulsive model, [41, 42] uses all available energy in an impulsive kick that is applied along the bond that is being severed. Conservation of energy, linear momentum, and angular momentum allows one to easily predict the amount of energy in the rotational, vibrational, and translational degrees of freedom of the fragments. The

impulsive model tends to overestimate the translational energy of the fragments when the available energy is in excess of the barrier to recombination.

The other set of theories that are in common use are usually applied to reactions which have small (or no) barriers to recombination. The simplest of these is the prior distribution [43] which assumes that all energetically accessible product states are equally probable. When the conservation of angular momentum of the products is taken into account, the result is phase space theory (PST). [44] Both of these theories tend to overestimate product rotational excitation above the vibrational threshold while underestimating product vibrations. The separate statistical ensembles theory (SSE) [45] attempts to correct these deficiencies by using some of the information about energy partitioning in the parent molecule to obtain product state partitioning.

In Chapter 5, we will present a single theory that unifies the essential aspects of both the impulsive model (for energies near the top of the barrier) and the best of the statistical models (for energy in excess of the barrier height). We will require the theory to be easily applicable to molecules of appreciable size, so it must utilize information that is commonly available for these reactions; namely the energies, frequencies, and geometries of the parent molecule, the transition state, and the fragments.

1.4. Overview of the Following Work

Chapter 2 details our investigation of a technique for modifying classical equations of motion to correct for the zero-point energy problem. We look at what this technique does to the dynamics of the Hénon-Heiles Hamiltonian, [46] as well as to the state-to-state reaction probabilities for the $H + HF(v=2,3) \rightarrow F + H_2(v=0)$ reaction, comparing various properties of the dynamics to quantum and un-modified classical calculations in both systems.

Chapters 3 and 4 concentrate on reduced-dimensionality (but rigorous and fully quantum mechanical) models for two fascinating unimolecular reactions of ketene. Chapter 3 is an investigation of resonance structure in the energy dependence of the rate of

ketene isomerization via the oxirene intermediate, and the dissociation of triplet ketene to form $^3B_1\ CH_2 + {}^1\Sigma^+\ CO$ is discussed in Chapter 4. These reactions provided a good test of the methodology discussed above. Indeed, it would have been nearly impossible to calculate quantum mechanical reaction rates for these reactions without some of the advances mentioned in Section 1.3.2.

A new method for predicting the distribution of energy in photodissociation reactions is developed in Chapter 5. Briefly stated, the theory combines an impulsive model [41, 42] using the height of the exit barrier as the size of the impulse reservoir and a statistical model for the rest of the available energy. Contributions to the average product rotational, translational and vibrational energy are calculated for each reservoir, and are combined to give totals for each fragment of the dissociation event. The statistical reservoir is divided using a method similar in character to the separate statistical ensembles (SSE) method [45] which has been modified to handle very large parent molecules and fragments.

Finally, we conclude the dissertation in Chapter 6 with a summary of the previous chapters, and with suggestions for future work.

2 On the Zero-Point Energy Problem

Abstract

A series of calculations is presented which compare the traditional quasiclassical trajectory method for calculating chemical properties (reaction probabilities, IVR rates) for some model systems (the Hénon-Heiles Hamiltonian and the H + HF $\rightarrow$ H_2 + F reaction) with the Bowman-Miller-Hase (BMH) method which constrains trajectories so that they maintain zero-point energy in all vibrational modes. Calculations using both methods are compared to exact quantum calculations of the same properties, and the BMH method is found to introduce serious errors into the dynamics as well as into the averaged properties for ensembles of constrained trajectories. A number of other possible solutions to the zero-point energy problem are also discussed.

2.1. The origins of Zero-Point Energy

Zero-point energy can best be understood as a consequence of the Heisenberg uncertainty principle. When a particle is localized in a potential well of length a, it must have a momentum uncertainty of $\Delta p \geq \pi\hbar/a$, giving a kinetic energy of $E \sim (\Delta p)^2/(2m)$, which can be thought of as the zero-point energy for a particle in a box. Baym [48] argues that zero-point energy is why Helium remains a liquid at temperatures near absolute 0. Solid Helium would require the individual atoms to be localized in a lattice, and since the masses are so small, the resulting zero-point energy would overcome the relatively weak attractive forces between the atoms.

In a harmonic oscillator, the total energy can be expressed as $(p^2/2m) + (kx^2/2)$. A state with zero energy would require that the expectation values of $\hat{P}^2$ and $\hat{X}^2$ be simul-

taneously zero. The problem with this becomes apparent if one re-derives the uncertainty principle from the Schwartz Inequality,

$$\langle |(\Delta\hat{X})^2| \rangle \langle |(\Delta\hat{P})^2| \rangle \geq |\langle |\Delta\hat{X}\Delta\hat{P}| \rangle|^2 , \tag{2-1}$$

where $\Delta\hat{A} \equiv \hat{A} - \langle |\hat{A}| \rangle$. (Here, $| \rangle$ symbolizes an arbitrary ket.) Since an eigenstate of a harmonic oscillator centered around $x=0$ will have $\langle |\hat{X}| \rangle = 0$ and $\langle |\hat{P}| \rangle = 0$, Eq. 2-1 simplifies to

$$\langle |\hat{X}^2| \rangle \langle |\hat{P}^2| \rangle \geq |\langle |\Delta\hat{X}\Delta\hat{P}| \rangle|^2 . \tag{2-2}$$

If the right hand side of Eq. 2-2 is expressed in terms of the commutator and anticommutator for X and P, we have [49]

$$\langle |\hat{X}^2| \rangle \langle |\hat{P}^2| \rangle \geq \frac{1}{4}|\langle |[\hat{X}, \hat{P}]| \rangle|^2 + \frac{1}{4}|\langle |\{\Delta\hat{X}, \Delta\hat{P}\}| \rangle|^2 . \tag{2-3}$$

Both terms on the right side of the inequality are real and positive, so the uncertainty relation,

$$\langle |\hat{X}^2| \rangle \langle |\hat{P}^2| \rangle \geq \frac{1}{4}|\langle |[\hat{X}, \hat{P}]| \rangle|^2 = -\frac{1}{4}(-i\hbar)^2 = \frac{\hbar^2}{4} , \tag{2-4}$$

holds.

It is easy to see that if the expectation values of $\hat{P}^2$ and $\hat{X}^2$ are simultaneously zero, the uncertainty relation will be violated. The minimum uncertainty product allowed by Eq. 2-4 requires a state which has an energy of $E_0 = \hbar\omega/2$, the zero-point energy for the harmonic oscillator.

2.2. Using Classical Mechanics to study large systems

Quantum mechanical calculations of chemical properties (state-to-state reaction probabilities, cross sections, and thermal rates) for systems of N atoms require matrix diago-

nalizations (which scale with N^3) or inversions (which scale with N^2). These scaling laws make quantum calculations impractical for obtaining chemical information from systems with more than a few atoms. One way of getting around this limitation is to average the results from ensembles of classical trajectories, making the initial ensemble resemble the initial quantum state as closely as possible.

The traditional way of performing a classical trajectory simulation of a simple reaction

$$A + BC\,(v_i = 0) \rightarrow AB\,(v_f) + C \tag{2-5}$$

(where the reactant BC is started in its ground vibrational state) is to place an amount of energy in the vibration of BC that is equal to the zero-point energy of an equivalent quantum mechanical harmonic oscillator. The phase of this oscillation is sampled randomly, and the resulting distribution is called the "quasiclassical" distribution, which corresponds to a microcanonical distribution of initial conditions sampled from a ring in the phase space of that vibrational mode. A trajectory is run for each set of initial conditions and after some amount of time (or when the trajectory reaches a fixed separation between the atom and diatom), the final positions and momenta are placed in one of a set of "bins" which correspond roughly to the nearest quantum vibrational state of the product diatom. This allows for easy computation of state-to-state reaction probabilities using an ensemble of classical trajectories instead of a fully quantum mechanical treatment.

2.3. The ZPE Problem

The problem with using classical trajectories to simulate chemical reactions is that classical mechanics does not capture the "correct" physics of chemical processes. Tunnelling, resonance and interference effects are obvious examples of phenomena that are not observed in classical mechanics. A more subtle, but equally troublesome error shows up because classical mechanics allows trajectories to sit near the bottom of a potential well with no momentum in that degree of freedom. The "zero-point energy problem" is that the energy in some vibrational modes may fall below the quantum zero-point energy

($\frac{1}{2}\hbar\omega_k$ where ω_k is the harmonic frequency for mode k). This may not seem like a problem, but in a medium size polyatomic molecule like benzene the zero-point energy is a considerable amount of energy (52.2 kcal/mol). It becomes a serious problem when the molecule has a number of stiff modes with considerable zero-point energy which can then pool into one weak bond, thereby breaking the bond when the molecule may have a true (quantum) ground vibrational state.

The zero-point energy problem is also apparent in the energy dependence of microcanonical reaction probabilities. Classical trajectories do not have to maintain zero-point energy in vibrational modes that are perpendicular to the reaction coordinate at the transition state, so the energy from those modes may pool into the reaction coordinate itself, thereby lowering the effective energy threshold for the reaction. This effect is clearly shown in state-to-state reaction probabilities for $H + HF \rightarrow H_2 + F$ (cf. Fig. 2-7).

When the chemical property being calculated is the rate at which intramolecular vibrational energy redistribution (IVR) takes place, then an exchange of energy between vibrational modes that leaves one of the modes below it's zero-point vibrational energy will give spurious results for the rate of energy transfer.

2.3.1. Evidence for the problem

A number of studies have revealed these limitations in great detail. Guan *et al.* [50, 51] added differing fractions of the total zero-point energy to their trajectory studies of near-threshold overtone-excitation-induced photodissociation of H_2O_2. In their calculations, trajectories which started with zero-point energy in all modes and had the OH local mode excited to $\nu_{OH} = 5$ had a total energy in excess of the barrier to O-O bond fission. Experiments by Crim *et al.*, [52, 53] however, show that excitation of $\nu_{OH} = 5$ alone provides insufficient energy to cross the barrier. Guan *et al.* found a significant dependence of the classically calculated dissociation rates on the fraction of total zero-point energy included in the initial conditions, but inclusion of the full zero-point energy gave poor agreement with the experiments.

Lu and Hase [54] have noticed poor IVR in classical trajectory studies of Benzene when the trajectories are started with zero-point energy in all vibrational modes. In particular, stiff vibrational modes with a large amount of vibrational energy quickly (within 0.3 ps) transferred much of this energy to "floppy" vibrational modes. This flow of energy is obviously incorrect from a quantum mechanical viewpoint.

In a paper on the dynamics of Ethyl radical decomposition, Hase and Buckowski [55] argued that classical unimolecular dissociation rates can yield "exploding ground states". Below the quantum barrier to dissociation, the zero-point energy from other vibrational modes can pool into the reaction coordinate, yielding classical rates that indicate dissociation below the quantum threshold. Although no trajectories were run to test this hypothesis, classical and quantum RRKM [56, 57, 58, 59] calculations showed a strong divergence of the classical and quantum dissociation rates below the quantum threshold.

2.4. Proposed Solutions to the ZPE Problem

A number of strategies have evolved for fixing the zero-point energy problem. These strategies can be divided roughly into two classes. The first class seeks modifications to initial state or final state sampling of trajectories while leaving the classical evolution of the trajectories alone. These are the "passive" methods for dealing with the ZPE problem, which are discussed in the Sections 2.4.1 through 2.4.3.

The other class of methods are the "active methods" which seek to modify the classical equations of motion to take zero-point energy into account at every point along the trajectory. One active method in particular (the BMH method) is detailed in Section 2.4.4. Some problems with this method are discussed in Sections 2.5 and 2.6. A more recently developed active method is discussed in Section 2.7.

2.4.1. Partial ZPE inclusion methods

Lu and Hase [60] studied the effect of zero-point energy in calculations of the C-H overtones following excitation of a C-H local mode in Benzene. Their method for dealing

with the ZPE problem was to include a fraction of the zero-point energy ($0 \leq f_{zpe} \leq 1$) in the vibrational modes of the system. The calculated linewidth was less than 1.0 cm^{-1} for $f_{zpe}=0$, regardless of which overtone state was sampled. Using $f_{zpe}=0.04$ gave results in good agrement with experiments for the n=3 state. Larger values of f_{zpe} yielded linewidths an order of magnitude larger than experimental values.

Additional calculations were performed where zero-point energy was excluded from some of the normal modes. By excluding zero-point energy from the initial conditions of the seven normal modes with strong CCH bending character and retaining the zero-point energy in the initial conditions of the other 14 modes, Lu and Hase observed a significant decrease in the calculated linewidth. The linewidth decreased by a factor of 3 to 5 when compared to the trajectories which were started with zero-point energy in all vibrational modes, depending on which overtone was excited. In contrast, excluding the zero-point energy from the initial conditions of the other 14 modes while adding it to the seven CCH bending modes gave linewidths that were nearly identical to the full-ZPE initial conditions. Lu and Hase also suggested another passive method for correcting the zero-point energy problem based on initial state sampling from the Wigner distribution. This approach will be discussed in greater detail in Section 2.4.3.

2.4.2. Trajectory rejection methods

Another passive method was investigated by Nyman and Davidsson [61] as part of a trajectory study on the reaction $O\left({}^3P\right) + OH\left({}^2\Pi\right) \rightarrow O_2\left({}^3\Sigma_g^-\right) + H\left({}^2S\right)$. The initial conditions for the trajectories were started with either all or none of the zero-point energy in the OH vibration, and trajectories were propagated classically. Once the trajectories had completed, those which had less than the zero-point energy in the O_2 products (or OH reactants if the trajectory was non-reactive) were selectively "thrown out" or removed from ensemble of trajectories used for calculating various properties of the reaction.

The criteria for rejecting a trajectory were also the subject of study by Nyman and Davidsson, and was allowed to range from retaining all trajectories regardless of vibra-

tional energy to throwing out all those trajectories that completed with less than the zero-point energy. The results showed a strong dependence on which scheme of categorizing the trajectories was employed, and the treatment that yielded the best agreement with experiment varied considerably with which properties were being compared.

2.4.3. Initial and Final state sampling methods

As mentioned above, Lu and Hase [60] suggested that since such a small fraction of the zero-point energy gave the best agreement between experiments and the trajectory simulations, the important regions of phase space for the vibrational modes are those with bond distances closest to the bottom of the well and with $p \approx 0$. This corresponds quite well to the *quantum* ground-state vibrational distribution in both p and x. The quasiclassical initial conditions that are employed in traditional trajectory simulations sample from a ring outside of these maxima in the quantum distribution. What was sought was a distribution of initial conditions for an ensemble of trajectories that closely resembled the distribution of p and x in the quantum ground-state distribution.

The Wigner distribution,

$$\Gamma_W(p, q) = \frac{1}{(2\pi\hbar)^n}\int ds^n e^{-2ips/\hbar}\rho\,(q-s, q+s)\ , \tag{2-6}$$

has already proven itself very useful as a distribution function for initial conditions in a large number of calculations of various chemical properties for simple systems. [62, 63, 64, 65] (In Eq. 2-6, ρ is the density matrix for the appropriate vibrational degree-of-freedom.) Brown and Heller [62] found that agreement between quantum calculations of cross sections for the collinear dissociation of ICN(0,0) into $I\left({}^2P_{3/2}\right)$ and $CN\left({}^2A\pi_i\right)$ with classical trajectories started with a Wigner distribution of initial conditions was substantially better than agreement obtained using the corresponding quasiclassical distribution.

There are two problems with using a Wigner distribution for initial conditions. Although the Wigner distribution is real, it can be negative, which means interpreting

it as a distribution function for initial conditions can be problematic. This limitation can be removed by using Husimi's distribution function, [66]

$$\Gamma_H(p, q) = \frac{1}{\pi\hbar}\int dp'dq' exp\left(-\frac{(q-q')^2}{\hbar w^2} - w^2\frac{(p-p')^2}{\hbar}\right)\Gamma_W(p', q') \tag{2-7}$$

where w is the width of the uncertainty in the position coordinate, q.

The other limitation of using either the Wigner or Husimi distribution functions is that the quantum mechanical wavefunction for a smaller (but still appreciable) system must be calculated to obtain the distribution functions for large reactions. For example, suppose one wishes to perform a trajectory simulation of an atom colliding with a vibrating 5-atom molecule. A Wigner or Husimi initial state distribution for the trajectories requires the ground-state vibrational wave function for the entire reactant molecule (a system with 9 degrees of freedom). This defeats the main advantage of classical trajectory simulations which is the linear scaling behavior with increasing numbers of atoms. If one wishes to study the dynamics of large systems it is unlikely that using initial conditions sampled from the Wigner or Husimi distributions will be of great utility.

2.4.4. Dynamics-altering Methods

The other class of methods that have been proposed for dealing with the zero-point energy problem introduce new ways of integrating the equations of motion in order to preserve the zero-point energy at every point along the trajectory. These "active" methods attempt to replace classical mechanics with a dynamical method that has a more "global" view of the potential energy surface, and typically require second derivatives of the potential energy surface at each point along the trajectory.

2.4.4.1. The Bowman-Miller-Hase (BMH) method

One active method was proposed simultaneously by Bowman *et al.* [26] and Miller, Hase, and Darling [27] and will hereafter be referred to as the BMH method. The BMH method operates on the principle that trajectories should be kept out of the forbidden ($n < 1/2$) region of phase space by a hard wall potential in the action. A classical hard

wall in position space simply reverses the conjugate momentum, so a hard wall in the action should reverse the associated angle variable. Figure 2-1 illustrates the general idea:

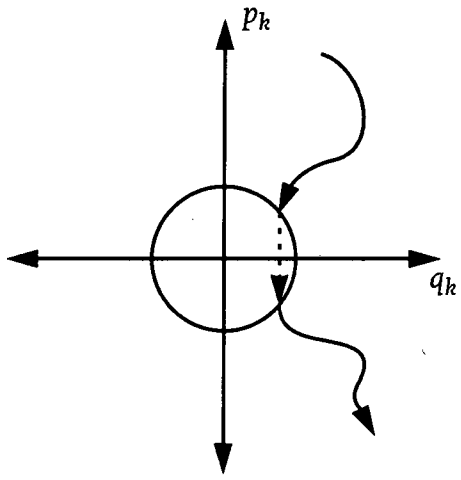

Figure 2-1. Schematic illustrating the BMH method

When a trajectory attempts to cross the $n_k < 1/2$ region, it is prevented from doing so by a reflection across the q_k axis. The simple version of this method splits the potential into harmonic and anharmonic parts:

$$V(\underset{\sim}{x}) = V_0(\underset{\sim}{x}) + V_1(\underset{\sim}{x}) , \tag{2-8}$$

where

$$V_0(\underset{\sim}{x}) = \sum_k \frac{1}{2}\omega_k^2 x_k^2 . \tag{2-9}$$

The positions and momenta for the harmonic Hamiltonian are given in terms of action $\{n_k\}$ and angle $\{\theta_k\}$ variables:

$$x_k = \sqrt{2\frac{(n_k + 1)\hbar}{\omega_k}} \cos\theta_k \tag{2-10}$$

$$p_k = \sqrt{(2n_k + 1)\hbar\omega_k}\sin\theta_k, \tag{2-11}$$

so the full Hamiltonian can be written as:

$$H(\underset{\sim}{n}, \underset{\sim}{\theta}) = H_0(\underset{\sim}{n}) + V_1(\underset{\sim}{x}(\underset{\sim}{n}, \underset{\sim}{\theta})), \tag{2-12}$$

with

$$H_0(\underset{\sim}{n}) = \sum_k \hbar\omega_k\left(n_k + \frac{1}{2}\right). \tag{2-13}$$

The trajectory is prevented from crossing into the forbidden region with a hard wall in the action which corresponds to an instantaneous reflection of the angle:

$$\begin{matrix} n_k(t) & & n_k(t) \\ & \rightarrow & \\ \theta_k(t) & & -\theta_k(t) \end{matrix} \tag{2-14}$$

Using equations 2-10 and 2-11, it is easy to see that this corresponds to:

$$\begin{matrix} x_k(t) & & x_k(t) \\ & \rightarrow & \\ p_k(t) & & -p_k(t) \end{matrix} \tag{2-15}$$

in cartesian coordinates.

Since many chemically interesting problems are highly anharmonic, however, the above treatment's use of a privileged set of harmonic modes can be made more general using instantaneous or "local" normal modes. At an arbitrary time t, the potential is expanded about a particular point $\underset{\sim}{x}(t) = \underset{\sim}{x}_t$ as follows:

$$V(\underset{\sim}{x}) = V(\underset{\sim}{x}_t) + \underset{\sim}{f}(\underset{\sim}{x}_t)^T \cdot (\underset{\sim}{x} - \underset{\sim}{x}_t) + \frac{1}{2}(\underset{\sim}{x} - \underset{\sim}{x}_t)^T \cdot \underset{\sim}{\mathsf{K}}(\underset{\sim}{x}_t) \cdot (\underset{\sim}{x} - \underset{\sim}{x}_t) , \tag{2-16}$$

where

$$\underset{\sim}{f}(\underset{\sim}{x}) = \frac{\partial}{\partial \underset{\sim}{x}} V(\underset{\sim}{x}) \text{ , and} \tag{2-17}$$

$$\underset{\sim}{\mathsf{K}}(\underset{\sim}{x}) = \frac{\partial^2}{\partial \underset{\sim}{x} \partial \underset{\sim}{x}} V(\underset{\sim}{x}) \tag{2-18}$$

If $\{\underset{\sim}{L}_k\}$ are the eigenvectors of the projected force constant matrix [67], $\underset{\sim}{\mathsf{K}}(\underset{\sim}{x}_t)$, and $\{\Omega_k^2\}$ the eigenvalues, then the "local" normal coordinates $\underset{\sim}{Q}$ and momenta $\underset{\sim}{P}$ are related to the original Cartesian variables $(\underset{\sim}{x}, \underset{\sim}{p})$ by

$$\underset{\sim}{x} - \underset{\sim}{x}_t = \sum_k \underset{\sim}{L}_k \cdot \underset{\sim}{Q} = \mathsf{L} \cdot \underset{\sim}{Q} \tag{2-19}$$

$$\underset{\sim}{p} = \mathsf{L} \cdot \underset{\sim}{P} . \tag{2-20}$$

This is a quadratic approximation to the Hamiltonian in the vicinity of $\underset{\sim}{x}_t$ which can be written in the local normal mode coordinate system as

$$H(\underset{\sim}{P}, \underset{\sim}{Q}) \cong V(\underset{\sim}{x}_t) + \sum_k \left(\frac{1}{2} P_k^2 + D_k Q_k + \frac{1}{2} \Omega_k^2 Q_k^2 \right), \tag{2-21}$$

where $\{D_k\} \equiv \underset{\sim}{D}$ is given by

$$\underset{\sim}{D} = \mathsf{L}^T \cdot \underset{\sim}{f}(\underset{\sim}{x}_t) . \tag{2-22}$$

We can complete the square for each of the shifted harmonic oscillators in Eq. 2-21,

$$\frac{1}{2}P_k^2 + D_k Q_k + \frac{1}{2}\Omega_k^2 Q_k^2 = \frac{1}{2}P_k^2 + \frac{1}{2}\Omega_k^2\left[Q_k + \left(\frac{D_k}{\Omega_k^2}\right)\right]^2 - \left(\frac{D_k^2}{2\Omega_k^2}\right), \tag{2-23}$$

but since we are computing the local normal modes at each point along the trajectory, $Q_k = 0$, so the zero-point constraint in each mode is

$$\frac{1}{2}P_k^2 + \left(\frac{D_k^2}{2\Omega_k^2}\right) \geq \frac{1}{2}\hbar\Omega_k \tag{2-24}$$

for all k. In terms of the original Cartesian coordinates and momenta, the condition for assuring that zero-point energy is preserved in mode k is

$$\frac{1}{2}\left(\underset{\sim}{L}_k^T \cdot \underset{\sim}{p}\right) + \frac{1}{2\Omega_k^2}\left(\underset{\sim}{L}_k^T \cdot \frac{\partial V}{\partial \underset{\sim}{x}}\right)^2 \geq \frac{1}{2}\hbar\Omega_k . \tag{2-25}$$

This more general version of the BMH model is implemented by adding the following steps at each point along the trajectory:

- Diagonalize the projected force constant matrix at the current position $\underset{\sim}{x}(t)$, yielding the eigenvalues $\{\Omega_k^2\}$ and eigenvectors $\{\underset{\sim}{L}_k\}$.
- For all modes k for which $\Omega_k^2 > 0$, check the zero point condition in Eq. 2-25. If it has been violated in this time step, make the replacement

$$\underset{\sim}{p} \rightarrow \underset{\sim}{p} - 2\underset{\sim}{L}_k\left(\underset{\sim}{L}_k^T \cdot \underset{\sim}{p}\right). \tag{2-26}$$

This extends the simple picture in Fig. 2-1 to allow for potential energy surfaces which are highly anharmonic. The local harmonic approximation about each point along the trajectory is expected to be excellent near the bottom of local minima on the surface, yet still allows this method to be extended to reactive systems. As presented above it prevents the trajectory from entering those regions of phase space which have less than the zero-point energy in any of the local normal modes. The questions which remain to be answered center around how strongly this method affects dynamical properties of the system. Of particular interest is the question of what the BMH method does to chemi-

cally relevant observables such as state-to-state reaction probabilities for simple reactions. Sections 2.5 and 2.6 attempt to answer these questions. Section 2.8 concludes the work on the zero-point energy problem.

2.5. Undesirable dynamical effects - the Hénon-Heiles potential

2.5.1. Model and Methods

The first model system which we used to investigate the dynamical effects of the BMH trajectory method was the Hénon-Heiles [46] Hamiltonian for two identical oscillators in mass-scaled units ($m_x = m_y = \omega_x = \omega_y = 1$):

$$H(x,y) = \frac{1}{2}\left(p_x^2 + p_y^2 + x^2 + y^2\right) + x^2 y + \frac{1}{3}y^3 . \tag{2-27}$$

Initial conditions for the classical and zpe-corrected trajectories were sampled from a quasi-classical (constant action) distribution [68] corresponding to the ground state of a zeroth order harmonic potential:

$$V_0(x,y) = \frac{1}{2}(x^2 + y^2) \tag{2-28}$$

i.e.

$$x_0 = \sqrt{(2n_x + 1)\hbar}\cos\theta_x , \tag{2-29}$$

$$p_{x0} = -\sqrt{(2n_x + 1)\hbar}\sin\theta_x . \tag{2-30}$$

with similar equations for y_0 and p_{y0}.

The quasi-classical distribution for the ground state is obtained by setting $n_x = n_y = 0$, and by sampling θ_x and θ_y randomly over the interval $(0,2\pi)$. In equations 2-29 and 2-30, $\hbar$ is a dimensionless Planck's constant which determines how quantum mechanical

the system is. For the results below, $\hbar$ was arbitrarily chosen to be $1/(7\pi)$, though other values have also been investigated.

The more general BMH method which applies the zpe-constraint instantaneously (in a local harmonic approximation at each point along the trajectory) was used for the zpe-corrected dynamics simulations, and uncorrected classical trajectories were also computed to provide a comparison.

We monitored the time dependence of a number of quantities of dynamical interest. The harmonic mode energies,

$$E_i(t) = \frac{1}{2}(p_i^2 + q_i^2) , \tag{2-31}$$

for $i = x$ and y, are of particular interest because they show the frequency with which the regular trajectories violate the zero-point energy restrictions. Additionally, the autocorrelation functions of the coordinates,

$$C_i(t) = \lim_{T \to \infty} \frac{1}{T}\int_0^T dt' q_i(t')\, q_i(t' + t) , \tag{2-32}$$

(also for $i = x$ and y) were computed, and these were Fourier transformed to obtain the power spectra, $I_i(\omega)$. Both quantities in equations 2-31 and 2-32 were averaged over the initial phases of the two modes (cf. eqs. 2-29 and 2-30) using ensembles of 100 trajectories.

For comparison with the classical and zpe-constrained trajectories, quantum mechanical values of the above quantities were also computed. The energy in mode i (cf. eq. 2-31) is given quantum mechanically by

$$E_i(t) = \langle \phi_0 | e^{(iHt)/\hbar} h_i e^{(-iHt)/\hbar} | \phi_0 \rangle , \tag{2-33}$$

where $\phi_0(x, y)$ is the initial zeroth-order (ground state) harmonic oscillator wave function, and h_i is harmonic oscillator Hamiltonian for mode i,

$$h_i = \frac{1}{2}(p_i^2 + q_i^2) . \tag{2-34}$$

If $\{\Psi_k\}$ and $\{E_k\}$ are the eigenfunctions and eigenvalues of the total Hamiltonian H - obtained by diagonalizing the matrix of H in a sufficiently large harmonic oscillator basis - then the time evolution operator in eq. 2-33 can be expressed as

$$e^{(-iHt)/\hbar} = \sum |\Psi_k\rangle e^{(-iE_k t)/\hbar} \langle\Psi_k| , \tag{2-35}$$

so that eq. 2-33 becomes

$$E_i(t) = \sum_{k,k'} \langle\phi_0|\Psi_k\rangle e^{i(E_k - E_{k'})t/\hbar} \langle\Psi_k|h_i|\Psi_{k'}\rangle\langle\Psi_{k'}|\phi_0\rangle . \tag{2-36}$$

Similarly, the time correlation function is given quantum mechanically by

$$C_i(t) = \lim_{T\to\infty} \frac{1}{T}\int_0^T dt \langle\phi_0|e^{(iHt')/\hbar} h_i e^{(-iHt')/\hbar} e^{(iH(t+t'))/\hbar} h_i e^{(-iH(t+t'))/\hbar}|\phi_0\rangle , \tag{2-37}$$

and again using eq. 2-35 for the time evolution operators, this becomes

$$C_i(t) = \sum_{k,k'} |\langle\phi_0|\Psi_k\rangle|^2 |\langle\Psi_k|h_i|\Psi_{k'}\rangle|^2 e^{(i(E_k - E_{k'})t)/\hbar} . \tag{2-38}$$

The time dependence of the zeroth-order mode energies, eqns. 2-31 and 2-36, exhibit time dependence only because the initial state is not the true ground state. This is most obvious in the quantum case which would be time independent if $|\phi_0\rangle = |\Psi_0\rangle$. (Expectation values of all operators are constant in an eigenstate.) The time correlation functions, eqns. 2-32 and 2-37, however, exhibit time dependence even if the initial state is the true ground state.

2.5.2. Results and discussion

Figure 2-2 shows the harmonic mode energies for the unconstrained (panel a) and constrained (panel b) classical calculations and for the quantum calculations (panel c). The results of the constrained classical mechanics are perhaps in somewhat better agreement with the quantum results, but the unconstrained classical trajectories are not in serious error. This may be explainable in terms of the initial conditions for the trajectories, which were chosen from the $n_x = n_y = 0$ rings in phase space, i.e. very close to the minimum on the potential energy surface. Although there is anharmonicity in the system that would tend to mix the two vibrations, near the bottom of the well the coupling is quite small and the unconstrained motion may be nearly harmonic. This would tend to preserve much of the energy of a given mode within that mode.

Figure 2-3 shows the results for the power spectra, the Fourier transforms of the time correlation functions. Here, matters are quite different. The normal, i.e. unconstrained classical mechanics gives a single peak at $\omega \approx 1$, signifying quasi-periodic motion. Figure 2-4 shows the coordinate space projection of this trajectory, confirming this.) The constrained classical mechanics, however, shows a broad, essentially continuous distribution of frequencies, characteristic of chaotic dynamics. (Fig. 2-4b shows the configuration space projection of a constrained trajectory, confirming the chaotic behavior of the motion.) The quantum result in Fig. 2-3c is clearly much closer to that of the *un*constrained classical dynamics. The BMH zero-point energy constraints thus severely modify the classical dynamics in what appears to be a physically incorrect fashion.

A variety of other initial conditions and potential parameters have been considered, but the qualitative results were all similar to those presented above. The BMH constraint method does indeed prevent the energy in each degree of freedom from falling below its local zero-point value, but the constraint appears to introduce non-physical behavior into the trajectory simulations - a side effect that may be worse than the problem that the method was intended to fix.

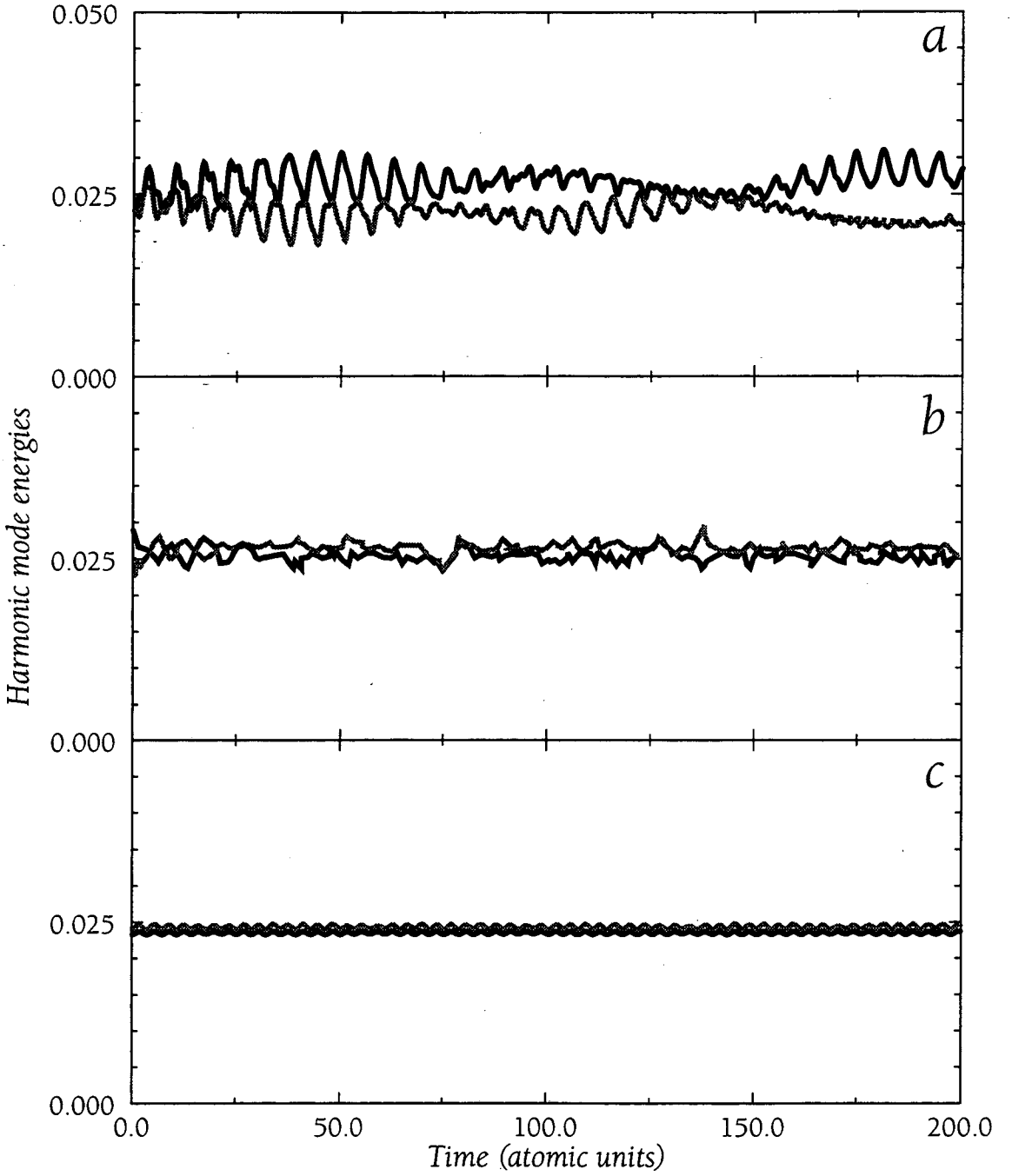

Figure 2-2. The BMH method's effects on harmonic mode energies

Time-dependent harmonic mode energies for the unconstrained and constrained classical mechanics (panels a and b, respectively), and for the quantum mechanical calculation (panel c). The results are for the "ground state" of the Hamiltonian with $\hbar = 1/7\pi$. The classical results are averages of 100 trajectories. The harmonic mode energies in the x direction are shown as solid lines, and in the y direction are shown as shaded lines.

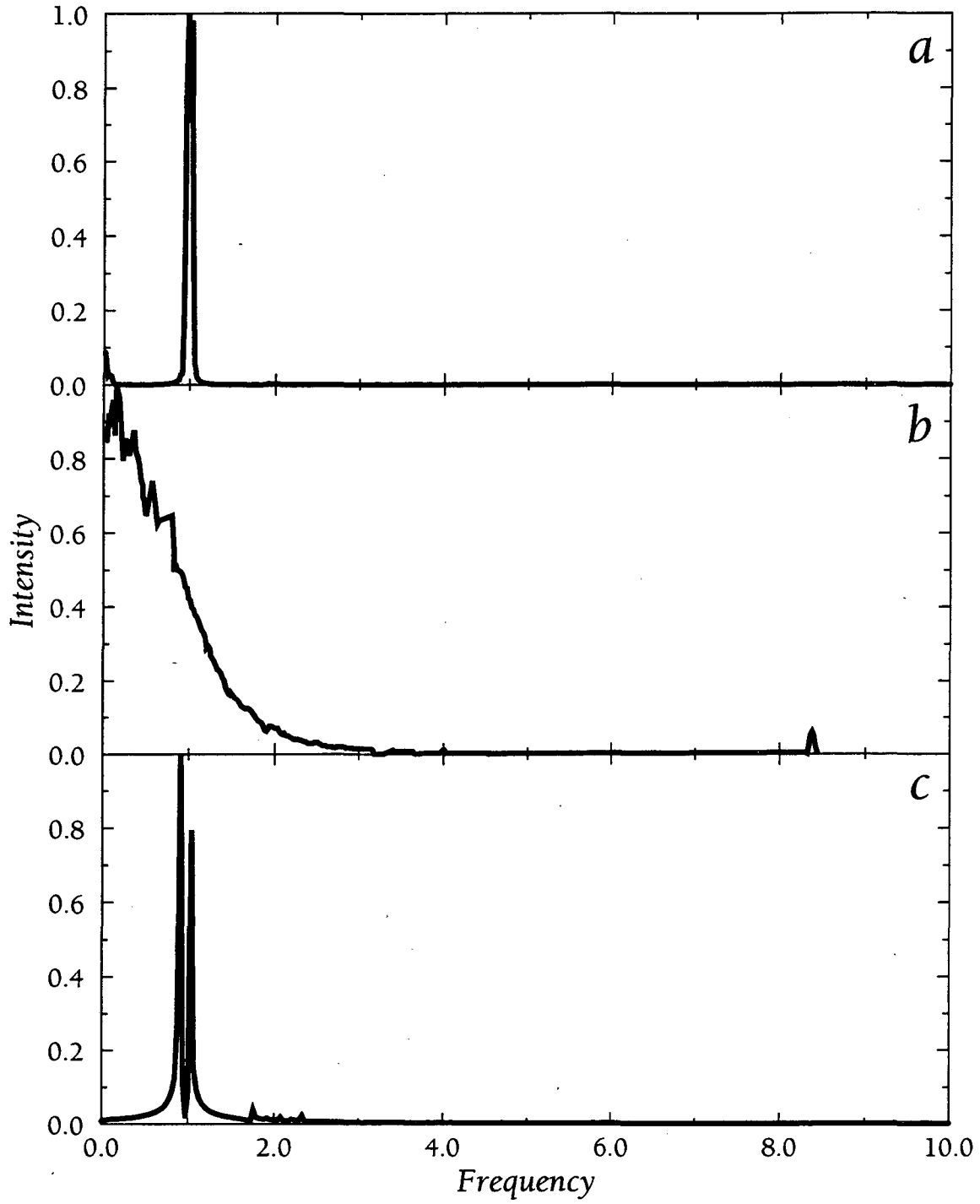

Figure 2-3. The BMH method's effects on the power spectrum.

Power spectrum of the "ground state" dynamics. Panels a and b are for the unconstrained and constrained trajectories, respectively. The quantum results are shown in panel c. The power spectra above are generated by fourier transforming the autocorrelation function of the x coordinate. The spectra for the y coordinate are nearly identical to the ones shown above.

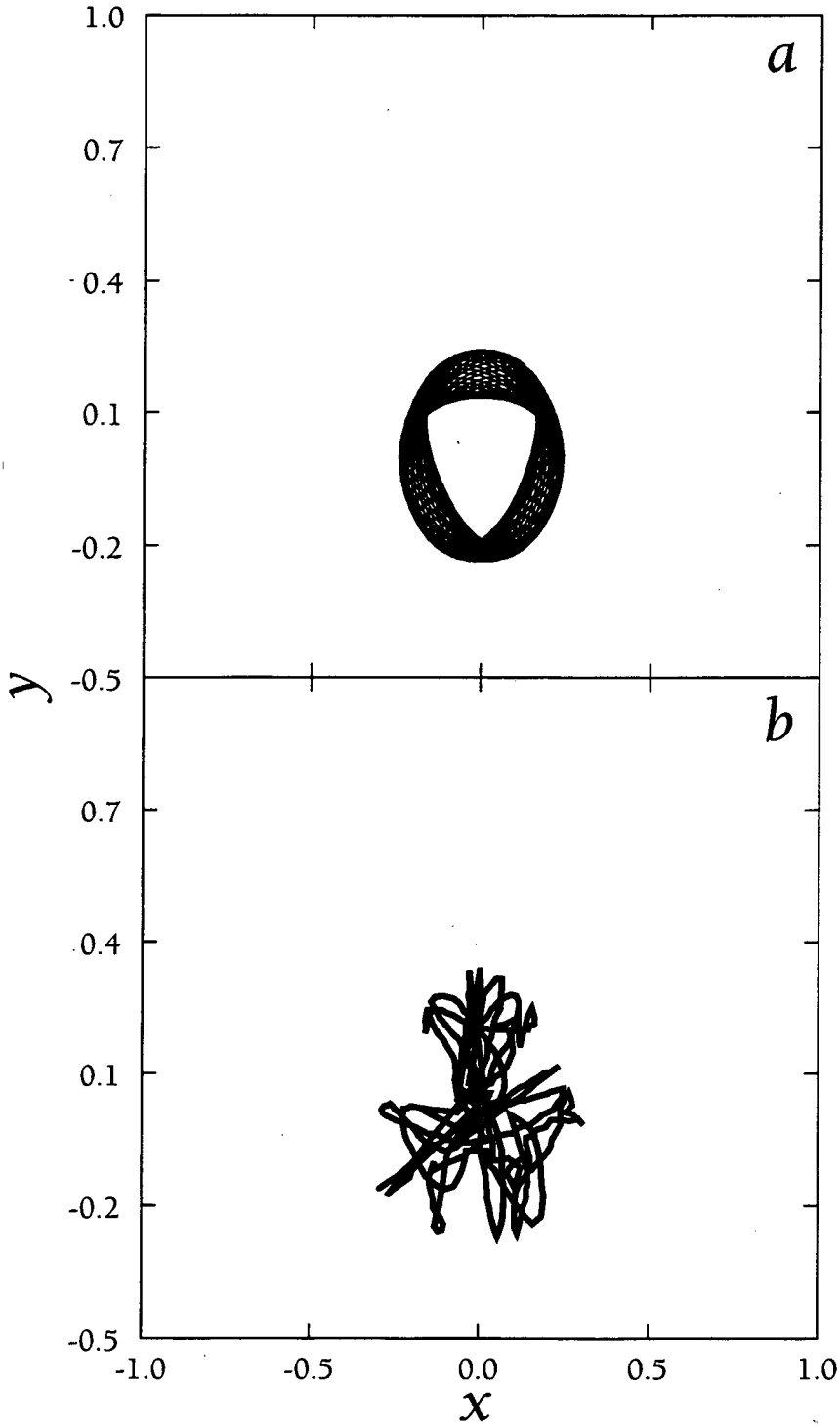

Figure 2-4. How BMH effects trajectories

Configuration-space projections of representative unconstrained (a) and constrained (b) classical trajectories.

2.6. Undesirable effects on observables: H + HF(v=2,3) -> F + H_2(v=0)

The previous work on the Hénon-Heiles potential centered around undesirable side effects in the dynamics that are introduced by application of the BMH zero-point energy constraint method. However, if a method for correcting classical trajectories for zero-point energy can obtain more "quantum-like" chemically relevant *observables* from a classical calculation, then the method may still have utility in the simulation of large chemical systems. A second model system was therefore investigated in order to answer to what degree the BMH method corrects the classical energy-dependent state-to-state or half-state-selected reaction probability in a real world reaction. The system under consideration is the H + HF $\rightarrow$ F + H_2 reaction, which has been studied extensively in numerous experiments. [69, 70] This reaction also has a large library of high-quality potential energy surfaces associated with it, [71, 72, 73] and quantum and quasi-classical state-to-state reaction rate calculations have been performed on some of these surfaces. [47] These factors made this reaction an ideal choice for an investigation of how the BMH method effects observable quantities in a real chemical reaction.

2.6.1. Model and Methods

The potential energy surface used to explore the dynamics of the H + HF $\rightarrow$ F + H_2 reaction was Muckerman's M5 potential. [71] The M5 potential is a London-Eyring-Polanyi-Sato (LEPS) [74, 75, 76, 77] surface which has the functional form

$$V(r_{AB}, r_{BC}, r_{AC}) = \frac{Q_{AB}}{1+S_{AB}} + \frac{Q_{BC}}{1+S_{BC}} + \frac{Q_{AC}}{1+S_{AC}} - \left\{\frac{1}{2}\left[\left(\frac{J_{AB}}{1+S_{AB}} - \frac{J_{BC}}{1+S_{BC}}\right)^2 + \left(\frac{J_{BC}}{1+S_{BC}} - \frac{J_{AC}}{1+S_{BC}}\right)^2 + \left(\frac{J_{AC}}{1+S_{AC}} - \frac{J_{AB}}{1+S_{AB}}\right)^2\right]\right\}^{1/2} \tag{2-39}$$

where Q and J are the Coulomb and exchange integrals from the Heitler-London valence bond theory. Q and J are determined from the Morse functions for a given two-atom pair as follows:

$$Q_{AB} + J_{AB} = D_{AB}\{e^{-2\beta_{AB}\left(r_{AB} - r^0_{AB}\right)} - 2e^{-\beta_{AB}\left(r_{AB} - r^0_{AB}\right)}\} \tag{2-40}$$

$$Q_{AB} - J_{AB} = \frac{1}{2}D_{AB}\{e^{-2\beta_{AB}\left(r_{AB} - r^0_{AB}\right)} + 2e^{-\beta_{AB}\left(r_{AB} - r^0_{AB}\right)}\}\ . \tag{2-41}$$

The S (or Satô) parameters in equation 2-39 are chosen to fit the location and height of the barrier with respect to the BC and AB distances. The parameters used for constructing the M5 surface are given in Table 2-1. The M5 surface is known to have some prob-

	$ij=H_aH_b$	$ij=FH_a$	$ij=FH_b$
β_{ij}(Å^{-1})	1.9420	2.2187	2.2187
D_{ij}(eV)	4.7462	6.1229	6.1229
r^0_{ij}(Å)	0.7419	0.9170	0.9170
S_{ij}	0.106	0.167	0.167

Table 2-1. LEPS parameters for the M5 surface

lems when used as a model for the H + HF → F + H_2 reaction, and has been recently been replaced in most calculations by the T5A [72] and 5SEC [73] surfaces which reproduce the *ab initio* energies [78] over much more of the configuration space than M5 does. There are, however, good quantum [47] and quasi-classical calculations that have been performed on M5 that we can compare our results to, and the newer surfaces do not have this background.

In a collinear system, it is possible to reduce the system to two degrees-of-freedom using mass-weighted Jacobi coordinates. Using this coordinate system, we calculated state-to-state and half-state-selected reaction probabilities ($P_{3,0}$, $P_{2,0}$, *and* $P_{n,0}$) with both classical and zpe-constrained trajectories. In the notation above, the reaction is $HF\,(v=i) + H \rightarrow H_2\,(v=j) + F$ where the state-to-state probabilities are denoted $P_{i,j}$ and the half-state-selected probabilities are denoted $P_{n,j}$. The microcanonical reaction probabilities were calculated at a number of energies ranging from 0.3 to 0.7 eV.

The trajectories were started in a particular vibrational "state" of the HF diatom by first finding the energy levels of the appropriate Morse oscillator, [79, 80]

$$E_n = -D + \hbar\omega\{\left(n+\frac{1}{2}\right) - \frac{1}{\zeta}\left(n+\frac{1}{2}\right)^2\}\text{, where} \tag{2-42}$$

$$\zeta = \frac{2r_o^2\sqrt{2\mu D}}{\beta\hbar^2} \text{ and } \omega = \beta\sqrt{\frac{2D}{\mu}} \tag{2-43}$$

and by setting the internuclear distance for HF to the maximum separation allowed at this energy. The momentum of the vibrational coordinate was set to 0, and the remaining energy was put into the initial momentum of the scattering coordinate, P_0. To sample the phase of the vibration, the period (τ) of the HF vibration was calculated as follows:

$$\tau = \frac{2\pi}{\omega_{vib}}\text{, where } \omega_{vib} = \frac{\omega}{2\pi c} - 2\frac{\omega}{2\pi c\zeta}\left(n+\frac{1}{2}\right). \tag{2-44}$$

This period was then used to set an initial distance for the scattering coordinate:

$$R_0(t=0) = R_{ref} + \phi\tau\frac{P_0}{\mu} \tag{2-45}$$

where R_{ref} was taken to be a large distance (15 Bohr), μ was the reduced mass of the scattering coordinate, and ϕ was sampled uniformly over the interval $(0,2\pi)$. At each energy and in each of the initial vibrational states of the HF molecule, 100 unconstrained and 100 zpe-constrained trajectories were run until either the HF or HH distances reached a value of 15 Bohr. The final states of the trajectories were placed into quasi-classical "bins" depending on the energy in the vibrational coordinate for the correct arrangement of the Jacobi coordinates.

2.6.2. Results and Discussion

The results of the state-to-state calculations are compared to the quantum calculations of Bowman *et al.* [47] and are presented in Figs. 2-5 and 2-6, and the half-state selected

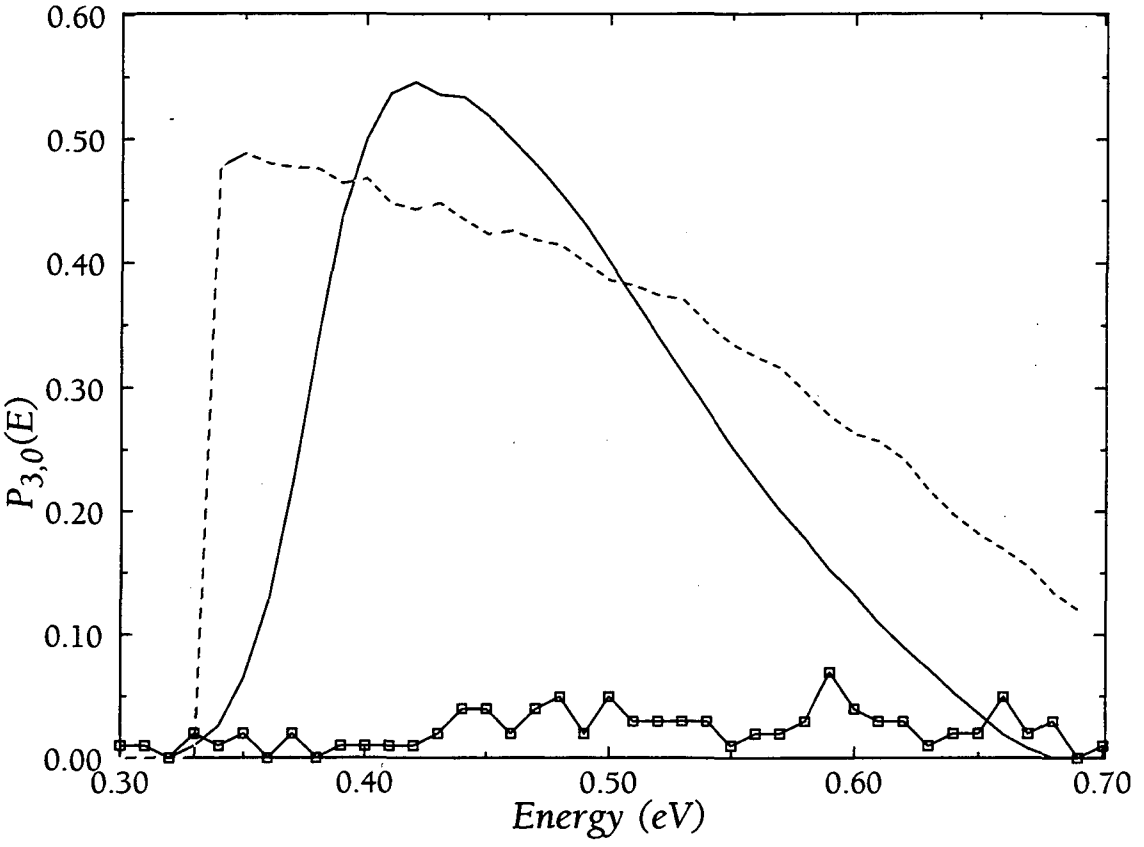

Figure 2-5. The BMH results for the $P_{3,0}$

The unconstrained classical (dotted line) and zpe-constrained reaction probabilities (squares) compared to the quantum results (solid line) of Bowman et al. [47] for HF in the v=3 state reacting to form H_2 in the v=0 vibrational state.

results are presented in Fig. 2-7. The results indicate that the zpe-constraints have introduced very serious errors into the reaction probabilities for a simple barrier crossing reaction, making it essentially unusable for calculating chemically relevant quantities in its current form.

The choice of this particular reaction was fortuitous in some ways because it illustrates very clearly exactly where the BMH method introduces the greatest errors. Immediately

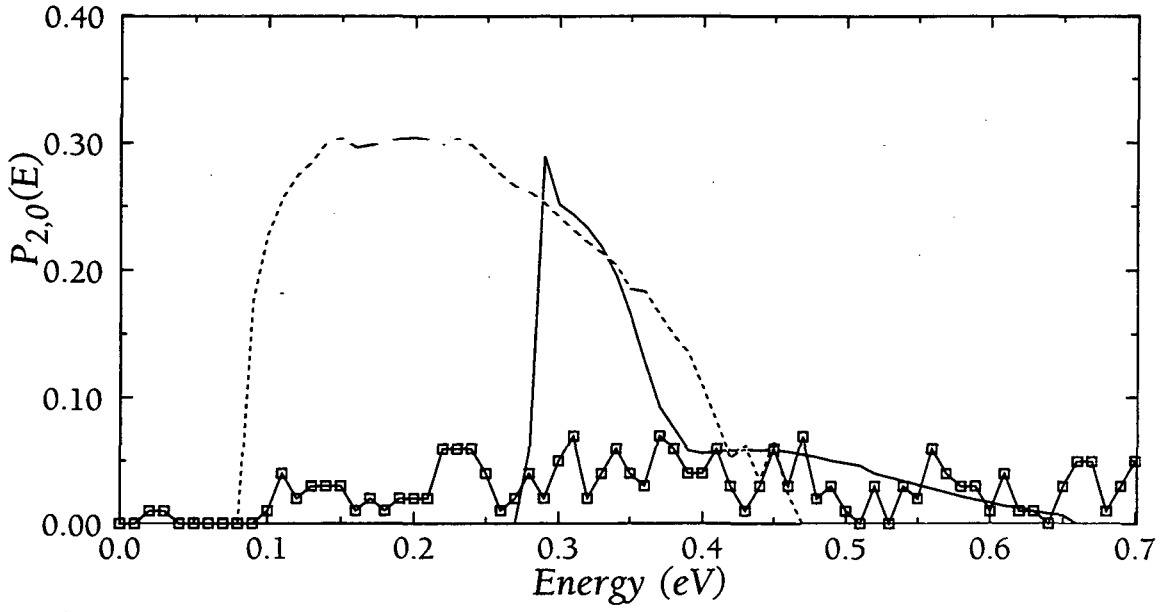

Figure 2-6. The BMH results for $P_{2,0}$

The unconstrained classical (dotted line) and zpe-constrained reaction probabilities (squares) compared to the quantum results (solid line) of Bowman et al. [47] for HF in the v=2 state reacting to form H_2 in the v=0 vibrational state.

after trajectories cross the top of the barrier, the downhill (H_2 + F) side of the barrier looks (locally) like the entrance to a region in the surface that contains a minimum along the reaction coordinate. The local normal mode expansion about that point in the trajectory sees a harmonic well that may have appreciable zero-point energy in the reaction coordinate even though the local calculation of the zero-point energy would drop to zero as the reaction coordinate is followed out into the asymptotic region. Figure 2-8 illustrates this effect in detail.

In order to illustrate to what degree this problem will manifest itself in calculations of reaction probabilities and to illustrate one possible solution to the problem, we have plotted the zero-point "condition" for the BMH method for a simple one-dimensional Eckart barrier

$$V = V_0 \left(sech\,(x/a) \right)^2 . \tag{2-46}$$

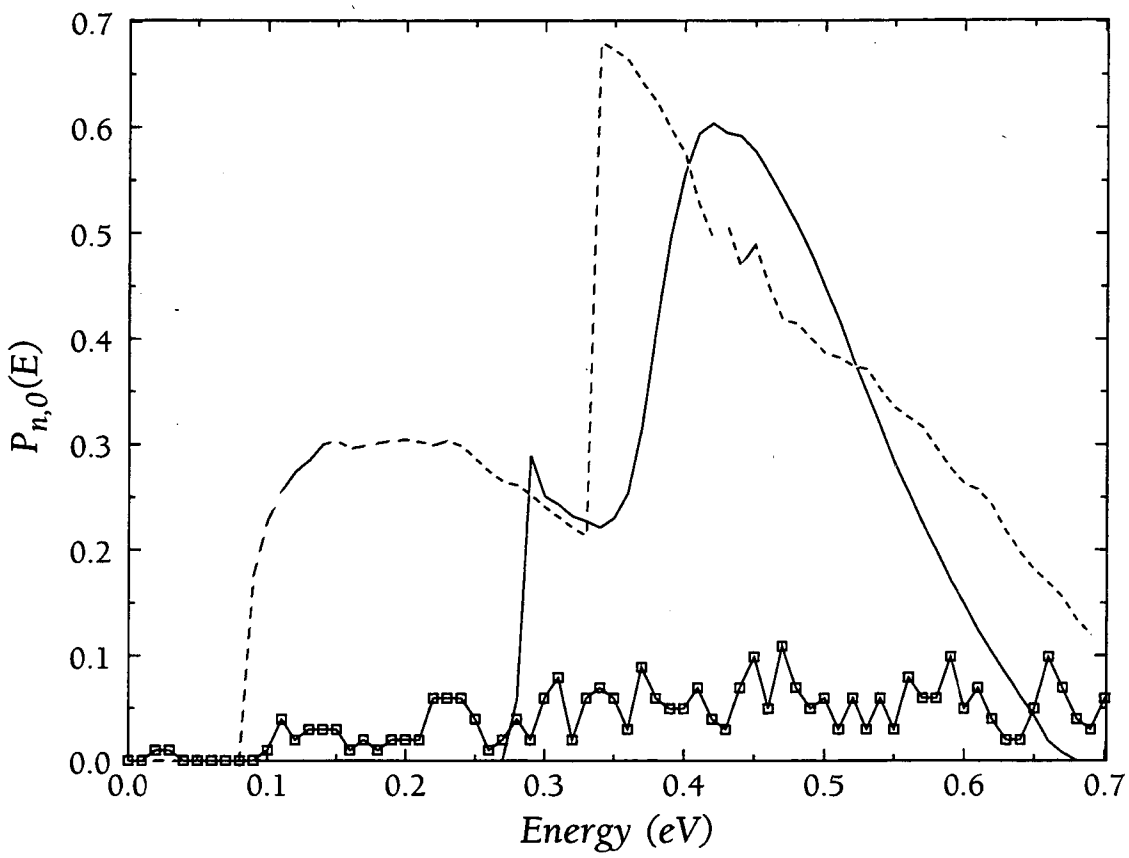

Figure 2-7. The BMH results for $P_{n,0}$

The unconstrained classical (dotted line) and zpe-constrained reaction probabilities (squares) compared to the quantum results (solid line) of Bowman et al. [47] for HF in all energetically accessible vibrational states to react to form H_2 in the v=0 vibrational state.

It is obvious that a one-dimensional model has no zero-point energy problem because there are no perpendicular vibrations, but the BMH method is unable to make distinctions between the reaction coordinate and non-reactive degrees of freedom, so this model illustrates the problem very clearly.

The "zero-point condition" for the one-dimensional model, or the condition which will result in a momentum-reversing kick for a trajectory that just barely crosses the barrier is given by

$$Z = \frac{\hbar}{2}\omega - \frac{1}{2\omega^2}\left(\frac{\partial V}{\partial x}\right)^2 \tag{2-47}$$

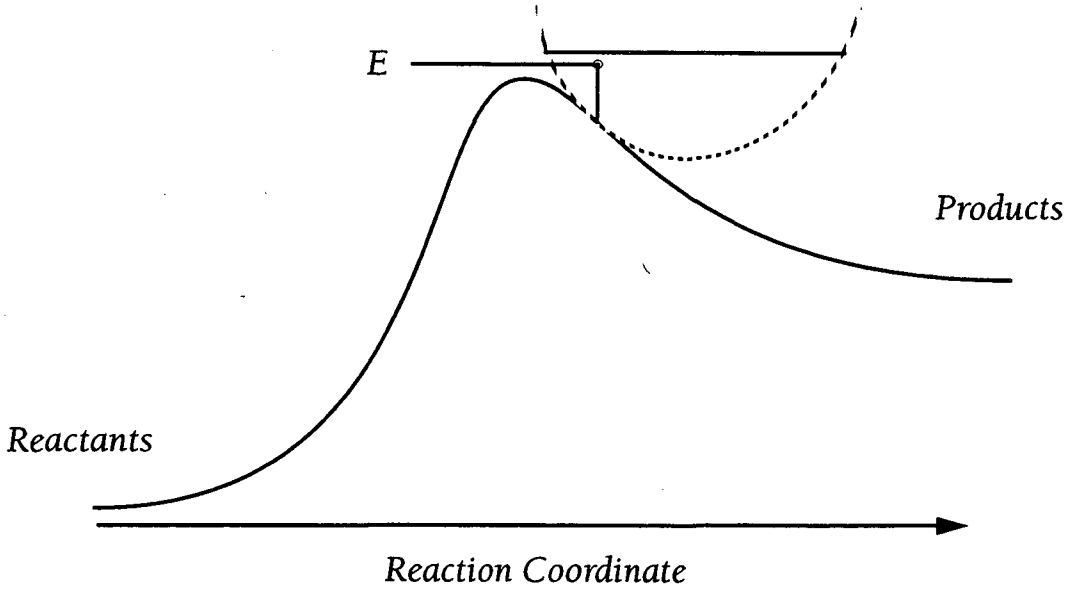

Figure 2-8. Sketch of the BMH barrier crossing problem

This illustrates how the reaction coordinate can be mistaken by the local normal mode approximation as a harmonic well with a zero-point energy above the barrier energy. At energies just above threshold, trajectories that should be reactive are knocked back over the barrier by the BMH method.

where ω is obtained from the second derivative of the potential at x. Fig. 2-9 illustrates how the zero-point condition can kick a trajectory that has already crossed the barrier back into the reactant region. The curves in Fig. 2-9 are calculated assuming a mass of 1 atomic unit. The zero-point condition for a more realistic mass and surface (an Eckart barrier which approximates the collinear $H + H_2$ barrier) is shown in Fig. 2-10. Although the hard zero-point constraints do not cause problems on the more realistic surface, it is possible that a chemically relevant potential energy surface which has a small first derivative after the inflection point following the barrier could exhibit the same behavior shown in Fig 2-9.

2.6.3. Future directions for the BMH model

One possible solution to this problem is to introduce a soft-wall potential in the action instead of the hard wall that gives the momentum-reversing dynamics of the BMH method. A soft wall in the action would allow trajectories to cross into the forbidden

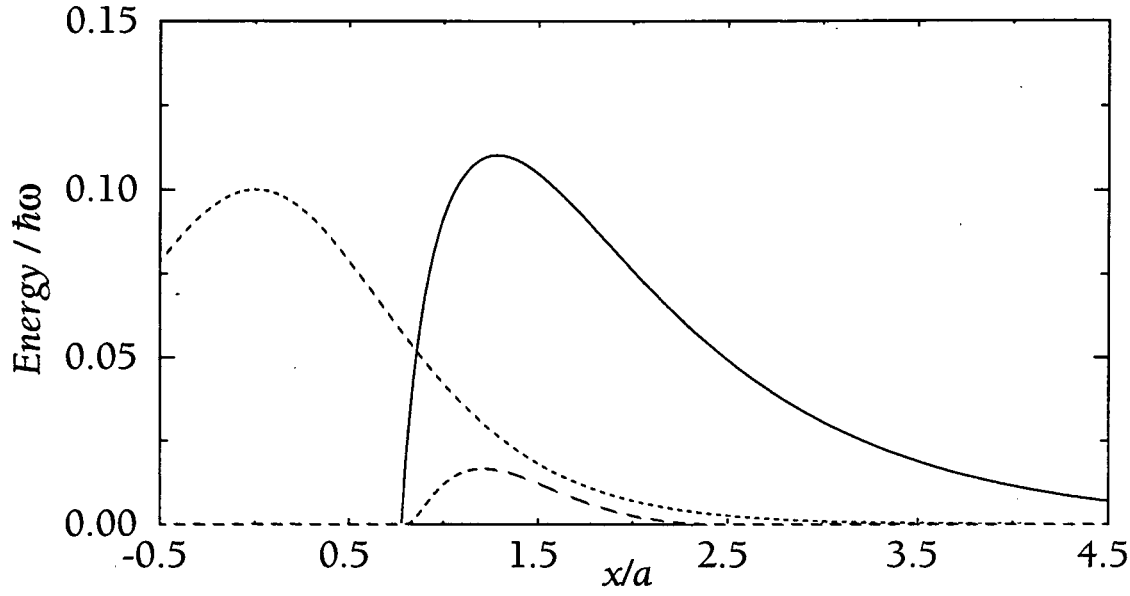

Figure 2-9. Zero Point Corrections for the Eckart Barrier

The Eckart barrier (dotted line) with $V_0 = 0.1$, $m = 1$, and $a = 1.0$ is plotted along with the "hard" zero point condition (solid line) from eqn. 2-47 and the "soft" constraint (dashed line) from eqn. 2-56. A value of 3 was used for λ in the soft constraint plotted above. Trajectories that cross the barrier with energies below 0.11 on the scale above will be reflected back across the barrier by the BMH method. All valid trajectories at the top of the barrier are allowed into the product region by the soft constraints.

region in phase space temporarily, but would discourage them from staying there indefinitely. The Hamiltonian including the soft constraints can be written as follows:

$$H = \frac{\underset{\sim}{p}^2}{2m} + V(\underset{\sim}{q}) + \sum_j f(n_j) \ , \tag{2-48}$$

where soft harmonic potentials,

$$f(n_j) = a n_j^2 h(-n_j) \ , \tag{2-49}$$

are placed in the action to repel trajectories from the regions in phase space that have less than zero-point energy in all modes.

With these potentials, Hamilton's equations of motion become

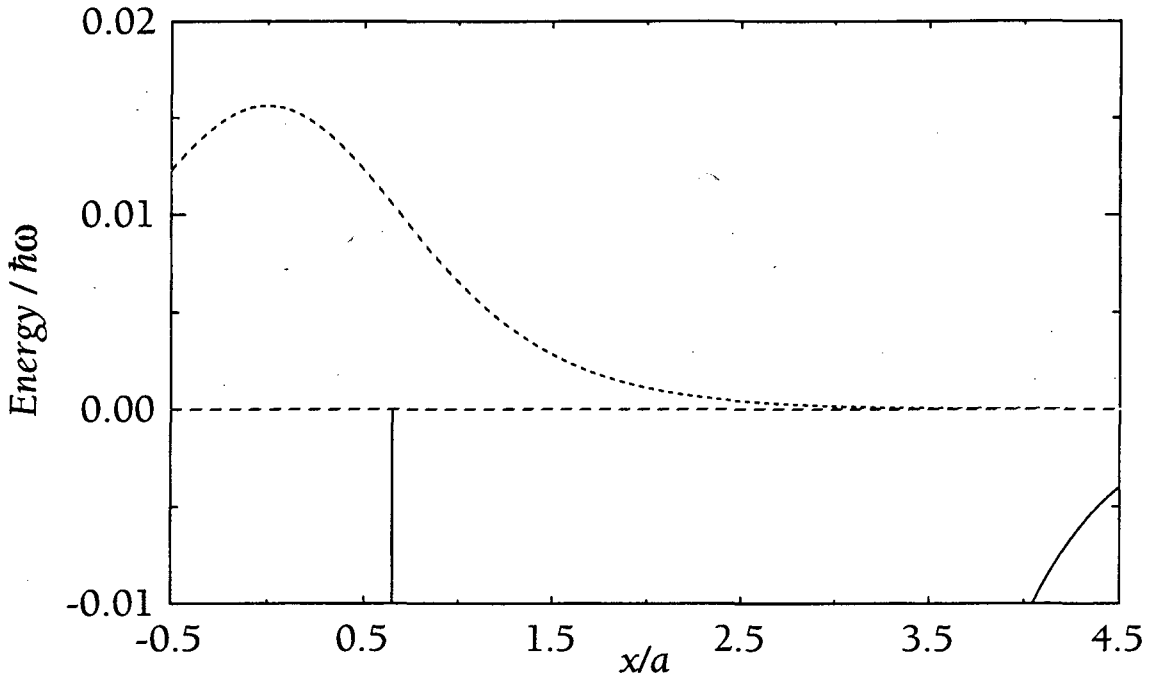

Figure 2-10. Zero Point corrections for a Realistic Barrier

This figure shows the zero-point violations for a more realistic barrier with parameters approximating the barrier for the collinear H + H_2 reaction. (V_0 = *0.425 eV*, *m* = *1060*, and *a* = *1.0*). In this case the barrier does *not* exhibit the zero-point violation problem shown in Fig. 2-9. The solid line is the hard zero-point condition which will never be violated on this surface, and soft constraints (dashed line) are only slightly above 0.

$$\dot{q}_i = \frac{\partial H}{\partial p_i} = \frac{p_i}{m} + \sum_j f'(n_j)\frac{\partial n_j}{\partial p_i} \tag{2-50}$$

$$\dot{p}_i = -\frac{\partial H}{\partial q_i} = -\frac{\partial V}{\partial q_i} - \sum_j f'(n_j)\frac{\partial n_j}{\partial q_i}, \tag{2-51}$$

where n_j can be written as:

$$n_j = -\frac{1}{2} + \left(\frac{1}{2}(\underset{\sim}{p}\cdot\underset{\sim}{L}_j)^2 + \frac{1}{2\Omega_j^2}\left(\underset{\sim}{L}_j^T\cdot\frac{\partial V}{\partial \underset{\sim}{q}}\right)^2\right)^{\frac{1}{2}} \tag{2-52}$$

These "new" Hamilton's equations can be simplified to the following form:

$$\dot{\underset{\sim}{q}} = \underset{\sim}{M} \cdot \underset{\sim}{p} \tag{2-53}$$

$$\dot{\underset{\sim}{p}} = -\left(\underset{\sim}{M} \cdot \frac{\partial V}{\partial \underset{\sim}{q}} \right), \tag{2-54}$$

where

$$\underset{\sim}{M} = \underset{\sim}{1} + \sum_j \frac{2an_j}{\Omega_j} h(-n_j) \cdot \underset{\sim}{L}_j \underset{\sim}{L}_j \cdot \ . \tag{2-55}$$

This formulation conserves the energy of the original Hamiltonian, and has only one adjustable parameter.

For a one-dimensional problem like the Eckart barrier, the value of the soft potential in the action can be written

$$f(n) = \lambda \left(-\frac{1}{2} + \frac{p^2}{2} + \frac{1}{2\omega^2} \left(\frac{\partial V}{\partial x} \right)^2 \right)^2 . \tag{2-56}$$

Once again, ω is obtained from the second derivative of the potential energy at x. For a one-dimensional problem like the Eckart barrier, the momentum is easily found as a function of position and energy, so the conditions at which the soft constraint begins to affect the dynamics can be plotted along with the hard-wall constraint of the BMH method. Figs. 2-9 and 2-10 show the soft constraints for trajectories with energies just above the barrier height. The primary advantage of the soft constraint is that trajectories that have enough energy to cross the barrier are allowed to proceed into the product channel. On the realistic surface in Fig. 2-10, the soft effective potential barely rises above 0, and is not expected to effect the dynamics at all.

Simulations to elucidate the effects that the soft constraints have on chemically relevant observables would be of great use in determining whether dynamics altering methods (like the BMH method) are worth using in simulations of larger systems. However, given

our initial investigations of the effects of the BMH method on the dynamics of the Hénon-Heiles model, as well as on observable quantities (reaction probabilities, etc.), we are not particularly optimistic about such methods.

2.7. Other Dynamics-Altering Methods

Recently, Peslherbe and Hase [81] extended the BMH method for rotating systems so that linear and angular momenta are conserved when the constraints are applied. (The BMH method does not necessarily conserve these quantities). Their extensions to the original method are quite impressive, but they are still expected to suffer from the post-barrier problem discussed in Section 2.6 in situations where the original BMH method exhibits the problem.

Lim and McCormack introduced an active method that was very similar in character to the BMH method. [82, 83] The new "twist" on correcting the trajectories was that instead of reflecting the trajectories across the $q=0$ line in phase space, a semiholonomic constraint is applied, forcing the trajectory to slide around the rim of the forbidden region. Modes that are about to violate the zero-point constraint are transformed as follows

$$(q_i, p_i) \rightarrow (\alpha_i q_i, \alpha_i p_i) \ , \tag{2-57}$$

where

$$\alpha_i = \sqrt{\frac{2E_i^z}{p_i^2 + q_i^2}} , \tag{2-58}$$

and E_i^z is defined as the left-hand-side of equation 2-25. All other vibrational modes are transformed with

$$(q_j, p_j) \rightarrow (\gamma q_j, \beta p_j) \ . \tag{2-59}$$

The coefficients γ and β are chosen to conserve total energy and linear momentum. The effect of these transformations is illustrated in Fig 2-11. Any mode which is about to

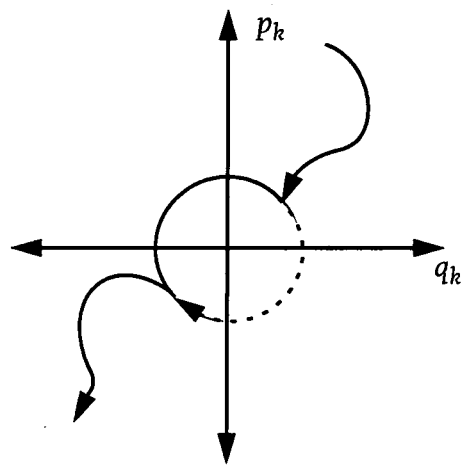

Figure 2-11. Sketch of the TRAPZ constraint method

drop below the ZPE is forced to slide around the rim of the ZPE ring in phase space. The trajectory leaves the ZPE orbit tangentially when the constraint is no longer needed.

Lim and McCormack found that their method is free of some of the dynamical pathologies that were present when the BMH method was applied to the Hénon-Heiles Hamiltonian. Their power spectra look quite similar to the quantum and classical results presented above. However, in regions where the Hénon-Heiles Hamiltonian exhibits classically chaotic motion, their method collapses all trajectories to a small set of periodic orbits. They did not carry out the corresponding quantum calculation with which to compare their results.

Lim and McCormack's method applies the zero-point constraints at the same point that the BMH method applies its constraints, and it could suffer from the same mis-identification of the post-barrier region as a vibrational mode in situations where the BMH method exhibits the same problem. The decision whether their method will be useful in trajectory simulations of chemical systems awaits the comparison of trajectories run with their method to quantum mechanical calculations of reaction probabilities on a real potential energy surface.

2.8. Conclusions

So far, none of the methods proposed for fixing the zero-point energy problem have been clearly superior to unmodified classical trajectory simulations. Indeed, some of the errors introduced in the course of fixing the ZPE problem have been worse than the original problem! The BMH method seems to introduce serious errors in trajectory calculations, and so far the only other "active" method which shows promise does not conserve angular momentum and changes the essential dynamics of chaotic systems. Whether or not the mis-identification of the post-barrier region as a harmonic well is relevant to real trajectory simulations awaits a more detailed analysis, but this problem will be most apparent on surfaces which are nearly flat (small first derivatives) following the inflection point after a barrier (where ω is increasing rapidly). The potential energy surfaces for biological molecules are usually quite corrugated with many local minima separated by barriers, and it seems possible that simulations on these surfaces could exhibit this problem.

None of the passive methods discussed at the beginning of this Chapter are able to prevent individual trajectories from falling below the zero-point energy of a vibrational mode, but they can provide ensemble averages that closely resemble the quantum mechanical observables. This seems like a more reasonable goal than trying to fix a dynamical method which (for the most part) works quite well. What is needed, it seems, is a method for sampling initial conditions and sorting final conditions that is better than the traditional quasiclassical method. There is still some debate on whether the ZPE problem is simply an artifact of how we perform these aspects of classical simulations, and until the problem is well understood, solutions to the problem will be appropriate for only a limited set of situations.

3 Resonant Features in the Energy Dependence of the Rate of Ketene Isomerization

Abstract

Calculations of the microcanonical isomerization rates for vibrationally excited ketene are presented. The calculations utilize the quantum reactive scattering methodology of absorbing boundary conditions (ABC) with a discrete variable representation (DVR) to obtain the cumulative reaction probability for one form of ketene to isomerize via the oxirene intermediate, and were carried out with model 1-, 2-, and 3-degree-of-freedom potential energy surfaces constructed using *ab initio* data. Significant differences are seen in the energy-dependent features of the microcanonical rate for the single mode and multi-mode potentials; e.g., the single mode potential exhibits tunneling resonances with widths of around 1 cm^{-1}, while the calculations involving more than one degree of freedom have additional resonant features that have widths around 10 cm^{-1} and also exhibit non-Breit-Wigner resonant lineshapes. This suggests that many of the resonance features are best described as Feshbach (energy transfer, or dynamical) resonances that result because of a strongly bent region on the multi-mode potential energy surfaces. The calculated rates show reasonable qualitative agreement with the experimental results of Lovejoy and Moore. [12]

3.1. Introduction

In recent history, theoretical models for the reactions of small molecules have shown remarkably good agreement with experiments on the same reactions. Transition state theory [86, 87] and RRKM theory [56, 57, 58, 59] have both proven to be powerful predictive and explanatory models for a wide class of reactions. Likewise, exact quantum

calculations [88] have had equal successes with reactions that involve H and D atom motion, showing experimentalists the details one could expect in an angular distribution from a system that exhibited a resonance, [30] and predicting the role of the geometric phase in reactions that involve conical intersections between two electronic surfaces. [89] However, the computational demands of exact quantum calculations have limited their applicability to at most 4 atom systems. [37]

Although there have been many of these theoretical investigations of quantum effects on chemical reactivity, there have been few experimental confirmations of these effects. Neumark *et al.* [9] observed dynamical resonances in a scattering experiment on the F + H_2 reaction, but scattering studies are carried out over a wide range of impact parameters, and the requisite averaging over total angular momentum can obscure the experimental signs of quantum effects. Unimolecular reactions, however, can be studied from well-defined initial states, which can reveal the effects of resonances on reaction rates.

Lovejoy and Moore [12] recently reported some remarkable experimental results on the photodissociation and photoisomerization of ketene. Figure 3-1 shows a (much simplified) picture describing the situation; C and C' denote the isotopes carbon-12 and carbon-13, respectively. Very cold ketene (in a supersonic beam, T_{rot} ~ 4 °K) is laser-excited to a well-defined energy E (energy resolution is ~ 1 cm^{-1}) and dissociation products (carbon monoxide and methylene) are observed. If the reactant molecule is $H_2CC'O$, then the major product is CH_2 and C'O, but 10-20% of the product has the isotopes of carbon switched, *i.e.* $C'H_2$ and CO, indicating that the isomerization,

$$H_2C{=}C'{=}O \quad \leftrightarrow \quad O{=}C{=}C'H_2\,, \tag{3-1}$$

has taken place prior to dissociation, presumably passing through the oxirene intermediate (cf. Fig. 3-1). (This isomerization or exchange process was also deduced from much earlier "hot atom" experiments by Rowland *et al.* [90]) From the branching ratio between normal and exchanged products, Lovejoy and Moore used a simple kinetic model to extract separately the unimolecular rate constants for direct dissociation (i.e.,

$H_2C{=}C'{=}O \rightarrow H_2C + C'{=}O$ without isomerization) and for isomerization, $k_d(E)$ and $k_{iso}(E)$, respectively. In a series of papers, [10, 14, 15, 11] Moore *et al.* have reported on many other interesting aspects of ketene photodissociation. The dissociation onto the triplet methylene surface is the subject of Chapter 4.

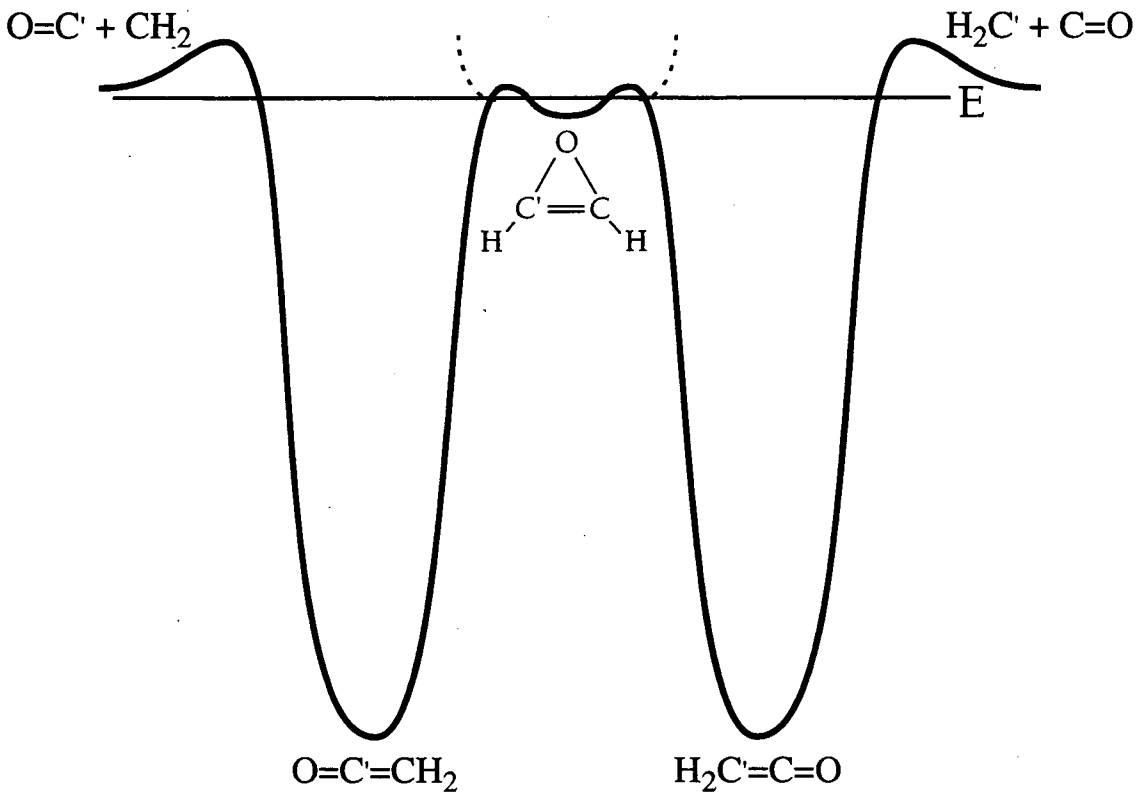

Figure 3-1. Sketch of the energetics along the reaction coordinate

A sketch of the relevant structures and energies involved in the photodissociation and photoisomerization of ketene.

The energy dependence of $k_d(E)$ shows some interesting step structure due to quantization of the transition state but is otherwise a very typical unimolecular $k(E)$ for which standard microcanonical transition state theory (*i.e.* RRKM [56, 57, 58, 59]) is an excellent description. The isomerization rate $k_{iso}(E)$, however, varies non-monotonically and exhibits regularly-spaced peaks as the energy is increased.

This appears to violate one of the fundamental tenets of transition state theory. If transition state theory were valid for this experiment, then the isomerization rate would appear to be a 'staircase' as a function of energy. As more vibrational levels at the transition state were opened with increasing reactant energy, the rate would jump up a step. Each step would indicate an additional open channel at the transition state.

Lovejoy and Moore observed a rate constant which had large features in the energy dependence of the rate, and was most certainly non-monotonic with increasing energy. Citing *ab initio* studies on the oxirene structure,[91, 92]

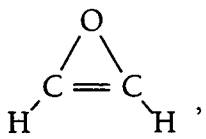

(3-2)

they tentatively concluded that the features in the energy dependence of the reaction rate were due to tunneling resonances through quasi-bound states in a small well in the potential energy surface around oxirene. Resonance tunneling through a one-dimensional double barrier is a well-known phenomenon, but it has never (to our knowledge) been observed in a molecular process. (Under less well defined experimental conditions, it would be easily averaged out.) Because of the novelty of this process, we therefore undertook a more detailed theoretical treatment, first to see if our theoretical methodology is capable of handling this complex reaction dynamics accurately for a polyatomic molecule of this size, and also to lend support (or not) to Lovejoy and Moore's interpretation of their observed structure.

Of additional interest, it has been postulated that ketene isomerization through the oxirene structure is an important step in the Wolff rearrangement, [93, 94] in which diazoketones are photolyzed to ketocarbene intermediates, which can then rearrange to form ketenes. An isomerization through the symmetric oxirene intermediate has been proposed [95, 96, 97] as an explanation for the observation that diazoketones that have been ^{13}C-labeled at the carbonyl carbon often have mixed labeling of the two carbons after the Wolff rearrangement is complete. A more complete understanding of the

dynamics involved in ketene isomerization observed by Lovejoy *et al.* would be useful to the understanding of the Wolff rearrangement for more complex molecules.

In Section 3.2, we introduce the general theoretical underpinnings of a calculation of the ketene isomerization rate via the oxirene intermediate. Results are presented in Section 3.3 and Section 3.4 concludes.

3.2. Summary of Theoretical and Computational Specifics

In comparing the results of theoretical calculations to experimentally measured quantities, the microcanonical rate is often the most detailed quantity that is available for comparison. The microcanonical isomerization rate can be expressed as

$$k_{iso}(E) = \frac{N(E)}{2\pi\hbar\rho(E)}, \tag{3-3}$$

where $\rho(E)$ is the density of reactant (ketene) states per unit energy – which is a smooth, almost constant function of energy over the relevant region. In most cases, $\rho(E)$ can be easily estimated using the Whitten-Rabinovitch approximation [98, 99]or the Beyer-Swinehart algorithm, [20] although experimental and anharmonic *ab initio* state densities are often available, as is the case for ketene. $N(E)$ is the cumulative reaction (here isomerization) probability (CRP), which contains all the aspects of the isomerization process and whose calculation is the central task.

3.2.1. The Cumulative Reaction Probability

The development of theoretical methods for calculating CRPs has been a major focus of our research group in the last few years, so the present application is an excellent test of this methodology. Seideman and Miller's [31] expression for the CRP is

$$N(E) = 4tr[\hat{G}(E)^*\hat{\epsilon}_p\hat{G}(E)\hat{\epsilon}_r], \tag{3-4}$$

where $\hat{G}(E)$ is the Greens function,

$$\hat{G}(E) = (E + i\hat{\epsilon} - \hat{H})^{-1}, \tag{3-5}$$

$\hat{H}$ being the total Hamiltonian for the ketene molecule and $\hat{\epsilon}$ an absorbing potential to enforce outgoing wave boundary conditions. $\hat{\epsilon}_r$ ($\hat{\epsilon}_p$) is the part of the absorbing potential in the reactant (product) region, *e.g.* the left (right) dotted curves in Figure 3-1; $\hat{\epsilon} = \hat{\epsilon}_r + \hat{\epsilon}_p$. One may think of this quantum mechanical expression for the CRP as analogous to a classical trajectory calculation in which one starts trajectories in the left ketene well (*cf.* Figure 3-1), with initial conditions sampled from a microcanonical distribution, and runs them to determine the fraction that reach the right hand ketene well, terminating them as soon as they exit the double barrier region into the product well. In this quantum calculation we are thus by-passing the problem of describing the dynamics of highly vibrationally excited ketene itself and only calculating the microcanonical reactive flux (which is the CRP).

Even with this limited treatment of the dynamics, however, it is not possible to carry out the calculation in its full dimensionality of $F = 3N\text{-}6 = 9$ degrees of freedom (with total angular momentum J=0). We thus carry out a CRP calculation including f degrees of freedom, obtaining $N_f(E)$, and then fold in the other uncoupled degrees of freedom by microcanonical convolution,

$$N(E) = \sum_{\underset{\sim}{n}=0}^{\infty} N_f\left(E - \varepsilon_{\underset{\sim}{n}}^{F-f}\right), \tag{3-6}$$

where $\{\varepsilon_{\underset{\sim}{n}}^{F-f}\}$ are the energy levels – approximated as harmonic oscillators – for the F-f uncoupled degrees of freedom – i.e., $\underset{\sim}{n} = n_{f+1}, \ldots, n_F$, and

$$\varepsilon_{\underset{\sim}{n}}^{F-f} = \sum_{j=f+1}^{F} \hbar\omega_j\left(n_j + \frac{1}{2}\right). \tag{3-7}$$

This is the idea of "dimensionality reduced" approximations [24, 100], and for $f=1$ is the standard expression for one-dimensional tunneling corrections to microcanonical transition state theory. [25]

Treating vibrational modes in this way is similar to the J-shifting approximation, [24, 100, 101] which estimates rate constants and cross sections using only $J=0$ calculations. This estimate is made by ignoring Coriolis coupling, and assuming that the geometry used to estimate the centrifugal coupling strongly resembles the transition state geometry. The J-shifting approximation to the thermal rate constant for $D+H_2(v=1)$ has given excellent agreement the exact quantum results. [102]

Described in terms of the normal modes of the oxirene intermediate, the ketene isomerization reaction has 3 strongly coupled degrees of freedom, and 6 degrees of freedom that are only weakly coupled to the reaction coordinate. This makes the n-shifting approximation in equation 3-6 useful in calculating the overall isomerization rate.

3.2.2. The Potential Energy Surface

The stability of the oxirene intermediate has been the subject of a great deal of controversy in the quantum chemistry community. Scott *et al.* [84] have performed the most detailed calculation of the reaction path to date. At the CCSD(T)/6-311G(df,p) level of theory, they find a broad, corrugated well between the transition states that separate the two ketene structures, as shown in Figure 3-2.

The oxirene well, however, is only slightly stable and lies at an energy above the energy for formylmethylene. Frequencies for the oxirene structure have been obtained at the CCSD(T)-fc/TZ2P(f,d) level of theory by Vacek *et al.* [85]. This level of theory also shows oxirene to be a stable point on the potential energy surface.

Other levels of theory, including density functional theory, have given an imaginary frequency for the ring-opening mode of oxirene [103]. Most of these calculations also give a fairly broad central well with transition states between the formylmethylene structures and the associated ketene structures. The fact that the region between the two outer

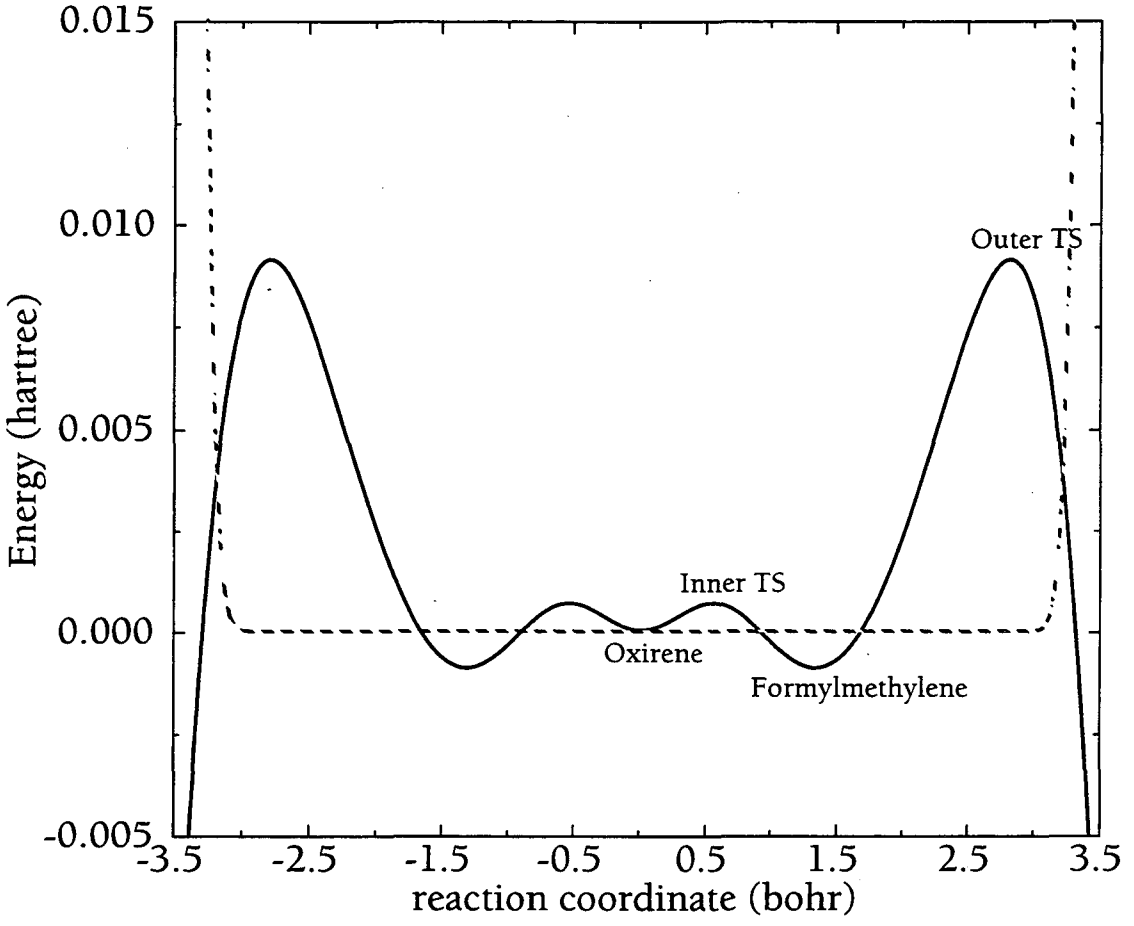

Figure 3-2. The 1-d potential energy surface

A plot along the reaction coordinate showing the 1-dimensional potential energy surface (solid line) and the absorbing potential (dotted line). The critical points are labeled with the names of the structures along the reaction coordinate that were calculated in reference [84].

transition states is not a single minimum (as indicated in the simplified Figure 3-1) does not change the discussion in the introduction about resonance tunneling, but it does suggest that the dynamics of the resonance intermediate may be quite complex.

We have used normal coordinates referenced to the oxirene geometry,

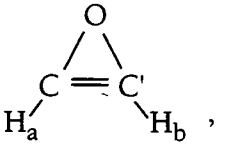

(3-8)

to construct a potential energy surface in the region of Figure 3-2, incorporating all information available from *ab initio* [84, 85, 103] calculations as well as possible. From these calculations, we identify at least three degrees of freedom that play active roles in the isomerization process. (The carbon-carbon and one of the carbon-hydrogen bond lengths are largely unchanged throughout the isomerization.)

The first important normal mode coordinate – the one we identify as the reaction coordinate – involves mainly oxygen and hydrogen atom motion. Displacement along this normal mode describes most of the structural differences between oxirene and the intermediates that lie between oxirene and ketene.

We have identified the other two quantum degrees of freedom in terms of two of the *local* modes of oxirene. The second degree of freedom that we include in the quantum calculation is a linear combination of the a_2 CH asymmetric out-of-plane mode and the b_1 CH symmetric out-of-plane mode. This corresponds to the out-of-plane motion of H_a relative to the CCO plane, a motion which has a frequency of approximately 514 cm^{-1}.

The third degree of freedom is a linear combination of the b_2 CH asymmetric rock and the a_1 CH symmetric rock. This combination corresponds to the in-plane swing of H_b towards the middle of the CC bond, and has a frequency of approximately 873 cm^{-1}.

We make some simplifying assumptions in calculating the frequencies of these local modes. The first assumption is that the asymmetric and symmetric normal modes are the normal modes for a system with two local modes which have identical frequencies. Next, we assume that the coupling between these local modes is positive. With these two assumptions, it is easily shown that the frequency of the symmetric normal mode is the same as the frequency of the constituent local modes. This is the lower of the two frequencies for each pair of normal modes listed above.

The form of the potential energy surface that we have used to perform this calculation is given by

$$V(s,\underline{Q}) = V_{1d}(s) + \sum_{j=2}^{3} k_j \left(Q_j + \frac{f_j(s)}{k_j} \right)^2, \tag{3-9}$$

$$V_{1d}(s) = a_2 s^2 + a_4 s^4 + a_6 s^6 + c s^2 e^{-ds^2}, \text{ and} \tag{3-10}$$

$$f_j(s) = d_j s^4. \tag{3-11}$$

The parameters for the 1-d potential $V_{1d}(s)$ were obtained by fitting to the energies and structures in reference [84]. A plot of this fit is given in figure 3-2. A comparison of the energies and frequencies of the calculated fit to the *ab initio* calculations is given in Table 3-1.

		Oxirene	inner TS	Formyl-methylene	outer TS
Energy (kJ/mol)	best fit V_{1d}	0	1.8	-2.4	23.9
	Ref. [84][a]	0	1.9	-2.0	23.9
ω (cm^{-1})	best fit V_{1d}	134	141 *i*	152	277 *i*
	Refs. [84][b] and [85]	163[c]	133 *i*	328	409 *i*

Table 3-1. Properties of the best-fit 1-d potential surface

Energies and frequencies for the critical points along the reaction coordinate. Energies are relative to the oxirene structure.

a. geometries are optimized at the CCSD(T)/6-311G(df,p) level, and energies are calculated using a mean of CCSD(T)/cc-pVTZ(f) and CCSD(T)/cc-pVTZ(g) values.

b. calculated at the CCSD(T)/6-31G(d) level.

c. calculated at the CCSD(T)-fc/TZ2P(f,d) level.

Frequencies for the two coupled degrees of freedom were obtained from the frequencies for the asymmetric hydrogen rock (in plane) and asymmetric hydrogen wag (out of plane) modes calculated in reference [85]. The coupling constants (d_j) for those two modes are obtained by using the geometries calculated in reference [84]. A contour plot of the potential energy surface as a function of s and Q_2 is shown in figure 3-5, and all the parameters used in constructing the potential energy surface are given in Table 3-2.

parameter	value
a_2	-2.3597×10^{-3} (hartree bohr^{-2})
a_4	1.0408×10^{-3} (hartree bohr^{-4})
a_6	-7.5496×10^{-5} (hartree bohr^{-6})
c	7.7569×10^{-3} (hartree bohr^{-2})
d	1.9769 (bohr^{-2})
k_2	1.0074×10^{-2} (hartree bohr^{-2})
d_2	-2.45182×10^{-4} (hartree bohr^{-5})
k_3	2.9044×10^{-2} (hartree bohr^{-2})
d_3	-8.54360×10^{-4} (hartree bohr^{-5})

Table 3-2. Parameters of the best-fit potential energy surface

3.2.3. Absorbing Boundary Conditions

Miller and Seideman [104, 105] developed an approach to calculating cumulative reaction probabilities using Absorbing Boundary Conditions (ABC's). In the original formulation, it allowed for easy calculation of the cumulative reaction probability in a DVR basis (see section 3.2.4) with the equation

$$N(E) = 4\sum_{j,j'} \epsilon_r(q_j) \, |\underline{G}_{j,j'}|^2 \, \epsilon_p(q_{j'}) \, , \tag{3-12}$$

where ϵ_r and ϵ_p are the DVR representations of the absorbing potentials in the reactant and product regions, and $\mathbf{G}$ is the DVR representation of the scattering Green's function, given by

$$\underline{G}(E^+) = (E\underline{I} - \underline{T} - \underline{V} + i\epsilon) \, . \tag{3-13}$$

In this Green's function, the standard convergence parameter, ε, has been replaced with the coordinate dependent absorbing potential, ϵ. The summation in equation 3-12 is derived from the original trace formula:

$$N(E) = \frac{1}{2}(2\pi\hbar)^2 tr\,[\hat{F}\delta(E-H)\,\hat{F}\delta(E-H)] \, , \tag{3-14}$$

where $\hat{F}$ is the flux operator and δ(E-H) is the microcanonical density operator. This formula is basis-set independent, and marks the point of departure for the P-matrix method that will be discussed in section 3.2.5.

The main reasons for using absorbing boundary conditions are that they allow one to treat a scattering problem as if it were a non-Hermitian bound system, and that they allow one to shrink the extent of the problem to the area immediately surrounding the interaction region. The second of these two advantages proved to be indispensable in calculating rates for ketene isomerization. The ABC formalism has been recently extended to allow for calculations of state-to-state [105, 106, 107] and half-state-selected [106, 107] reaction probabilities with great success.

The absorbing potential, $\epsilon(s,Q_2,Q_3)$, that we use in our calculations is given by

$$\epsilon(s, Q_2, Q_3) = a\left(\frac{r - r_0}{r_{max} - r_0}\right)^4 h(r - r_0) , \tag{3-15}$$

where

$$r = \sqrt{c_s|s|^2 + c_2|Q_2|^2 + c_3|Q_3|^2} . \tag{3-16}$$

We place the beginning of the absorbing potential, r_0, just after the final barriers to isomerization. The absorbing potential needs to rise fast enough to absorb the flux resulting from the rapid drop off of the potential energy, so a polynomial of at least degree 3 is required for the form of ϵ. The end of the absorbing potential, r_{max}, is placed at the edge of the grid. This edge is located just far enough outside the barrier to isomerization to assure convergence. Typical values for r_{max}, and for the constants in equations 3-15 and 3-16 are presented in Table 3-3.

3.2.4. The Basis Set

We have used a discrete variable representation (DVR) (i.e., a basis set of grid points) to represent the operators in equation 3-4, specifically the sinc-function DVR of Colbert

parameter	value
r_0	2.7 (bohr)
c_s	1
c_2	0.9
c_3	1
a	0.01 (hartree bohr^{-4})
r_{max} (1d)	3.45 (bohr)
(2d)	4.3 (bohr)
(3d)	5.6 (bohr)

Table 3-3. Parameters of the Absorbing potential

and Miller. [32] This is a convenient representation for a number of reasons. The potential energy operator is diagonal in a DVR, and the kinetic energy operator is the sum of 1-dimensional kinetic energy matrices. These two features of the DVR combine to give a sparse Hamiltonian matrix. The matrix inverse that is required to obtain the Green's function can therefore be solved with some of the sparse matrix techniques that will be discussed in section 3.2.6.

The basis functions themselves are an orthonormal set given by:

$$\langle x \mid x_i \rangle = \frac{\sin\left(\pi \frac{(x - x_i)}{\Delta x}\right)}{\pi (x - x_i)}. \tag{3-17}$$

In this equation, Δx is the grid spacing of the DVR grid, which is obtained by estimating the deBroglie wavelength of the highest kinetic energy that needs to represented:

$$\Delta x = \frac{1}{N_B}\left(\frac{2\pi}{\sqrt{2m\,(E_{high} - V_{low})/\hbar^2}}\right). \tag{3-18}$$

N_B is the number of grid points in one complete deBroglie wavelength. This number is typically taken to be around 3.7. E_{high} is the highest energy in the problem, and V_{low} is the lowest point on the potential energy surface.

For the three cartesian degrees of freedom that we used in this work, the kinetic energy operator for each degree of freedom can be expressed in this basis set as:

$$T_{ii'} = \frac{\hbar^2}{2m\Delta x^2}(-1)^{i-i'}\begin{cases} \frac{\pi^2}{3} & i = i' \\ \frac{2}{(i-i')^2} & i \neq i' \end{cases} \tag{3-19}$$

The first part of the calculation involves laying down a primitive rectangular grid in all 3 degrees of freedom. The primitive rectangular grid required to go from reactants to products would be very large, so the primitive grid is truncated based on the potential at the various grid points. If

$$V(s_i, \underset{\sim}{Q}_{jk}) > V_{cut}, \tag{3-20}$$

then the point (i,j,k) is removed from the grid. This procedure drastically reduces the number of grid point necessary to obtain the reaction probability. V_{cut} was taken to be twice the largest energy for which a value for $N(E)$ was required.

3.2.5. Evaluation of the Trace

Manthe and Miller [37] have shown that an efficient way to evaluate the trace in Eq. 3-4 is to introduce the reaction probability operator $\hat{P}(E)$, defined by

$$\hat{P}(E) = 4\hat{\epsilon}_r^{1/2}\hat{G}(E)^* \hat{\epsilon}_p\hat{G}(E)\hat{\epsilon}_r^{1/2}, \tag{3-21}$$

so that Eq. 3-4 for $N(E)$ becomes

$$N(E) = tr[\hat{P}(E)]. \tag{3-22}$$

(Since the absorbing potential matrices are diagonal, the square roots in Eq. 3-21 cause no problems.) This expression can be derived from equation 3-14 using cyclic permutation of the operators within the trace, and by observing that

$$\delta(E-H) = -\frac{1}{\pi} Im\, \hat{G}(E^{+}) . \tag{3-23}$$

One must also note that the flux operator, $\hat{F}$, is defined in terms of a surface in coordinate space that separates the reactant region from the product region. If one specifies this surface as $f(s, \underline{Q}) = s_F$, *i.e.* the surface is taken when the reaction coordinate, s, is held at a constant value s_F, then the flux operator may be written as

$$\hat{F} = \frac{i}{h} \{\hat{H}, h[f(\hat{s}, \hat{\underline{Q}})]\} . \tag{3-24}$$

Manthe and Miller also show that the eigenfunctions of the P-operator all lie between 0 and 1. The cumulative reaction probability is expressed in terms of the eigenvalues $\{p_k(E)\}$ as

$$N(E) = \sum_k p_k(E) . \tag{3-25}$$

These eigenvalues have been termed "eigenreactionprobabilities", and roughly correspond to the probability of transmission through a given open channel at the transition state.

The great strength of this method is that it allows us to use iterative methods to obtain only those eigenvalues that contribute to the reaction probability. This provides a simple convergence test for the iterative methods that are discussed in the next section. Typically, one only needs to find the lowest few eigenvalues of a very large matrix. The computational savings due to this fact are significant.

3.2.6. Methods for Solving Sparse Linear Systems

The preferred method [38] for finding the Greens function in equation 3-12 is to use LU-decomposition followed by back-solving to obtain the columns of the Greens function:

$$(H - EI + i\epsilon)\, G_n = I_n . \tag{3-26}$$

Here, I_n and G_n are the nth columns of the identity matrix and Green's functions, respectively. The LU-decomposition is done once, and backsolving is done for each column of the Green's function that is required. This is an extremely efficient and reliable way of obtaining the inverse of small and medium sized matrices, and for $N \times N$ matrices, the number of operations required to perform the inverse scales with N^3.

When the size of the grid and the resulting Hamiltonian matrix becomes too large, it becomes impossible to store either the Hamiltonian, the Green's function, or the P-operator. This limit is reached at around 7500 grid points on workstations with 1 GByte of core memory. The number of grid points required to treat three quantum mechanical degrees of freedom in the ketene isomerization is approximately 48,000, so a different technique is required.

Methods based on Krylov subspaces [39, 40] of the operator are extremely good at converging the high end of the eigenvalue spectrum. This is ideal for the P-operator, as the higher eigenvalues are the ones that contribute most to the cumulative reaction probability. One needs to find only the non-zero eigenvalues of P, which is typically a very small subset of the full set of eigenvalues. These eigenvalues can usually be obtained in only a few iterations of the Lanczos algorithm.

The algorithm is summarized as follows:

We start with an arbitrary initial vector $\underline{v}_0$, which is often chosen to be a random vector. The Lanczos recursion formula for a Hermitian operator is as follows

$$b_{i+1}\underline{v}_{i+1} = \hat{P}\underline{v}_i - a_i\underline{v}_i - b^*_i\underline{v}_{i-1}, \tag{3-27}$$

where

$$a_i = \left(\underline{v}_i, \hat{P}\underline{v}_i\right), \tag{3-28}$$

and

$$b_1 \underline{v}_1 = \underline{v}_0 . \tag{3-29}$$

The inner product in equation 3-28 is the hermitian inner product. We now define $\tilde{P}$ as the representation of the P operator in the Krylov basis of $V^m = \{\underline{v}_1, \underline{v}_2, \ldots, \underline{v}_m\}$. Since $\hat{P}$ is hermitian, it is easy to show that $\tilde{P}$ is a tridiagonal matrix of the form:

$$\tilde{P} = \begin{bmatrix} a_1 & b_2^* & & \\ b_2 & a_2 & b_3^* & \\ & b_3 & a_3 & \ddots \\ & & \ddots & \ddots \end{bmatrix} . \tag{3-30}$$

This matrix can be used directly to calculate the eigenvalues of P. Due to round-off errors, however, the elements of the vectors, $\underline{v}_i$,can deviate from their exact values. This can introduce spurious or 'ghost' eigenvalues or multiple copies of correct eigenvalues into the spectrum for $\tilde{P}$. To alleviate this problem, one may explicitly reorthogonalize the vectors, and obtain the following recursion relation:

$$c_{i,i-1} \underline{v}_i = \hat{P} \underline{v}_{i-1} - \sum_{j=0}^{i-1} c_{j,i-1} \underline{v}_j , \tag{3-31}$$

where

$$c_{i,j} = \left(\underline{v}_i, \hat{P} \underline{v}_j \right) . \tag{3-32}$$

Since we are looking for the trace of the P operator in this representation, all we really need are the diagonal elements of P:

$$N(E) = \sum_{i=0}^{N_{kry}} \left(\underline{v}_i, \hat{P} \underline{v}_i \right) = \sum_{i=0}^{N_{kry}} c_{i,i} , \tag{3-33}$$

where N_{kry} is the number of Krylov iterations that have been performed.

Since the Lanczos algorithm obtains the highest lying eigenvalues of the P operator first, the number of iterations required to converge $N(E)$ is on the order of $N(E)$ itself. This amounts to a built-in convergence test of the method – when $N(E)$ is stable, no more Lanczos iterations are required.

Every operation of the matrix $\underset{\sim}{P}$ onto a vector in Eq. 3-27 requires two operations of the Green's function matrix onto a vector (i.e., the various matrices in $\hat{P}(E) = 4\hat{\epsilon}_r^{1/2}\hat{G}(E)^* \hat{\epsilon}_p\hat{G}(E)\hat{\epsilon}_r^{1/2}$ multiply sequentially from the right). The operation of the Greens function matrix onto a vector effectively means that one must solve the set of linear equations,

$$\underset{\sim}{A} \cdot \underset{\sim}{x} = \underset{\sim}{b}, \tag{3-34}$$

where the vector $\underset{\sim}{b}$ is given and $\underset{\sim}{A} = (E + i\underset{\sim}{\epsilon} - \underset{\sim}{H})$, and this is the primary computational task. Use of the Lanczos method above with the P-operator/matrix greatly reduces the number of Green's function operations that are required and is why it was such an important step forward.

There is, of course, an enormous literature on the solution of the linear algebra problem in Eq. 3-34. Our present matrix $\underset{\sim}{A}$ is complex symmetric, large, but very sparse. We have made most use of the generalized minimum residual (GMRES),[35] and more recently the quasi-minimum residual (QMR) algorithms.[36] These are both Krylov-based algorithms, and they allow one to use pre-conditioners. I.e., if $\underset{\sim}{A}_0$ is an approximation to $\underset{\sim}{A}$ that itself is easily invertible, then one writes Eq. 3-34 as

$$\underset{\sim}{A}' \cdot \underset{\sim}{x} = \underset{\sim}{b}', \tag{3-35}$$

where

$$\underset{\sim}{A}' = \underset{\sim}{A}_0^{-1} \cdot \underset{\sim}{A} \tag{3-36}$$

$$\underset{\sim}{b}' = \underset{\sim}{A}_0^{-1} \cdot \underset{\sim}{b}, \tag{3-37}$$

and then generates a Krylov basis using $\underset{\sim}{A}'$. GMRES is the most efficient procedure on the basis of the number of such iterations, but it requires that one store (and explicitly orthogonalize) all the Krylov vectors. QMR is not as efficient as GMRES on the basis of number of iterations, but since it requires the storage of only a few Krylov vectors, its cost (i.e., computational time) per iteration is much less. QMR finds the inverse by a quasi-minimization of the residual at each iteration. It is based on the look-ahead Lanczos algorithm which is used to find approximate eigenvalues of large non-Hermitian matrices. We stop the QMR iterations when the residual for the Green's function has dropped below 10^{-4}.

We have found that a diagonal preconditioner gives the best performance with QMR, i.e.

$$(\underset{\sim}{A}_0)_{i,j} = (\underset{\sim}{A})_{i,j}\delta_{ij} \tag{3-38}$$

in equation 3-36 above. Other preconditioners, notably the Symmetric Successive Over Relaxation (SSOR) preconditioner resulted in a smaller number of iterations, but the costs associated with finding the inverses of upper and lower Hessenberg matrices made it a less attractive preconditioner.[108, 109] For the particular matrices used in this calculation, SSOR was often more expensive than having no preconditioner at all.

3.3. Results

3.3.1. Isomerization Rate using one degree of freedom

The best-fit single mode potential energy surface is shown in figure 3-2, and the calculated cumulative reaction probability ($N_{1d}(E)$) for this PES is shown in figure 3-3.

$N_{1d}(E)$ was used to calculate the isomerization rate using the other 8 vibrational modes at the outer transition states as uncoupled harmonic oscillators. The isomerization rate is shown as a solid line in figure 3-4. In all calculations, the experimentally measured

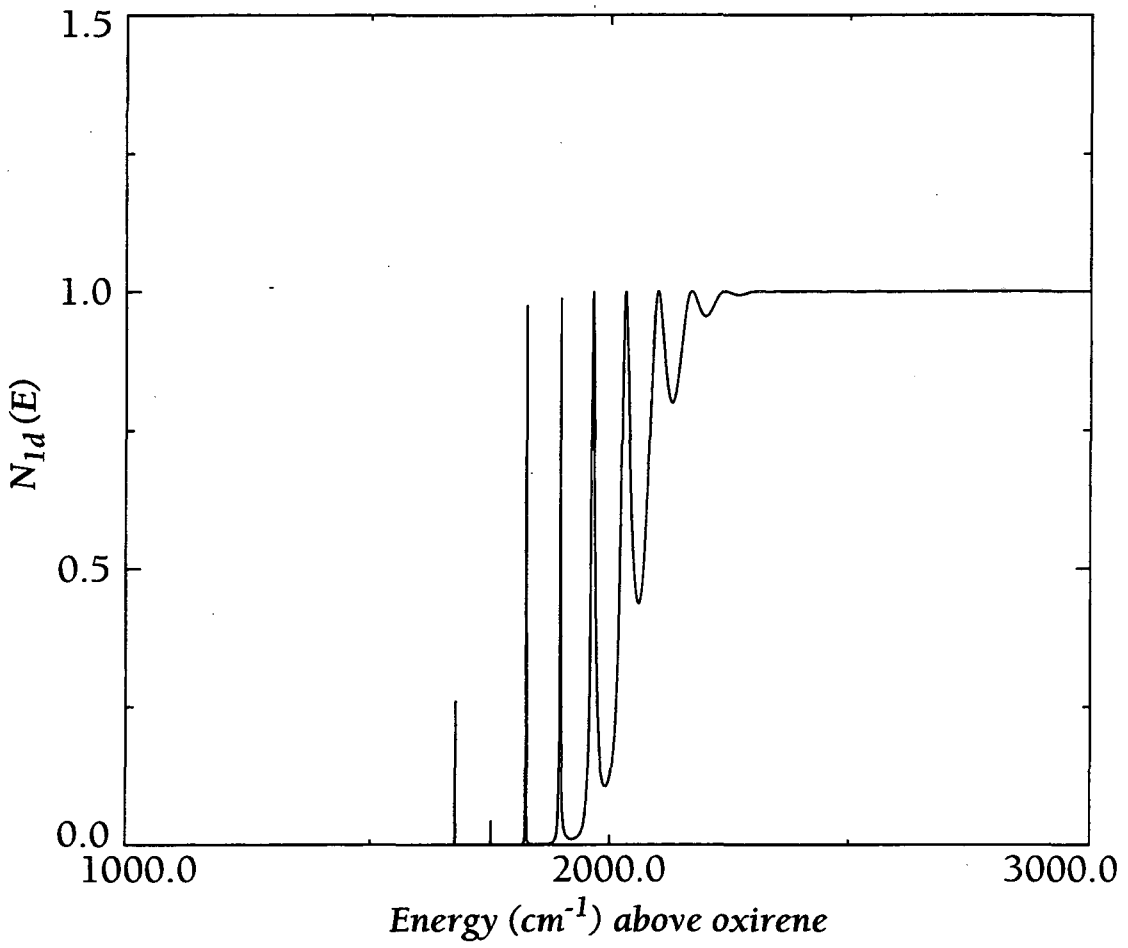

Figure 3-3. 1-d $N(E)$

The calculated cumulative reaction probability ($N(E)$) for the potential shown in figure 3-2.

[10, 14, 15, 11, 13] density of states (4.5×10^4 states/cm^{-1}) for a reactant ketene molecule with 28,000 cm^{-1} of vibrational energy was used.

With a single quantum degree of freedom, the rate shows resonant features with widths of ~1-5 cm^{-1} that are spaced ~70-80 cm^{-1} apart. From the $N(E)$ calculation in figure 3-3, this spacing corresponds to a progression of tunneling resonances within the one-dimensional oxirene well. Agreement with the experimental rate is surprisingly good, giving qualitative matches between the number of observed features and the absolute magnitudes of the rates.

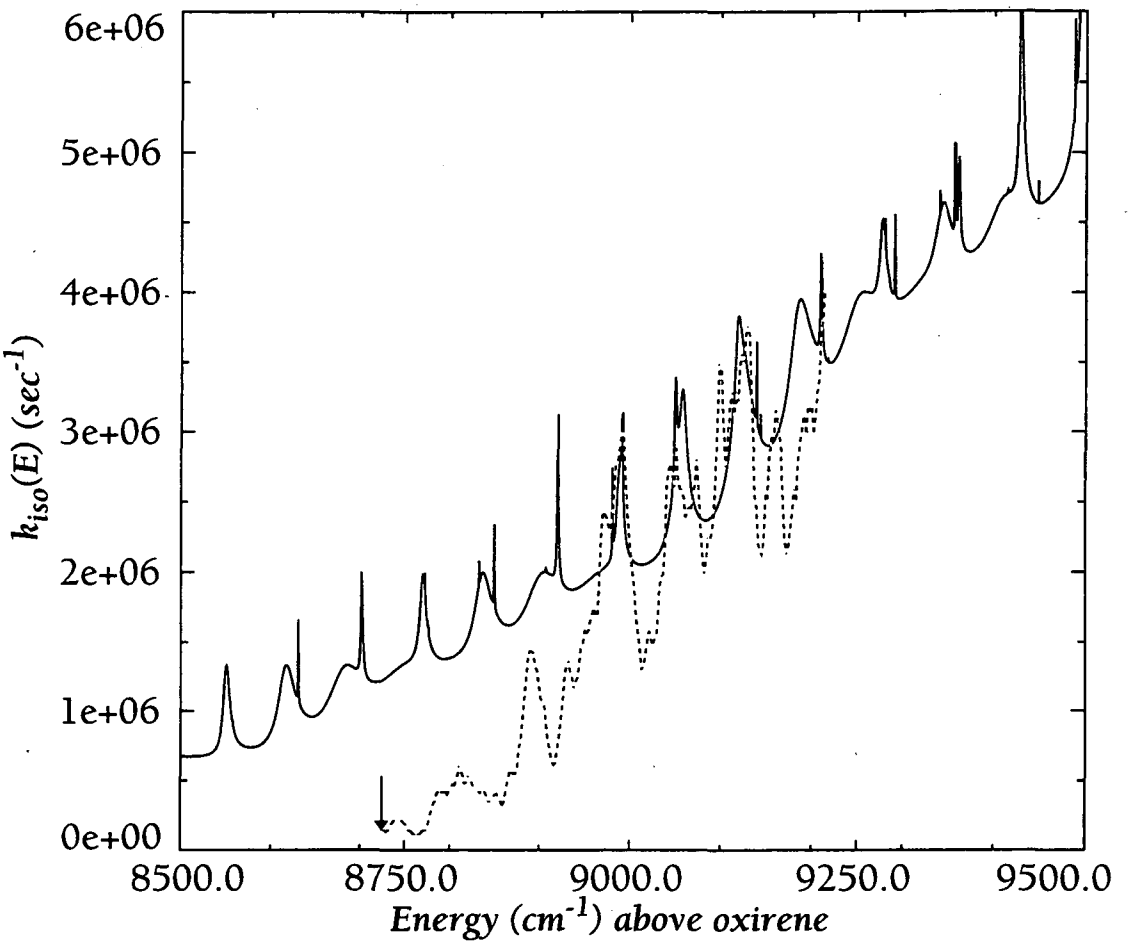

Figure 3-4. 1-d $k_{iso}(E)$

The calculated isomerization rate for the 1-dimensional surface shown in figure 3-2. The dotted line is the experimentally obtained reaction rate from reference [12].

3.3.2. Isomerization Rate using two degrees of freedom

Using the two-mode potential energy surface displayed in figure 3-5 to calculate the microcanonical isomerization rate, two additional and striking aspects of the energy dependence of the rate are observed. Figure 3-6 shows the rate calculated using the reaction coordinate and the *out-of-plane* hydrogen mode as the two coupled degrees of freedom, and treating the other 7 modes as uncoupled harmonic oscillators. Resonant lineshapes appear in the 2-dimensional rates that resemble Fano lineshapes instead of the pure Breit-Wigner peaks observable in the 1-d rates. This indicates that the back-

ground phase at those energies is non-zero, which we believe to be a signature of overlapping resonant contributions to the cumulative reaction probability.[110]

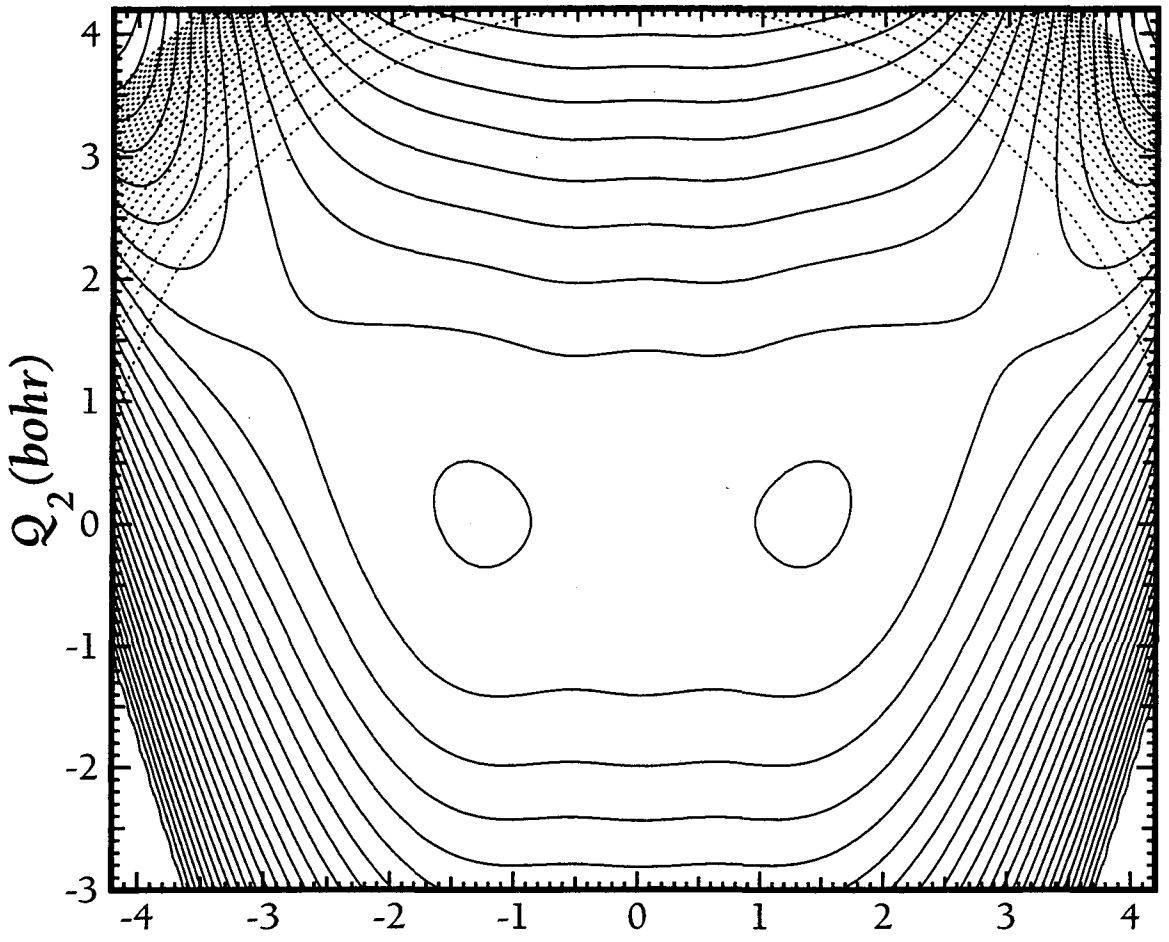

Figure 3-5. 2-d potential energy surface

A contour plot showing the 2-dimensional potential energy surface (solid contours) and the absorbing potential (dashed contours). The two degrees of freedom represented in this plot are the reaction coordinate, s, and the hydrogen out-of-plane local mode, Q_2.

The other striking feature is that there are resonant features that are wider (~10 cm^{-1}) than those observed in the one-degree of freedom rate. We believe that these features correspond to Feshbach, energy-transfer or dynamical resonances that occur at energies above the barrier to isomerization. These dynamical resonances appear because the multi-mode potential energy surface has a strongly bent region between the two outer

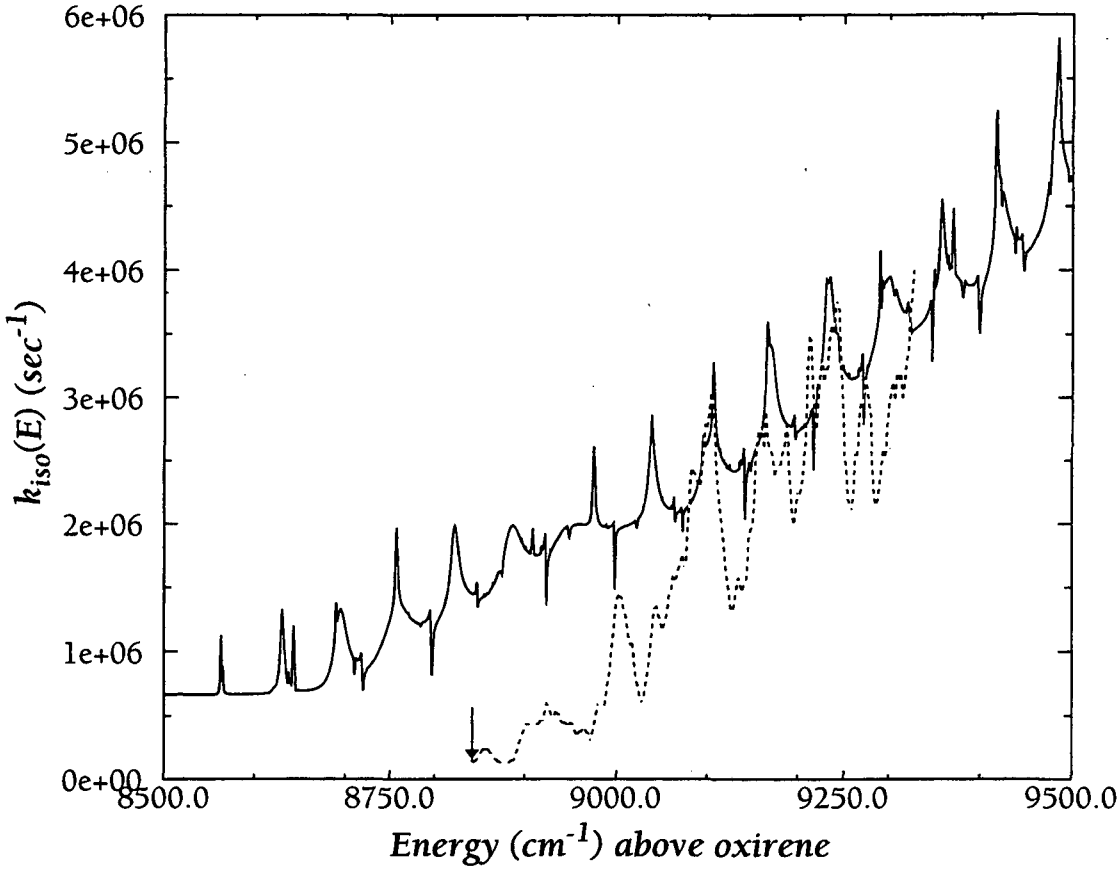

Figure 3-6. 2-d $k_{iso}(E)$

The calculated isomerization rate for the 2-dimensional surface shown in figure 5. The dotted line is the experimentally obtained reaction rate from reference [12].

transition states (cf. Fig.) which acts as a dynamical bottleneck even at total energies above the outer transition state energies.

Figure 3-7 shows the 2-dimensional rate calculated using the reaction coordinate and the *in-plane* hydrogen mode as the two coupled degrees of freedom, and treating the other 7 modes as uncoupled harmonic oscillators. As in the other 2-dimensional calculation, resonance widths are wider (10 cm^{-1}) than in the 1-dimensional calculation and the spacings between the wide resonant features are on the order of 70-80 cm^{-1}. Most of the peaks are pure Breit-Wigner-type peaks, which indicates that there are very few overlapping resonances when the in-plane mode is used as the second coupled degree

of freedom. This is due in large part to the higher vibrational frequency of the in-plane mode relative to the out-of-plane mode's vibrational frequency.

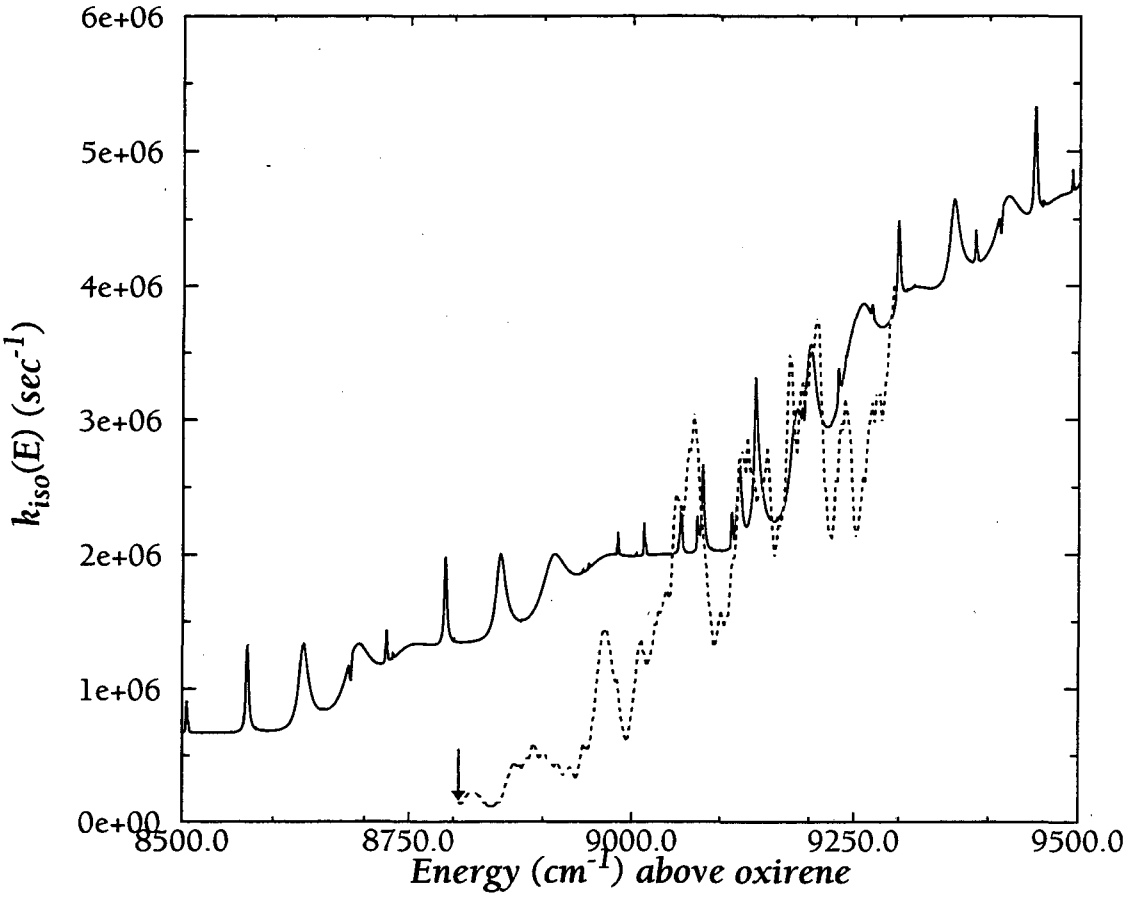

Figure 3-7. 2-d $k_{iso}(E)$

The calculated isomerization rate for a 2-dimensional surface using the reaction coordinate, s, and the hydrogen in-plane local mode, Q_3. The dotted line is the experimentally obtained reaction rate from reference [12].

3.3.3. Isomerization Rate using three degrees of freedom

We have also calculated $k_{iso}(E)$ for three coupled degrees of freedom (i.e., the reaction coordinate, the in-plane, and the out-of-plane hydrogen local modes are coupled according to the parameters for the potential energy surface given in Table 3-2). The isomerization rate for the three-dimensional calculation is shown in figure 3-8. It exhibits broad (10 cm^{-1}) features similar to the ones that were observed in the two-dimen-

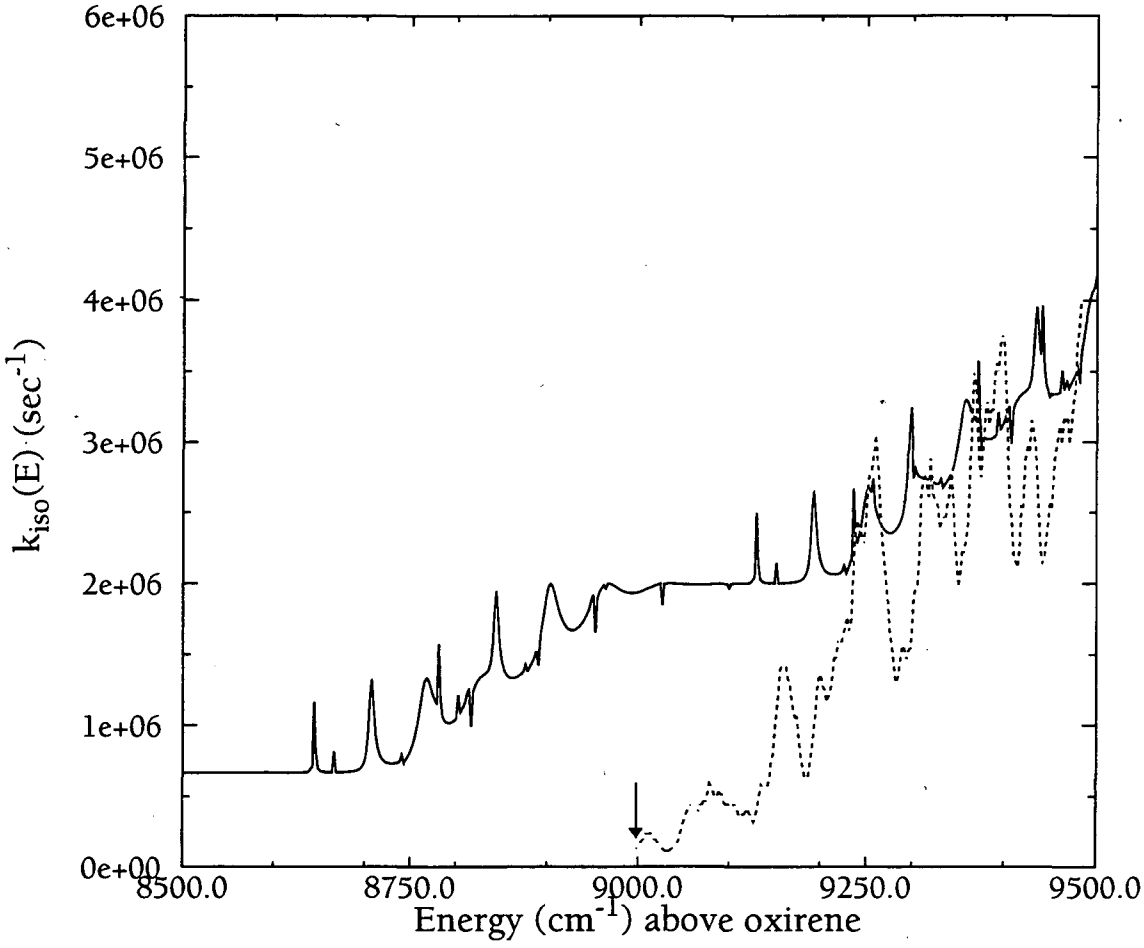

Figure 3-8. 3-d $k_{iso}(E)$

The calculated isomerization rate for a 3-dimensional surface using the reaction coordinate, s, and both the hydrogen out-of-plane local mode, Q_2, and the in-plane local mode, Q_3. The dotted line is the experimentally obtained reaction rate from reference [12].

sional rates, as well as a few overlapping resonances similar in character to the ones present in figure 3-7.

We attribute the narrow (1 cm^{-1}) features that are similar to the ones observed in the 1-dimensional calculations to tunneling resonances. These features are observed at energies below the barriers to isomerization (at ~ 8100 cm^{-1} in Figs. 3-4, and 3-6 through 3-8). The narrow features can also be observed at higher energies because of repetitions due to the uncoupled harmonic modes. At energies well above the barrier to isomeriza-

tion, we again see the broad features that we attribute to Feshbach resonances that were observed in the 2-dimensional isomerization rates.

3.4. Discussion

In figures 3-4, 3-6, 3-7, and 3-8, the calculated rates (solid lines) are plotted along with the experimental rates (dashed lines). However, since the present experiments determine the isomerization rate indirectly, i.e., from the exchange yield of the labeled carbon atom in the dissociation of ketene into CO and CH_2, they cannot measure the isomerization rate below this dissociation threshold. The barrier to dissociation lies slightly above the barrier for the isomerization, and the relative energies of these two barriers are only known to within a few hundred cm^{-1}, so we have adjusted the zero of energy for the experimental rate to illustrate the kind of agreement that our calculations can give with the experimental rates. The energy that we have assumed as the barrier to dissociation is marked with an arrow along the energy axis in each of these figures. It would be very useful to have experimental results for the isomerization rate below the dissociation threshold, for this would confirm or deny the existence of true tunneling resonances that lie below the barrier to isomerization.

Additionally, by placing absorbing potentials immediately outside the outer transition state between the oxirene well and ketene, we have eliminated any interaction between the dynamics within the ketene wells and the oxirene region. It is possible that these interactions could alter the theoretically calculated rates to some degree. However, these calculations are performed at energies where there is a near-continuum of states in the ketene well, and we expect that the mixing of the ketene states that occurs prior to isomerization will average out the effects of the interaction between the two regions.

The model potential surfaces presented in Section 3.2 are obviously not close enough to the true surface to give us quantitative agreement with the experimental rate. Also, although we have included up to three of the most strongly coupled degrees of freedom relevant to the isomerization process, incorporating other degrees of freedom fully dynamically (and not just via the reduced dimensionality approximation) will undoubt-

edly change the results somewhat. Nevertheless, we do see qualitative similarities between the present calculated rates and the experimental results. The average width and spacing of the features in the isomerization rate are represented well in our calculations, leading us to believe that we have included most of the important large-scale features of the potential energy surface in our current model.

Perhaps the most definite conclusion that we can draw is that the resonance structure in the isomerization rate is not from purely tunneling resonances. Tunneling is the only decay mechanism of a metastable oxirene state in one dimension, but the widths of the resonant features in the one dimensional calculation are much narrower than the structure seen experimentally. Multidimensional models allow also for Feshbach, or energy-transfer (dynamical) resonances: here the metastable state has enough total energy to dissociate (without tunneling) but not enough energy in the reaction coordinate; the decay rate (resonance width) is determined in this case by the rate of energy transfer from a "bath" mode into the reaction coordinate. Both tunneling and multimode coupling are of course included in the multidimensional calculations, and the significantly broader resonance features indicate that Feshbach-type resonances make a very significant contribution to the ketene isomerization. This is easily understood from the strong curvature seen in the multidimensional potential energy surfaces.

4 Dynamics of the Photodissociation of Triplet Ketene

Abstract

Calculations of the microcanonical dissociation rate for vibrationally excited ketene on the first excited triplet surface (T_1) are presented. The calculations utilize the quantum reactive scattering methodology of absorbing boundary conditions (ABC) with a discrete variable representation (DVR) to obtain the cumulative reaction probability for dissociation over the barrier. Model 1- and 2- degree of freedom potential energy surfaces for the T_1 surface were obtained by fitting to the best available *ab initio* structures, energies, and frequencies. The dissociation rates in these reduced-dimensionality calculations give good overall agreement with the experimentally measured rates, although the step-like features seen in the experiments are washed out by the tunnelling through the narrow barrier predicted in the ab initio calculations. Further model calculations reveal that a barrier frequency of approximately 50-100 i cm^{-1} is required to recover the step structure seen experimentally, which suggests that there is either another transition state region on the T_1 surface farther out towards the product channel, or that there is surface-hopping dynamics taking place between the T_1 and S_0 ketene potential energy surfaces, or that the *ab initio* barrier frequency is simply too large.

4.1. Introduction

In a recent series of experiments, Moore *et al.* have reported on a number of fascinating aspects of the dynamics of ketene photodissociation. [10, 11, 12, 13, 14, 15, 16, 17, 18, 19] The internal isomerization of carbon-labeled ketene via the oxirene intermediate exhibited surprising structure in the energy dependence of the isomerization rate; [12, 13] the quantum dynamics of this process was the subject of the previous chapter. [113]

The photodissociation of singlet ketene onto the singlet methylene surface has also been studied in great detail because it was an excellent example of a barrierless bond-breaking process. [14, 15, 16] Product state distributions of this reaction have also been measured, giving varying degrees of agreement with statistical theories such as phase space theory (PST). [44, 114]

More recently, Kim, Lovejoy, and Moore [10, 11] have investigated the dissociation of triplet ketene onto the triplet methylene surface. Figure 4-1 shows a schematic of the surfaces and energies involved in the experiment. Kim *et al.* prepared rotationally cold ketene on the S_0 surface (see Fig. 4-1) in a supersonic molecular jet, and used a UV laser to excite the ketene to the first excited singlet surface (S_1), which then underwent intersystem crossing to the triplet (T_1) surface. The products of the photodissociation on the triplet surface, ${}^3B_1\ CH_2 + {}^1\Sigma^+\ CO$, were detected using laser-induced fluorescence (LIF) of the CO fragment.

At first glance, the dissociation on the triplet surface is a simple barrier process for which standard reaction rate theories (RRKM [56, 57, 58, 59] and Transition State Theory [25]) provide adequate descriptions of the process and reaction rates. Indeed, the reaction rates observed by Kim *et al.* are very close to the predictions of RRKM theory, and the energy dependence of the reaction rate seems to exhibit the classic staircase-like structure that would result from newly opening channels at the transition state. Upon closer inspection, however, Kim *et al.* found that not all of the detailed fine structures in the energy dependence of the reaction rate were explainable using standard RRKM theory. We therefore undertook a series of calculations of the dissociation rate of triplet ketene onto the triplet methylene surface in order to further elucidate the origin of these structures. This paper describes those calculations and reports their results.

The microcanonical dissociation rate can be expressed as

$$k_d(E,J) = \frac{N(E,J)}{2\pi\hbar\rho(E,J)}, \tag{4-1}$$

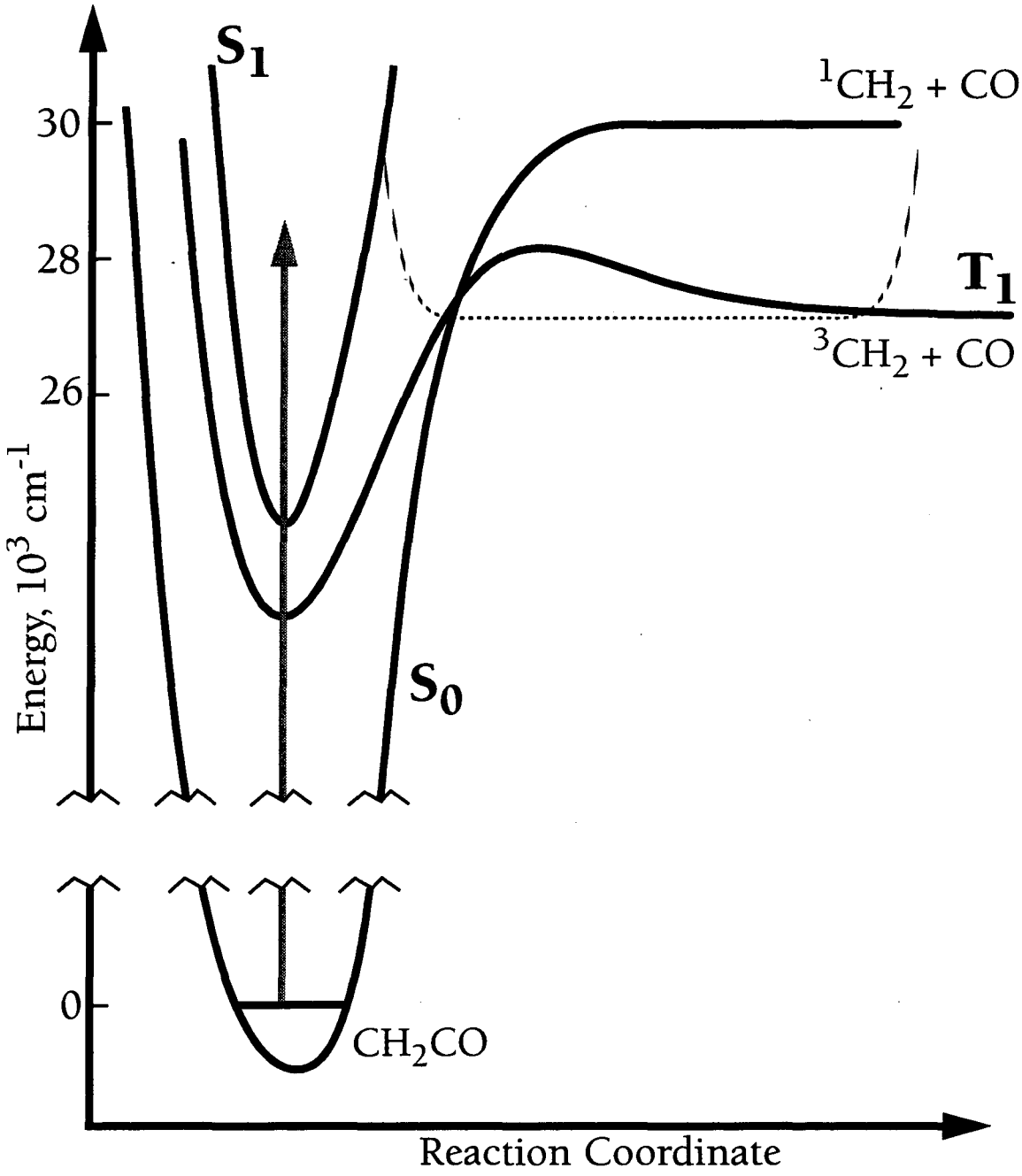

Figure 4-1. The energetics of the ketene dissociation experiments

A schematic depiction of the lowest three electronic surfaces of ketene along the reaction coordinate. In the experiment, ketene is photoexcited to the first excited singlet state (S_1), which then undergoes internal conversion to the ground electronic surface (S_0) or inter-system crosses to T_1. The dissociation can happen on either the S_0 or T_1 surfaces, which lead to the $^1CH_2$ + CO (Singlet channel) or $^3CH_2$ + CO (Triplet channel) products, respectively. The calculations in this chapter are of dissociation rates through the barrier region of the T_1 surface. The absorbing boundary potential used in this work is shown as a dotted line.

where $\rho(E,J)$ is the density of reactant (ketene) states per unit energy, which is a smooth function of energy and can be treated well using an empirically determined constant times the Whitten-Rabinovitch approximation for the density of states: [98]

$$\rho_{WR}(E,J=0) = \frac{(E+E_{zp})^{F-1}}{(F-1)!\prod_{i=1}^{F}\hbar\omega_i}, \tag{4-2}$$

where F is the number of vibrational modes of the ketene molecule, E_{zp} is the zero-point energy of ketene on the S_0 surface, and $\{\omega_i\}$ are the frequencies of the vibrational modes on the S_0 surface. The empirical constant multiplier has been measured by the Moore group in various experiments and was found to be 3.34. [10]

$N(E,J)$ is the cumulative reaction probability (CRP), which contains all the aspects of the dissociation process and whose calculation is the central task. The development of theoretical methods for calculating CRPs has been a major focus of our research group in the last few years, so the present application is an excellent test of this methodology. Seideman and Miller's [31] expression for the CRP is

$$N(E,J) = 4tr\left[\hat{G}_J(E)^*\hat{\epsilon}_p\hat{G}_J(E)\hat{\epsilon}_r\right], \tag{4-3}$$

where $\hat{G}_J(E)$ is the Greens function,

$$\hat{G}_J(E) = \left(E+i\hat{\epsilon}-\hat{H}_J\right)^{-1}, \tag{4-4}$$

$\hat{H}_J$ being the total Hamiltonian (for total angular momentum J) for the ketene molecule and $\hat{\epsilon}$ an absorbing potential to enforce outgoing wave boundary conditions. $\hat{\epsilon}_r$ ($\hat{\epsilon}_p$) is the part of the absorbing potential in the reactant (product) region, *e.g.* the left (right) dotted curves in Figure 4-1; $\hat{\epsilon} = \hat{\epsilon}_r + \hat{\epsilon}_p$. In practice, one may place the absorbing potential immediately outside the barrier region for the reaction, thereby by-passing the

problem of describing the dynamics of highly vibrationally excited ketene itself and only calculating the microcanonical reactive flux (which is the CRP).

Even with this limited treatment of the dynamics, however, it is not possible to carry out the calculation in its full dimensionality of $F = 3N\text{-}6 = 9$ degrees of freedom (with total angular momentum $J=0$). We thus carry out a CRP calculation including f degrees of freedom, obtaining $N_f(E)$, and then fold in the other uncoupled degrees of freedom by microcanonical convolution,

$$N(E) = \sum_{\underline{n}=0}^{\infty} N_f\left(E - \varepsilon_{\underline{n}}^{F-f}\right), \tag{4-5}$$

where $\{\varepsilon_{\underline{n}}^{F-f}\}$ are the energy levels for the F-f uncoupled degrees of freedom. Most of the modes are treated as uncoupled harmonic oscillators, though in this calculation one of the modes is a hindered internal rotation for which the harmonic approximation is particularly poor, so the energy levels for that degree of freedom are obtained in a more careful fashion. The details of the energy level calculation are given in Section 4.2.5.

Equation 4-5 is a statement similar in nature to the "dimensionality reduced" approximations [24, 100], and for $f=1$ is the standard expression for one-dimensional tunneling corrections to microcanonical transition state theory. [25]

Section 4.2 first gives a more detailed description of the theoretical methodology and its implementation, and section 4.3 describes the results of the calculation for $f = 1$ and 2 coupled degrees of freedom. Section 4.4 concludes.

4.2. Summary of Theoretical and Computational Specifics

4.2.1. The Potential Energy Surface

Allen and Schaefer have carried out the most detailed calculations to date on the reaction ${}^3A\ CH_2CO \rightarrow {}^3B_1\ CH_2 + {}^1\Sigma^+\ CO$. [111, 112] At the TZ(2d1f,2p) CCSD level of theory, they find the transition state to be 4.74 kcal/mol above the products. The ^{3}A"

transition state is easily deformed via a hindered internal rotation to a ^{3}A' transition state that lies between the ^{3}A' ketene structure and the products. The barrier to the internal rotation is only 1.07 kcal/mol, resulting in energy levels for the internal rotation that lie within the range over which the experiments were carried out. For the purposes of this calculation, the internal rotation is treated as uncoupled from the reaction coordinate, although the energy levels must be calculated in order to obtain the RRKM rate. This is necessary because the harmonic approximation that is used for the other uncoupled modes will be incorrect for an internal rotation. The calculation of these energy levels is detailed in Section 4.2.5.

The points along the reaction path that have been calculated by Allen and Schaefer lead us to believe that a simple one or two degree-of-freedom calculation will capture the essential aspects of the reaction dynamics. The reaction coordinate is ideally chosen to be the distance between the centers of mass of the CH_2 and CO fragments (R in Figure 4-2). The *ab initio* calculations show two other degrees of freedom to be strongly coupled to this reaction coordinate. One of these (the CCO bending vibration, γ in Figure 4-2) transforms asymptotically into rotation of the CO product, while the other (the CH_2 scissors mode) retains it's identity as a vibration, although the CH_2 bend angle changes considerably from ^{3}A ketene to the $^3B_1$ methylene product. Although this mode may be strongly coupled to the reaction path, we treat it as uncoupled for the purposes of this calculation.

The functional form that we have used for the potential energy surface is:

$$V = V_{1d} + \frac{1}{2} a_{inert} \omega^2 (\gamma - \gamma_0)^2 + c_{R\gamma} (\gamma - \gamma_0)\ (R - R_{max}) , \tag{4-6}$$

where V_{1d} is defined as

$$V_{1d} = \frac{As}{(1-s)} - \frac{Bs}{(1-s)^2} + \left(\frac{\sigma}{R}\right)^{12} - V_0 , \tag{4-7}$$

with

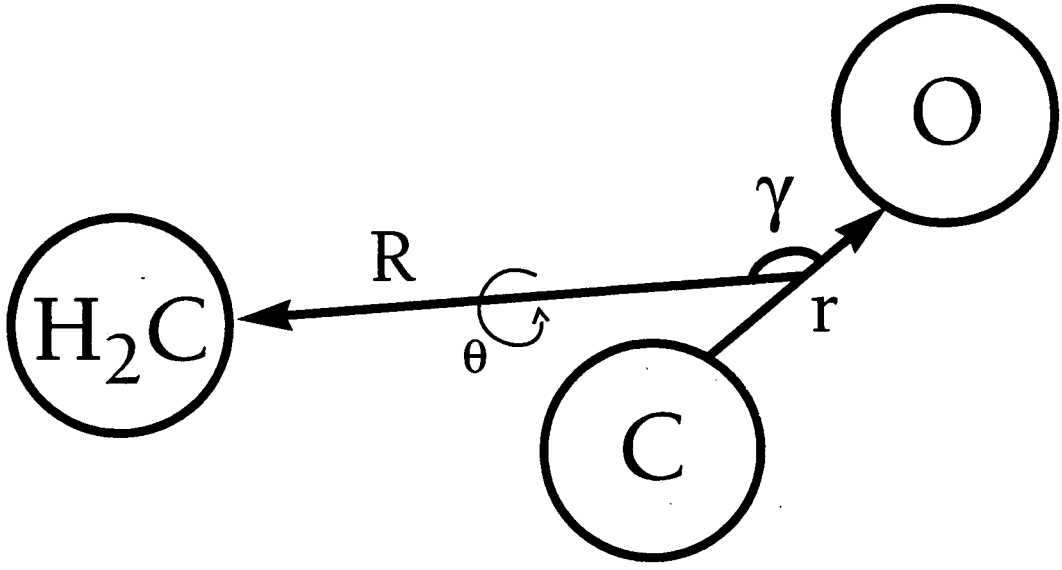

Figure 4-2. The coordinate system for ketene triplet dissociation.

The Jacobi coordinates used in this chapter. The coordinate r is the C-O vibrational coordinate, R is the distance of the center-of-mass of the CH_2 to the center-of-mass of the CO, and γ is the angle between these two distances. In this chapter, the CO bond distance r is fixed, and the calculation is carried out in the scattering coordinate R and the angle γ. The angle θ is utilized in the calculation of energy levels for the hindered internal rotation. θ is angle between the plane defined internally to the CH_2 unified atom and the plane defined by the two carbon and oxygen atoms.

$$s = -e^{2\pi(R-R_{barr})/l}, \tag{4-8}$$

and where ω is switched smoothly from the CCO bend frequency at ketene to 0 in the product region:

$$\omega = \omega_{ketene}\left(\frac{1}{1+e^{(R-R_{1/2})/\alpha}}\right). \tag{4-9}$$

The inertial term, a_{inert}, in equation 4-6 is given by

$$a_{inert} = \frac{1}{\mu_r r_0^2} + \frac{1}{\mu_R R^2}. \tag{4-10}$$

In equation 4-9, $R_{1/2}$ is chosen so that the frequency of the perpendicular vibrational mode is correct at both the ketene and transition state structures,

$$R_{1/2} = R_{max} - \alpha ln\left(\frac{\omega_{ketene} - \omega_{TS}}{\omega_{TS}}\right) \tag{4-11}$$

The frequencies, energies, and positions of the ketene minimum, the transition state, and the asymptotic product valley are given in Table 4-1. The parameters used to construct the best-fit potential energy surface are collected in Table 4-2.

		3A" CH_2CO	3A" $CH_2...CO$ transition state	$^3B_1CH_2 + {}^1\Sigma^+CO$
Energy (kcal/mol)	best fit surface	-26.76	0	-4.87
	Ref. [111][a]	-27.53	0	-4.74
CC Stretch ω (cm^{-1})	best fit surface	932	409 *i*	0
	Refs. [111] and [112][b]	931	379 *i*	0
CCO Bend ω (cm^{-1})	best fit surface	447	229	0
	Refs. [111] and [112][b]	463	228	0
R (bohr)	best fit surface	3.83	4.98	∞
	Ref. [111]	3.88	4.96	∞
γ (radians)	best fit surface	2.22	2.06	----
	Ref. [112]	2.20	2.06	----

Table 4-1. Energies and frequencies for the critical points along the reaction coordinate. Energies are relative to the transition state structure

a. calculated at the TZ(2d1f, 2p) CCSD level of theory.

b. 3A" CH_2CO frequencies were calculated at the DZP CISD level of theory.

parameter[a]	value
A	0.0896
B	0.1550
σ	2.77554
V_0	0.007758
R_{barr}	4.4938
l	-2.4696
μ_g	12506.1
γ_0	2.06188
$c_{R\gamma}$	0.27
R_{max}	4.97585
ω_{ketene}	2.0868×10^{-3}
ω_{TS}	1.0402×10^{-3}
α	0.3

Table 4-2. Parameters of the best-fit potential energy surface

a. All quantities are given in Atomic units (i.e. Distances are given in Bohr, Energies in Hartree, and angles in Radians, etc.)

4.2.2. The coordinate system

In performing this calculation, we used mass-scaled body-fixed center-of-mass Jacobi coordinates. The particular arrangement of the Jacobi coordinates we employed used the vector R between the CH_2 and the CO centers-of-mass as the scattering coordinate, and r as the CO vibrational coordinate. Figure 4-2 illustrates the details of the coordinate system that was used. The internal coordinates can be simplified to a set of 3 coordinates, $q = (R, r, \gamma)$, where R is the mass scaled scattering coordinate ($R = |R|$), r is the mass scaled CO vibrational coordinate ($r = |r|$), and γ is the bending angle ($\gamma = acos\,(r \cdot R/rR)$). The plane defined by the three "atoms" can be related to the lab frame coordinates via 3 Euler angles (Φ, Θ, Ψ) which rotate the body-fixed center of mass coordinates into the lab frame center of mass coordinates.

In the coordinate system outlined above, the six dimensional Hamiltonian is:

$$\hat{H}(\hat{\underset{\sim}{J}}, r, R, \gamma) = \hat{T}_r + \hat{T}_R + \frac{(\hat{\underset{\sim}{J}} - \hat{\underset{\sim}{j}})^2}{2\mu R^2} + \frac{\hat{\underset{\sim}{j}}^2}{2\mu r^2} + V(r, R, \gamma) , \tag{4-12}$$

where $\hat{\underset{\sim}{J}} - \hat{\underset{\sim}{j}}$ is the orbital angular momentum operator, $\hat{\underset{\sim}{j}}$ is the angular momentum operator for the CO, and the reduced mass, μ, is

$$\mu = \left(\frac{M_C M_O M_{CH_2}}{M_C + M_O + M_{CH_2}} \right)^{1/2} . \tag{4-13}$$

In equation 4-12, the kinetic energy operators are

$$\hat{T}_R = -\frac{\hbar}{2\mu} \frac{\partial^2}{\partial R^2}, \text{ and} \tag{4-14}$$

$$\hat{T}_r = -\frac{\hbar}{2\mu} \frac{\partial^2}{\partial r^2}, \tag{4-15}$$

and $V(r, R, \gamma)$ is the potential energy surface in the internal coordinates.

Since the internal degrees of freedom of the CH_2 moiety are treated as uncoupled from the scattering coordinate, the coordinate system is equivalent to the coordinates used in 3 atom reactive scattering calculations. In reduced-dimensionality scattering calculations, the two most commonly used coordinates are the scattering coordinate R, and the vibrational coordinate r. In the dissociation of triplet ketene, R is an obvious choice for the scattering coordinate, but γ is a natural choice for the second degree of freedom since deformations of the CCO bend angle appear to be highly coupled to the reaction coordinate and the CO bond length and vibrational frequency change little from ketene to the product CO molecule. We thus make the simplifying approximation that the CO bond distance is fixed at the transition state CO distance, r_0. Within this approximation, the Hamiltonian simplifies to:

$$\hat{H} = -\frac{\hbar^2}{2\mu}\frac{\partial^2}{\partial R^2} + \frac{(\hat{\underset{\sim}{J}} - \hat{\underset{\sim}{j}})^2}{2\mu R^2} + \frac{j^2}{2\mu r_0^2} + V(R, \gamma; r_0) \,. \tag{4-16}$$

The orbital angular momentum term can be expanded as

$$(\hat{\underset{\sim}{J}} - \hat{\underset{\sim}{j}})^2 = \hat{J}^2 + \hat{j}^2 - 2\hat{J}_x\hat{j}_x - 2\hat{J}_y\hat{j}_y - 2\hat{J}_z\hat{j}_z \,. \tag{4-17}$$

If we operate these terms on the simultaneous eigenstates of $\hat{J}^2$ and the projections of $\hat{J}$ along the z-axes of both the body-fixed and space-fixed frames, then the first term in this equation is $2\hbar^2 J(J+1)$. The final term in this equation is simply $2\hbar^2 K^2$, where K is the projection of the total angular momentum ($\hat{J}$) onto the z-axis of the body-fixed frame (which is along R). The third and fourth terms in equation 4-17 are off-diagonal in K and are usually called the Coriolis coupling terms. When the off-diagonal terms in K are small, these terms can be neglected, and the approximate Hamiltonian (or the "centrifugal sudden" approximation) is given by:

$$\hat{H} = -\frac{\hbar^2}{2\mu}\frac{\partial^2}{\partial R^2} + \frac{\hbar^2\,[J(J+1) - 2K^2]}{2\mu R^2} + \hat{j}^2\left(\frac{1}{2\mu R^2} + \frac{1}{2\mu r_0^2}\right) + V(R, \gamma; r_0) \,. \tag{4-18}$$

4.2.3. The Basis Set

In performing this calculation, we have used two different Discrete Variable Representations (DVRs) for the two coupled degrees of freedom. Along the scattering coordinate, R, we use the radial form of the sinc-function DVR introduced by Colbert and Miller. [32] In this basis set, the functions are associated with points along a grid defined by $R_i = i\Delta R$, where ΔR is determined by the highest kinetic energy we wish to represent,

$$\Delta R = \frac{2\pi}{N_B\sqrt{(2\mu\,(E - V_{low}))/\hbar^2}} \,. \tag{4-19}$$

In this equation, N_B is the number of grid points per deBroglie wavelength (typically between 3.7 and 4), and V_{low} is the lowest point on the potential energy surface. In the

radial sinc-DVR basis set, the kinetic energy for the scattering coordinate (the first term in equation 4-18) is given by

$$T_{ii'} = \frac{\hbar^2}{2\mu\Delta R^2}(-1)^{i-i'}\left\{\begin{array}{ll} \frac{\pi^2}{3} - \frac{1}{2i^2} & i = i' \\ \frac{2}{(i-i')^2} - \frac{2}{(i+i')^2} & i \neq i' \end{array}\right\}. \tag{4-20}$$

In the bending degree of freedom, we are using a Gauss-Legendre DVR to construct a set of points $\{cos\gamma_i\}$ and weights $\{\omega_i\}$ for the $K=0$ associated Legendre functions. These points and weights are then used to construct a representation of the angular momentum in the third term in equation 4-18 as follows:

$$\hat{j}^2_{ii'}(K) = \sum_{j=K}^{2N_{GL}-1} \sqrt{w_{i'}} P_{jK}(cos\gamma_{i'})\,[\hbar^2 j(j+1)]\,P_{jK}(cos\gamma_i)\sqrt{w_i}, \tag{4-21}$$

where the P_{jK}'s are the associated Legendre functions ($P_{jK}(cos\gamma) = \sqrt{2\pi}Y_{jK}(\gamma, 0)$, and $Y_{lm}(\theta, \phi)$ is a spherical harmonic function). N_{GL} is the number of Gauss-Legendre DVR points, which is obtained by dividing the range of γ (0 to π) by the angular spacing required to represent the highest kinetic energy. This spacing is calculated in a similar fashion to the radial spacing in equation 4-19.

4.2.4. Evaluation of the Trace

Manthe and Miller [37] have shown that an efficient way to evaluate the trace in Eq. 4-3 is to introduce the reaction probability operator $\hat{P}(E)$, defined by

$$\hat{P}(E,J) = 4\hat{\epsilon}_r^{1/2}\hat{G}_J(E)^*\,\hat{\epsilon}_p\hat{G}_J(E)\,\hat{\epsilon}_r^{1/2}, \tag{4-22}$$

so that Eq. 4-3 for $N(E)$ becomes

$$N(E,J) = tr[\hat{P}(E,J)]. \tag{4-23}$$

(Since the absorbing potential matrices are diagonal, the square roots in Eq. 4-22 cause no problems.) We have dealt with the calculation of the trace of $\hat{P}$ (Eq. 4-23) in greater detail in Chapter 3. It is helpful to review the basic implementation of the method here, however. The trace is evaluated using the Lanczos algorithm; [39, 38, 40] i.e., one begins with some starting vector $\underset{\sim}{v}_1$, and a sequence of Krylov vectors is generated by

$$\underset{\sim}{v}_{n+1} = \underset{\sim}{P} \cdot \hat{v}_n + S.O. \tag{4-24}$$

where $S.O.$ denotes Schmidt orthogonalization to all preceding vectors. The matrix elements of $\underset{\sim}{P}$ in this basis,

$$P_{n,n'} = \underset{\sim}{v}_n \cdot \underset{\sim}{P} \cdot \underset{\sim}{v}_{n'} \tag{4-25}$$

are obtained in the process of generating the vectors, and the trace carried out in this representation,

$$N(E,J) = \sum_n P_{n,n}. \tag{4-26}$$

This procedure is efficient because the rank of the matrix $\underset{\sim}{P}$ is low, typically orders of magnitude lower than the size of the DVR basis itself, and the number of Lanczos iterations required – i.e., the number of Krylov vectors which must be generated via Eq. 4-24 – is essentially the rank of $\underset{\sim}{P}$.

We explicitly re-orthogonalize the Lanczos vectors to avoid compounding numerical errors and iterate until $N(E)$ is converged to 10^{-3}. For the highest energies reported this required 5-10 iterations, and for the lowest energies only about 3.

Every operation of the matrix $\underset{\sim}{P}$ onto a vector in Eq. 4-24 requires two operations of the Green's function matrix onto a vector (i.e., the various matrices in $\hat{P} = 4\hat{\epsilon}_r^{1/2}\hat{G}(E)^* \hat{\epsilon}_p \hat{G}(E)\hat{\epsilon}_r^{1/2}$ multiply sequentially from the right). The operation of the Greens function matrix onto a vector effectively means that one must solve the set of linear equations,

$$\underset{\sim}{A} \cdot \underset{\sim}{x} = \underset{\sim}{b}, \tag{4-27}$$

where the vector $\underset{\sim}{b}$ is given and $\underset{\sim}{A} = (E + i\underset{\sim}{\epsilon} - \underset{\sim}{H})$, and this is the primary computational task. Use of the Lanczos method above with the P-operator/matrix greatly reduces the number of Green's function operations that are required and is why it was such an important step forward.

We have made use of the quasi-minimum residual (QMR) algorithm [36] to solve Eq. 4-27 for $\underset{\sim}{x} = \underset{\sim}{A}^{-1} \cdot \underset{\sim}{b}$. QMR finds the inverse by a quasi-minimization of the residual at each iteration, and is based on the look-ahead Lanczos algorithm which is used to find approximate eigenvalues of large non-Hermitian matrices. We have also used a diagonal pre-conditioner to reduce the number of required applications of $\underset{\sim}{A} = (E + i\underset{\sim}{\epsilon} - \underset{\sim}{H})$ required to obtain the inverse. The detailed workings and the effective use of QMR in reactive scattering calculations has been investigated in great detail by Karlsson, [109] and the reader is encouraged to see this work for more specifics of how the QMR algorithm is applied to this type of calculation.

In this set of calculations, we have stopped the QMR iterations when the residual for the Green's function has dropped below 10^{-4}. This typically required N applications of the matrix, where N is on the order of 10%-20% of the number of basis functions.

4.2.5. Hindered Internal Rotation

Following the work of Kim, Lovejoy, and Moore, [10] we have treated the hindered internal rotation as uncoupled from the reaction coordinate, R, and the CCO bend, γ. The hindered rotor cannot be treated as a simple harmonic oscillator in the reduced-dimensionality approximation (eqn. 4-5) because the barrier to internal rotation is at approximately the same energy as the energies at which the experiment is carried out. The situation is complicated even more by the high degree of coupling between the internal rotation and the overall rotation of the ketene about the same axis. Given the information about the transition states that is known from *ab initio* calculations, we can

approximate the potential energy surface for the hindered rotation as a cosine series: [10]

$$V(\theta) = \frac{V_0}{2}(1 - cos2\theta) + \frac{V_1}{2}(1 - cos4\theta) + \ldots . \tag{4-28}$$

In equation 4-28, θ is the dihedral angle between the CH_2 and CCO planes, V_0 is the barrier to internal rotation, and V_1 changes the width of the barrier. There is one minor difference between our treatment of the internal rotation and the treatment in Ref. [10]; we utilize the Jacobi R coordinate as the axis of the reference frame for the internal rotor, while Kim *et al.* used the CC bond as the axis for this rotation.

In order to calculate the coupling between the hindered internal rotation and the overall rotation of the ketene molecule, we use *ab initio* calculations of the structure of the C_s^{II} transition state to obtain the moments of inertia for the ketene itself. The moment of inertia of the CH_2 top about the Jacobi axis is denoted I_{top}, and the moment of inertia of the CO frame about the same axis is denoted I_{frame}. Since $I_{top} > I_{frame}$, we use the principal axes of the ketene molecule at the transition state as the coordinate system. Following Brocks, *et al.* [115] and Stockman, *et al.*, [116] the Hamiltonian is written as:

$$H = H_{rot} + F(p - P)^2 + V(\theta) , \tag{4-29}$$

where H_{rot} is the rigid-rotor asymmetric top rotational Hamiltonian, and F is the effective rotational constant for the internal rotation of the top about its symmetry axis:

$$F = \frac{\hbar^2}{2rI_{top}} ; r = 1 - \sum_i \frac{\lambda_i I_{top}}{I_i} , i = (a, b, c) . \tag{4-30}$$

In equation 4-30, I_a, I_b, and I_c are the principal moments of inertia of the ketene molecule, λ_a, λ_b, and λ_c are the direction cosines of the symmetry axis of the top to the principal axes, and I_{top} is the moment of inertia of the CH_2 about the symmetry axis.

If $T = (H\text{-}V)$, then momenta P and p in equation 4-29 are defined as

$$P = \sum_i P_i \hat{i}\,;\; P_i = \frac{\partial T}{\partial \omega_i}, \text{ where } i = (a, b, c)\text{, and } p = \frac{\partial T}{\partial \dot{\theta}}. \tag{4-31}$$

In the expression for P_i, ω_i is the angular velocity about axis i. We can now make 2 simplifying assumptions. First, since there is a plane of symmetry, λ_c from equation 4-30 vanishes. Second, since $(p\text{-}P)$ in equation 4-29 represents the relative angular momentum of the top and the frame, we can rewrite the Hamiltonian as:

$$\begin{aligned} H = {} & A^{\ddagger\prime} P_a^2 + B^{\ddagger\prime} P_b^2 + C^{\ddagger} P_c^2 - 2F\,(\alpha P_a p + \beta P_b p) \quad , \\ & + F\alpha\beta\,(P_a P_b + P_b P_a) + F p^2 + V(\theta) \end{aligned} \tag{4-32}$$

where

$$A^{\ddagger\prime} = A^{\ddagger} + F\alpha^2,\; B^{\ddagger\prime} = B^{\ddagger} + F\beta^2,\; \alpha = \frac{\lambda_a I_{top}}{I_a},\; \beta = \frac{\lambda_b I_{top}}{I_b}, \tag{4-33}$$

and $\ddagger$ denotes the transition state geometry.

The Hamiltonian matrix can then be easily set up in a symmetric prolate top free-rotor basis. The non-vanishing elements of H are given in Stockman *et al.* [116] For the ketene transition state, which is a nearly symmetric top, the matrix elements off-diagonal in $K^{\ddagger}$ are very small, so they are neglected in this calculation. In the free-rotor basis set, $|m\rangle = \frac{1}{\sqrt{2\pi}} e^{-im\theta}$, the Hamiltonian matrix is then:

$$\langle m|H|m\rangle = Fm^2 - 2F\alpha K^{\ddagger} m + \frac{V_0}{2} + \frac{V_1}{2}, \tag{4-34}$$

$$\langle m|H|m \pm 2\rangle = -\frac{V_0}{4}, \text{ and} \tag{4-35}$$

$$\langle m|H|m \pm 4\rangle = -\frac{V_1}{4}. \tag{4-36}$$

The parameters used for the calculation of the hindered rotor energy levels are given in Table 4-3. A basis set of 100 free-rotor functions was used to construct the Hamiltonian matrix, which was then diagonalized to give the energy levels of the hindered internal rotation for each value of K. These energy levels (which differ slightly from those calculated in Ref. [10] due primarily to the height of the *ab initio* barrier) were then used in the RRKM expression for the dissociation rate.

parameter[a]	value
I_a	5.65
I_b	69.55
I_c	75.21
λ_a	0.91
λ_b	0.42
F	12.64
I_{top}	2.004
$A^{\ddagger}$	4.297
$B^{\ddagger}$	0.244
$C^{\ddagger}$	0.224
V_0	374.2
V_1	-30.0

Table 4-3. Parameters used in the calculation of hindered internal rotation energy levels of the transition state.

a. The units are amu *Å^2 for I_x (x=a,b,c,top) and cm^{-1} for F, $A^{\ddagger}$, $B^{\ddagger}$, $C^{\ddagger}$, V_0, and V_1. The *ab initio* (TZ(2d1f, 2p) CCSD) C_s^{II} transition state structure in Ref. 111 was used to obtain these values.

4.3. Results

The dissociation rate has been calculated with one and two quantum degrees-of-freedom in the scattering calculation. Thermal populations of the overall angular momentum (J) of ketene at a rotational temperature of 4 K were generated. At each energy, all allowed K states for a given J were used to construct the Hamiltonian in the centrifugal sudden approximation (eqn. 4-18). This Hamiltonian was used in the calculation of

$N_{JK}(E)$, which was then used in the RRKM expression for the dissociation rate. The results of these calculations are presented below.

4.3.1. One degree of freedom

The cumulative reaction probability, $N(E)$, for the one degree of freedom calculation is plotted in figure 4-3. The most notable thing about $N(E)$ is that it rises slowly over the span of several hundred cm^{-1} in energy. This range of energy is directly related to barrier frequency, which in the best *ab initio* calculations is 379 i cm^{-1}. A lower barrier frequency would make the rise in the reaction probability much sharper, because at energies below the barrier, tunnelling through a wider barrier would be more difficult thereby reducing the reaction probability at those energies.

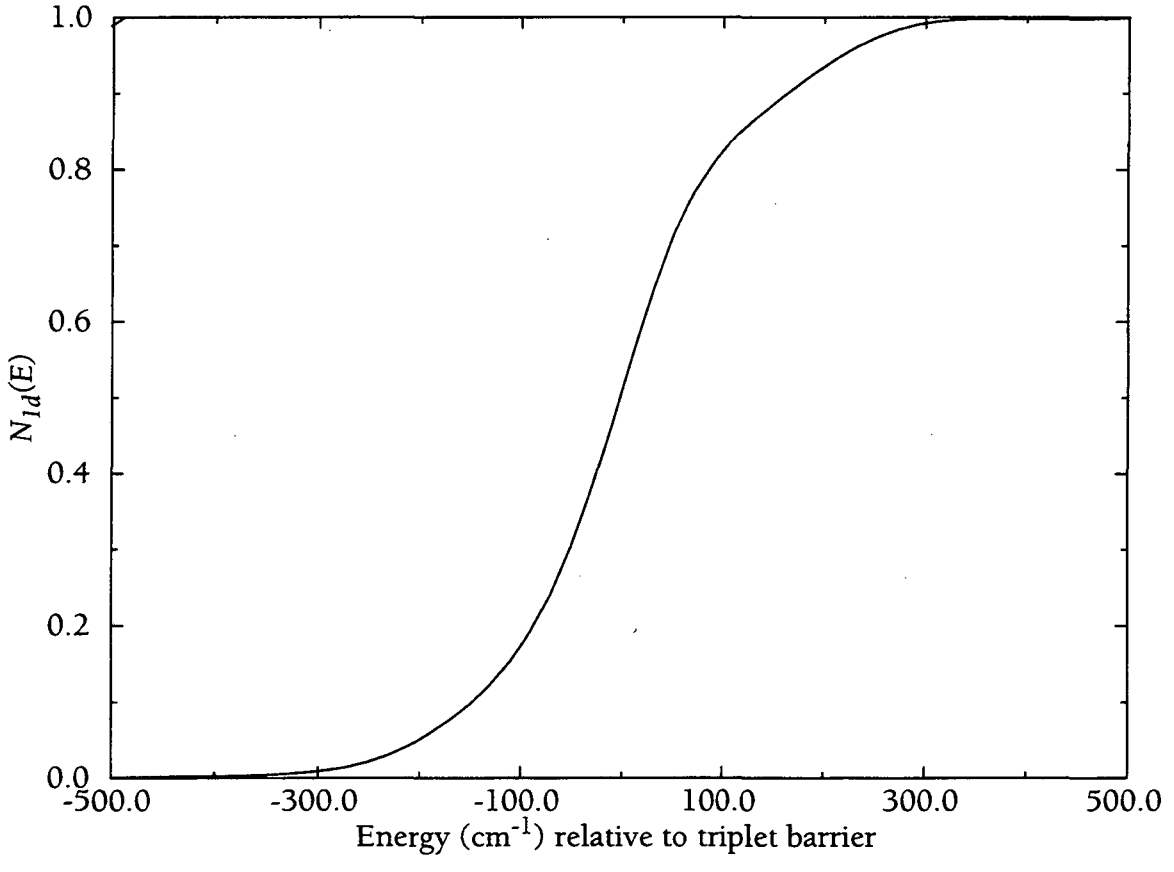

Figure 4-3. $N_{1d}(E)$ for ketene triplet dissociation

The cumulative reaction probability ($N_{1d}(E)$) for the calculation with one active degree of freedom.

This reaction probability has been used in an RRKM calculation (with *ab initio* vibrational frequencies given in Table 4-4) to obtain the dissociation rate as a function of

mode	frequency (cm^{-1})[a]
ν_1 (a') asym CH stretch	3343.9
ν_2 (a') sym CH stretch	3135.0
ν_3 (a') CO stretch	2141.4
ν_4 (a') CH_2 scissor	1166.6
ν_5 (a') CH_2 rock	421.4
ν_6 (a') CC stretch	379.0 *i*
ν_7 (a') CCO bend	228.3
ν_8 (a") CH_2 wag	331.6
ν_9 (a") HCCO torsion	134.4

Table 4-4. The *ab initio* Vibrational frequencies of the C_s^{II} transition state

a. Frequencies are taken from Ref. 111 and were calculated at the TZ (2d1f, 2p) CCSD level of theory.

energy. This is plotted along with the experimentally measured dissociation rates in figure 4-4. There is good agreement in general with the experimental results and our calculation, although any step-like features due to quantization of states of the activated complex have been "washed out" by the slow rise of $N_{1d}(E)$. This is due to the frequencies of some of the perpendicular vibrations (CCO bend, CH_2 wag, CH_2 rock, and HCCO torsion) being considerably lower than the barrier frequency. This causes the spacings between the would-be steps to be smaller than the width over which the step rises, so that they overlap one another, leading to a very smooth reaction probability in RRKM calculations.

In order to estimate what barrier frequency would be needed to closely match with the experimental rates, we have also calculated the rates using an asymmetric Eckart barrier with a number of different barrier frequencies as the potential energy along *R*. The reaction probability for this barrier is analytical and well-known. [117] These calculated rates are shown in figure 4-5. It is interesting to note that we do not observe step-like

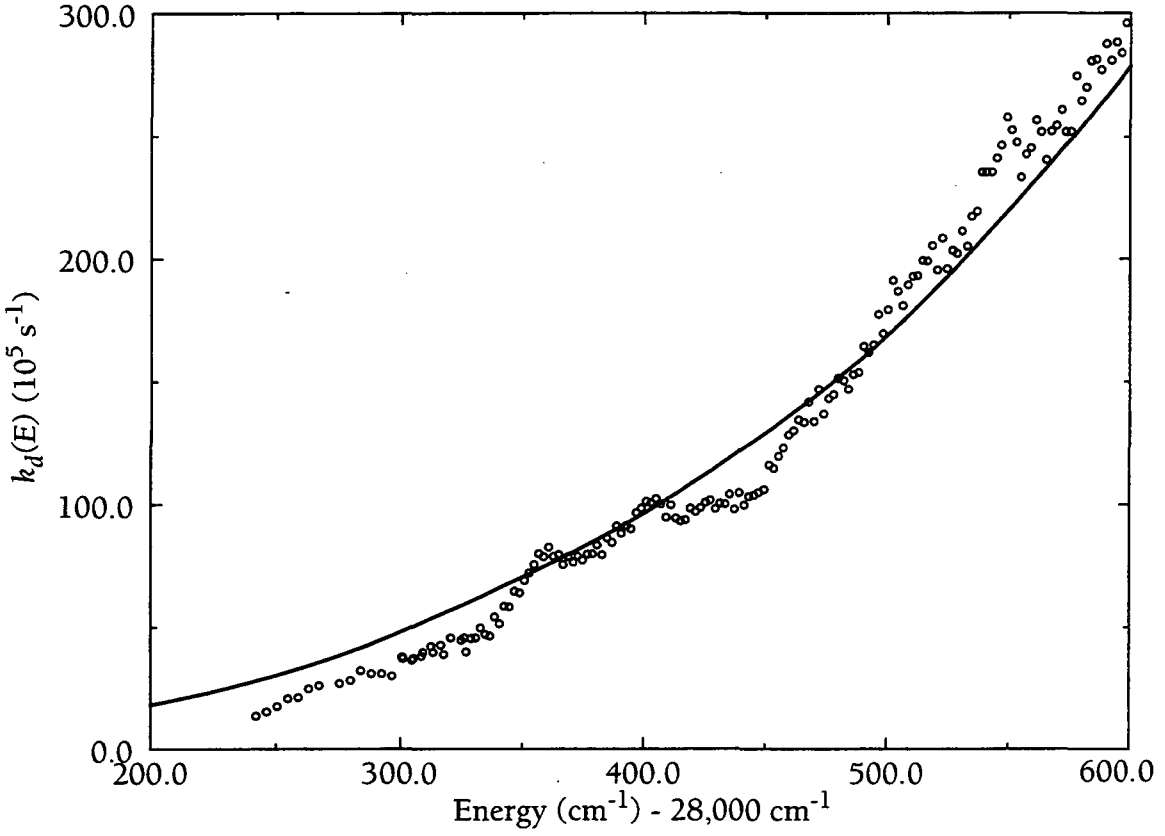

Figure 4-4. The one-dimensional $k_d(E)$ for ketene triplet dissociation

The calculated dissociation rate ($k_d(E)$) with one active degree of freedom compared to the experimental results from Ref. [10].

features in the calculated rates until the barrier frequency has dropped below 100 cm^{-1}, *4 times* lower than the barrier frequency predicted by *ab initio* calculations. With barriers that low, we do not obtain good agreement with experiments over the whole energy range, although the agreement at lower energies suggests that the barrier frequency may be substantially lower than *ab initio* calculations predict it to be.

Additionally, the step-like features seen with barrier frequencies of 100 and 50 cm^{-1} have approximately the correct energy spacings for states of the hindered internal rotation. The spacing of the steps in the experimental rates leads us to believe that the barrier to the internal rotation as well of the frequency for that vibrational mode at the transition state are probably too high in the *ab initio* calculations.

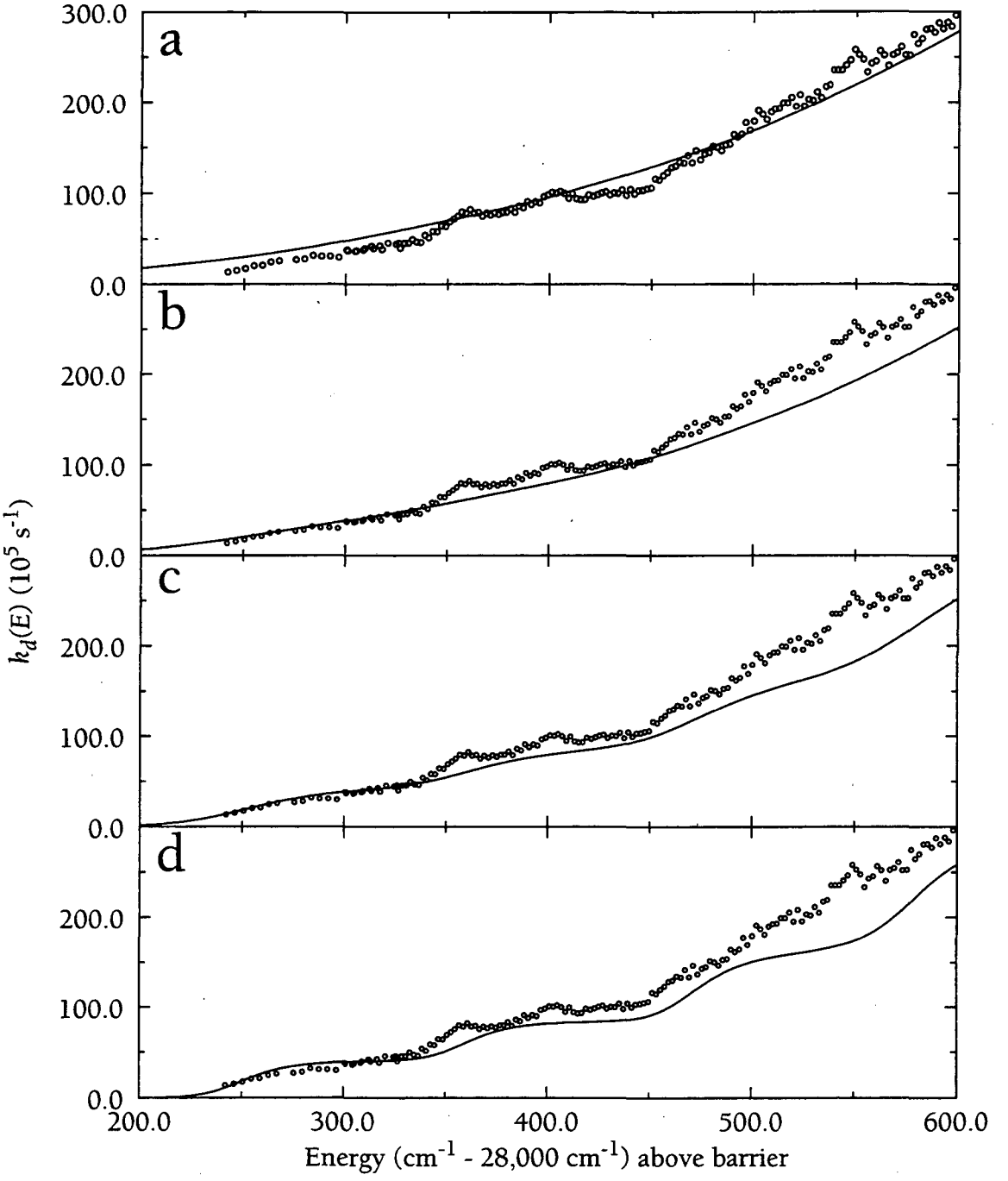

Figure 4-5. The effect of lowering the barrier frequency.

Plots showing one degree of freedom calculations of the dissociation rate ($k_d(E)$) for a number of different barrier frequencies, compared to the experimental results from Ref. [10]. (a), (b), (c), and (d) are for barrier frequencies of 397 i cm^{-1} (as calculated in Ref. [111]), 200 i cm^{-1}, 100 i cm^{-1}, and 50 i cm^{-1}, respectively.

4.3.2. Two degrees of freedom

We have also investigated whether the step-like features in the experimental rates could be caused by coupling between one of the perpendicular vibrations and the reaction coordinate. If the potential energy surface "tightened" just before or after the transition state, it is possible that structure could arise in the CRP due to short-lived metastable states. Most of the highly-coupled modes loosen as the reaction coordinate goes toward the product region and become tighter toward the ketene reactant well. We picked the most highly-coupled mode (the CCO bend) for our investigation of this effect. The potential energy surface we are using (see equations 4-6 through 4-11) does tighten the perpendicular vibrational frequency considerably towards the reactant region. A contour plot of the 2-dimensional surface is shown in figure 4-6.

The calculated rate using two quantum degrees-of-freedom is shown with the experimental rate in figure 4-7. The most noticeable feature of the energy dependence of this reaction rate is that while giving good overall agreement with the experimental rates, it does not exhibit the step-like features observed experimentally.

4.4. Discussion

The present calculations thus show good overall agreement with the experimentally observed rates, but the step-like features observed experimentally are still unexplainable using the best currently available potential energy surface.

It is possible that the potential energy surface we have been using does not accurately capture the essential features of the reaction. The frequencies and energies along the reaction coordinate are known at a very small number of points -- ketene, the transition state, and the asymptotic products. A second transition state farther out into the product region, or a tightening of the perpendicular modes after the known transition state to form a dynamical bottleneck could result in some of the structures observed by Kim *et al.* It may be, too, that the ab initio calculations are simply not quantitatively accurate for this system and that the barrier frequency may be significantly lower than the present value.

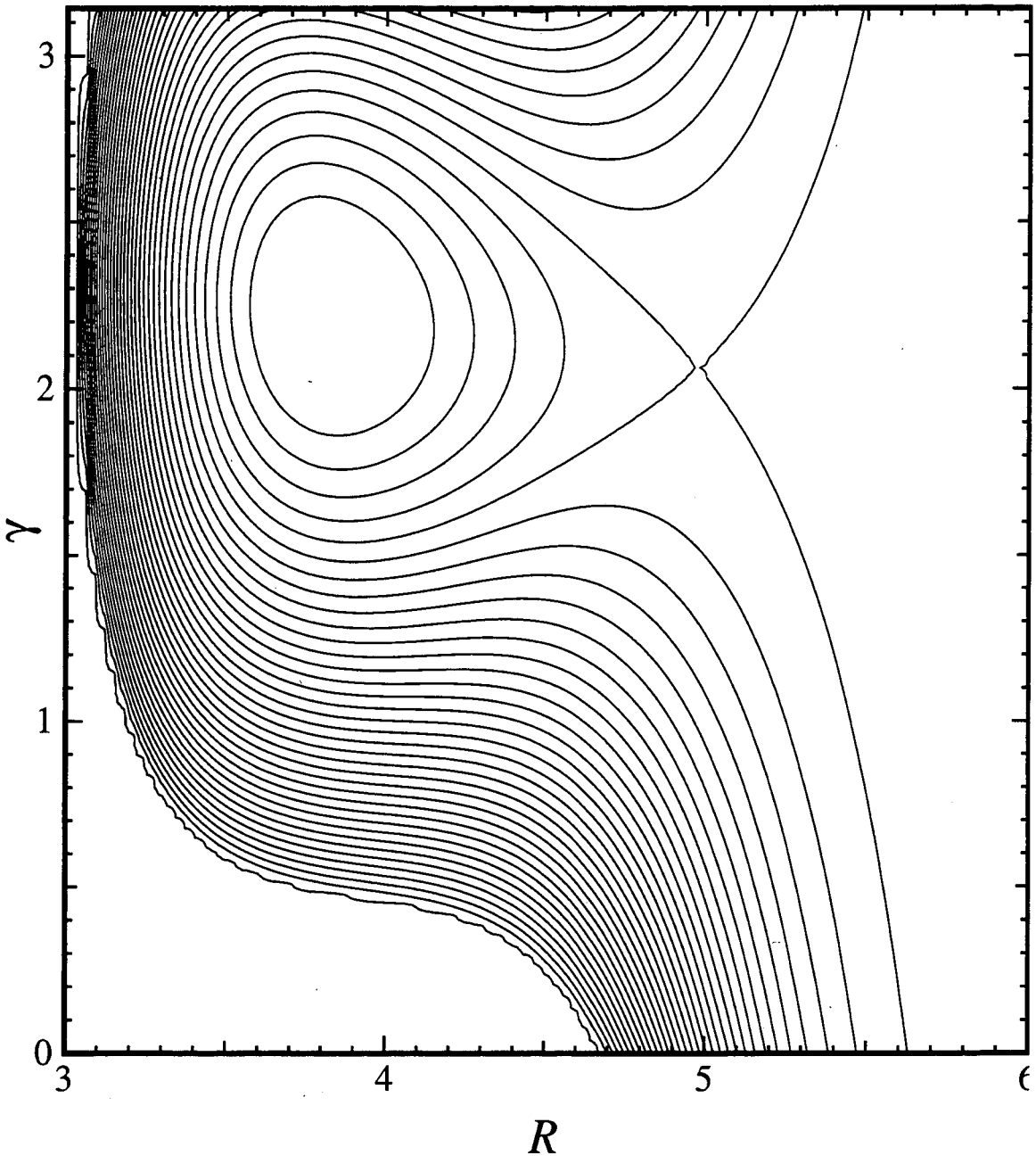

Figure 4-6. The 2-D surface for ketene triplet dissociation

Contour plot showing the best-fit 2-d potential energy surface used in the calculation of the 2-d dissociation rate in Fig 4-7.

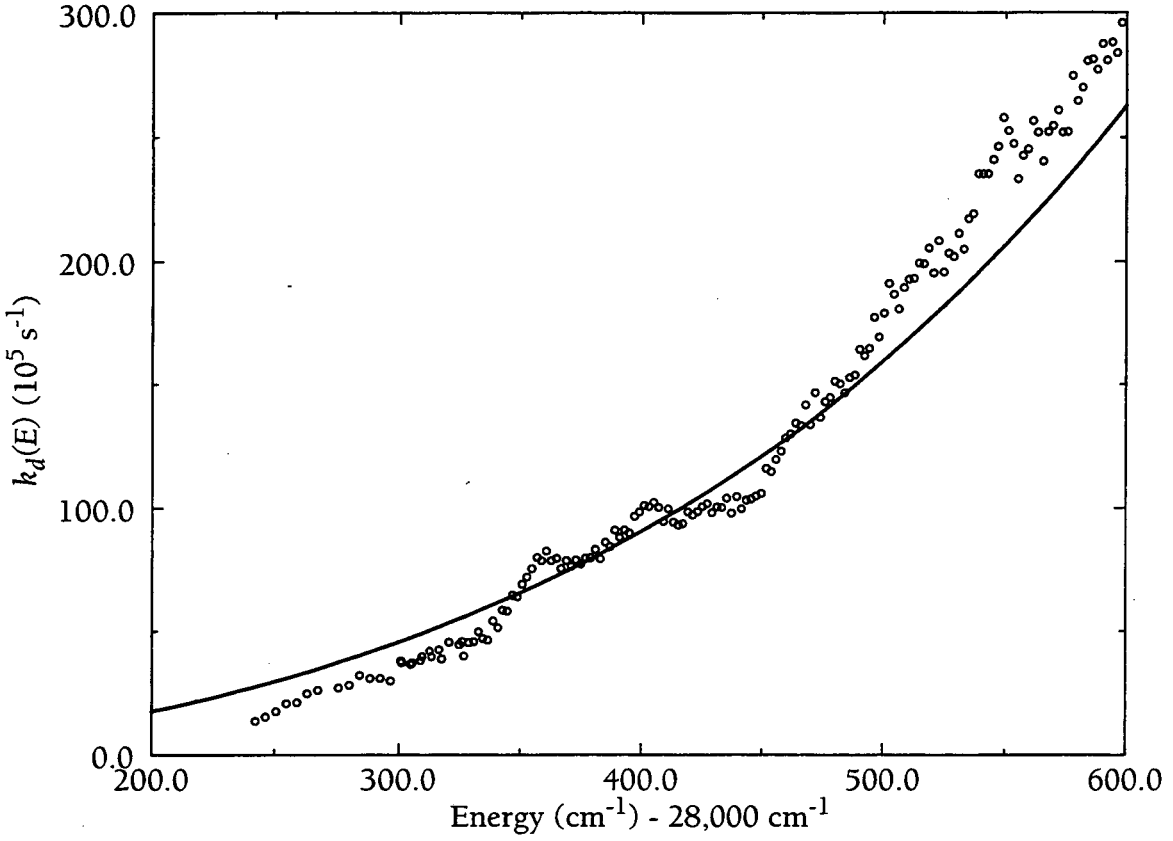

Figure 4-7. The two-dimensional $k_d(E)$ for ketene triplet dissociation

The calculated dissociation rate ($k_d(E)$) with two active degrees of freedom compared to the experimental results from Ref. [10]

Alternatively, Troe and Moore have proposed [118] that the crossing between the singlet and triplet surfaces may occur at a geometry very near the transition state configuration (although with a substantially different CH_2 bending angle). Surface hopping between the triplet and singlet surfaces in the vicinity of the transition state could also give some amount of structure to the rates or effectively broaden the barrier along the reaction coordinate.

Which scenario is a most likely explanation for the observed features awaits a more comprehensive exploration of the both the triplet and singlet potential energy surfaces by *ab initio* methods.

5 The Barrier Impulsive Model: A new method for predicting the distribution of energy in photodissociation reactions

Abstract

A new model for calculating the average energies in product rotational, vibrational, and translational degrees of freedom in photodissociation reactions involving substantial exit barriers is presented. The model is discussed as a logical extension of the impulsive model that includes statistical partitioning of energy in excess of the barrier. Calculations are performed using the new model on the photodissociation of acetone and acetic acid. The results are compared to experiments and to other models for unimolecular dissociation.

5.1. Introduction

In seeking to explain the results of a wide range of photodissociation experiments, it is desirable to have a model that accurately reflects the physics of the dissociating molecule. Many models have been used because they explain the reactions in terms of simple impulsive bond rupture. [41, 42] These models are justifiably popular because they give an easily understood physical picture of the reaction.

Another class of models seeks to explain the experiments in terms of a statistical distribution of energy either in the products or at the transition state. For experiments which involve large barriers to recombination, however, these models fail to reproduce the interesting physics of the dissociation event. It seems then, that neither set of models

has satisfactory predictive (or even explanatory) power for many possible photodissociation events.

We seek a model that will reflect both the impulsive nature of reactions with large barriers to recombination as well as the statistical distribution of energy in excess of the barrier height. We also want to restrict our model so that it requires only readily available information about the transition state and the reactants. Commonly known quantities are the normal mode frequencies of the reactant and product molecules, geometries of the transition state, and the forward and reverse barrier heights. We believe that the model presented in this chapter represents a simple extension of the impulsive and statistical models that are currently in common use. We hope that the physical picture that we present will allow a physical understanding of the unimolecular reaction that gives qualitative agreement with experiments.

The barrier impulsive model (BIM) is conceptually very simple. The available energy is separated into two "energy reservoirs", one which is denoted *statistical* and the other *impulsive*,

$$E_{avail}(tot) = E^{stat}(tot) + E^{imp}(tot) \tag{5-1}$$

$E^{imp}(tot)$ is chosen to be the height of the exit barrier (Figure 5-1). In this way the model reduces to the impulsive model at the dissociation threshold and to a simplified statistical model in the absence of a barrier. Furthermore, since the translational energy of the products from the impulsive reservoir is fixed by the barrier height, the total translational energy increases with available energy statistically. This behavior is consistent with experimental observation. (for examples, see Refs. 122, 123, 124, 125, and 126) The partitioning of energy into product rotation, vibration, and translation in each reservoir independently conserves linear momentum, angular momentum, and total energy. The impulsive reservoir can be partitioned among the fragment degrees of freedom according to either the soft or the rigid fragment models. The energy in the statistical reservoir is partitioned by a new method that is outlined in Section 5.3. The average

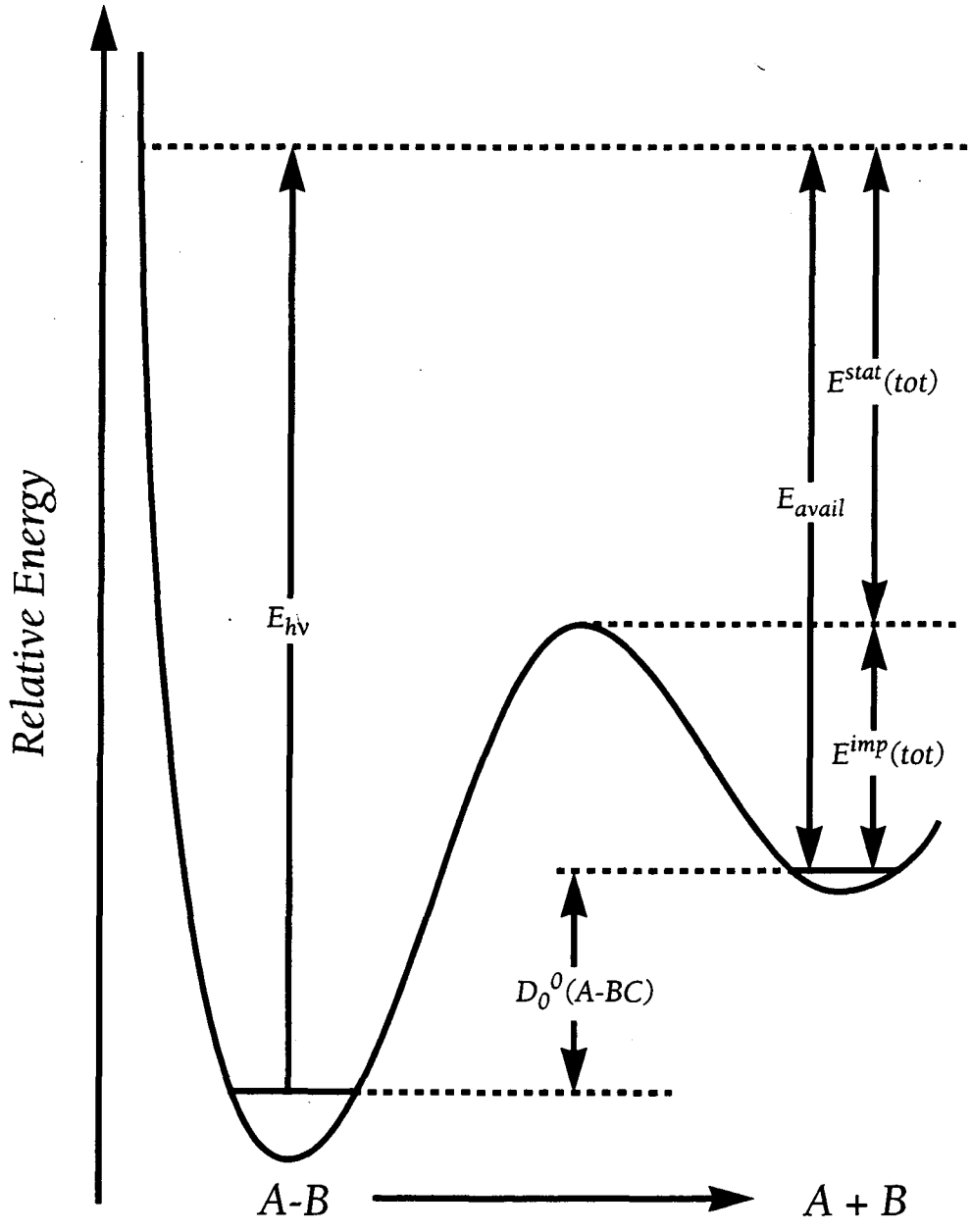

Figure 5-1. Sketch showing the energetic reservoirs.

Schematic energy diagram showing the relations between various energetic quantities in the barrier impulsive model.

energies from each reservoir are combined to obtain the final R,V, and T energies of the products. There are a number of inherent assumptions in this model. We assume that once the molecule is beyond the transition state the *localized* release of the potential energy from the exit barrier can be adequately described by the impulsive model. In

order for the statistical treatment of $E^{stat}(tot)$ to be justified, the redistribution of vibrational energy must occur prior to dissociation but cease at the moment of the impulsive energy release.

We now consider the photodissociation of a polyatomic molecule A-B. The initial bond cleavage, produces fragments A and B which can themselves be polyatomic. We assume that neither fragment is electronically excited upon dissociation and that the A-B parent contains no internal energy prior to absorption of the photon.

5.2. The Impulsive Model

If there is a large release of the available energy into product translation then a model in which the potential energy is released locally, between the departing fragments is required. The most commonly used of these due to its simplicity is the impulsive model, first applied to triatomic photodissociation by Busch and Wilson. [41] An extension of the model that treats polyatomics has been presented by Tuck. [42] In the Impulsive model it is assumed that when the bond is broken *all* of the potential energy is released in the dissociative coordinate as repulsion between the two previously bonded atoms. The two atoms then transfer their initial kinetic energy into translation, rotation and vibration of the fragments in accordance with classical kinematics. The impulsive model has been successful in predicting the partitioning of available energy into product translation in the dissociation of many polyatomic molecules. Most notable are the alkyl halides.[127] These molecules exhibit strong anisotropy in the photofragment angular distributions indicating that the dissociation occurs prior to parent rotation. This suggests that the dissociation is sudden, with excitation directly to a repulsive electronic state. In the alkyl halides, the transition involves promoting an electron localized on the halogen to a C-X anti-bonding orbital. The inherent assumptions in the impulsive model are justified here because the dissociation resembles a *quasi-diatomic* due to the localized absorption of the photon. [128]

The available energy (in the A-B center-of-mass) which will ultimately be partitioned between the various degrees of freedom of the photofragments is given by,

$$E_{avail} = E_{h\nu} + E_{int}(AB) - D_0^0(AB) \tag{5-2}$$

where $E_{h\nu}$ is the photon energy, $E_{int}(AB)$ is the internal energy of the parent, and $D_0(AB)$ is the bond dissociation energy. The contribution of $E_{int}(AB)$ to the available energy is neglected, which is a reasonable assumption in the context of a molecular beam experiment. The basic premise of the impulsive model is that all of the available energy is released as a repulsion localized in the reaction coordinate. There are two limiting impulsive models: the "soft" fragment limit and the "rigid" fragment limit.

5.2.1. The Soft Fragment Limit

In the soft fragment impulsive model (SFIM) the two previously bonded atoms, α (on fragment A) and β (on fragment B) are considered to be loosely coupled to their respective fragments which behave as spectators during the dissociation. The atoms recoil with relative translational energy according to the conservation of linear momentum,

$$E_T(\alpha) = \frac{m_\beta}{M} E_{avail} = E(A) \tag{5-3}$$

$$E_T(\beta) = \frac{m_\alpha}{M} E_{avail} = E(B) \tag{5-4}$$

where m_α, m_β, and M are the mass of atom α, the mass of atom β, and the total mass (m_α+m_β) respectively. This kinetic energy also determines the total energy, $E(A)$ and $E(B)$, each atom transfers to its respective fragment A and B. The translational energy of each fragment is obtained from the conservation of momentum,

$$E_T(A) = \left(\frac{m_\alpha}{m_A}\right) E(A) \tag{5-5}$$

$$E_T(B) = \left(\frac{m_\beta}{m_B}\right) E(B) \tag{5-6}$$

where m_A and m_B are the masses of the fragments. When one of the fragments is an atom, for example A=α, then the expected result $E(A)=E_T(A)$ is obtained. Rearranging equations 5-5 and 5-6 the total translational energy, $E_T(tot)$, released in the dissociation can be obtained,

$$E_T(tot) = \left(\frac{\mu_{\alpha\beta}}{\mu_{AB}}\right)E_{avail} \tag{5-7}$$

where $\mu_{\alpha\beta}$ is the reduced mass of atoms α and β and μ_{AB} is the reduced mass of the two fragments. The fact that, in a two-body dissociation, the total translational energy is determined only by a mass factor ($\mu_{\alpha\beta}/\mu_{AB}$) and the available energy is the well known result of the soft fragment impulsive model. It is important to note that the translational energy is independent of the geometry of the molecule.

The internal energy of each fragment is simply the difference between its total energy and its translational energy,

$$E_{int}(A) = \left(1 - \frac{m_\alpha}{m_A}\right)E(A) \tag{5-8}$$

$$E_{int}(B) = \left(1 - \frac{m_\beta}{m_B}\right)E(B) \tag{5-9}$$

If A is an atom and B is a diatomic then the partitioning of internal energy between fragment rotation and vibration can be found in reference 41. Even if they are not, the polyatomic parent can often be approximated as a pseudo-diatomic. However, this treatment assumes that the geometry of the fragment at the time of the impulse is identical to the asymptotic geometry. If this is not the case then the model will incorrectly predict the rotational energy despite conserving angular momentum.

A general method for determining the partitioning of internal energy involves first obtaining the rotational energy from the conservation of angular momentum. The

fragment vibrational energy is then later determined from the conservation of energy. The angular momentum associated with each atom as it recoils about its respective fragment's center-of-mass is given by,

$$J_\alpha = b_\alpha \sqrt{2m_\alpha E_T(\alpha)} \tag{5-10}$$

$$J_\beta = b_\beta \sqrt{2m_\beta E_T(\beta)} \tag{5-11}$$

where b_α and b_β are the classical exit impact parameters (see Figure 5-2). Clearly the

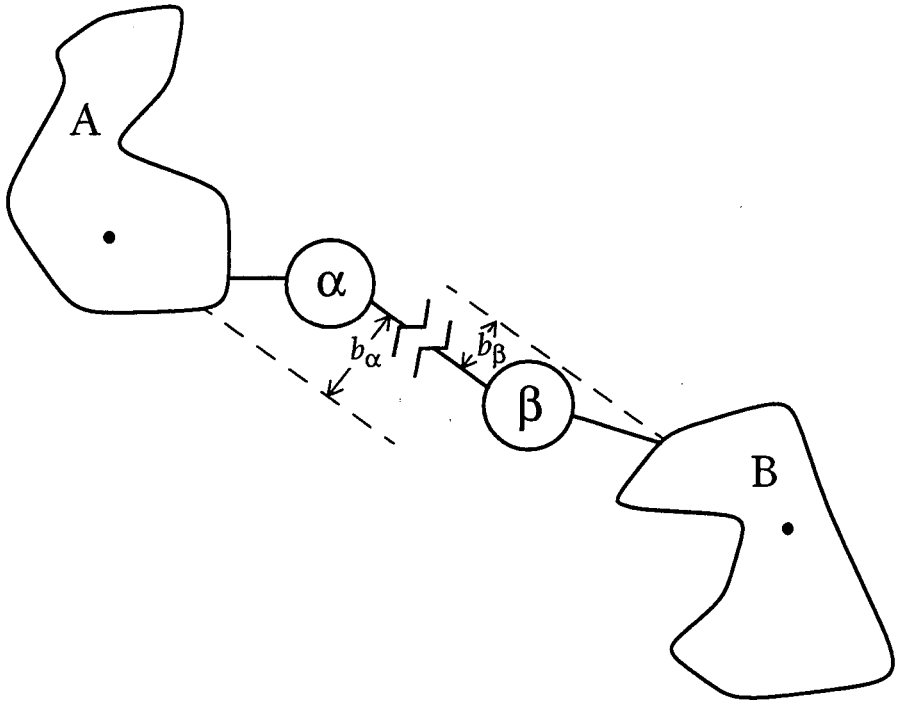

Figure 5-2. Sketch of the masses involved in the Soft-fragment impulsive model

Sketch of the bodies involved in the Soft Fragment Impulsive Model (SFIM). α and β are the 2 atoms at the ends of the bond that is breaking. These recoil and become parts of the 2 fragments, A and B. The centers of mass of the two fragments are indicated by dots.

calculation of the impact parameters requires prior knowledge of the dissociative geometry. In practice, this is usually assumed to resemble the equilibrium geometry. The

angular momenta of the atoms are conserved, evolving into fragment rotation. The resulting rotational energy of each fragment is then,

$$E_R(A) = \frac{(J_\alpha)^2}{2I_A} \tag{5-12}$$

$$E_R(B) = \frac{(J_\beta)^2}{2I_B} \tag{5-13}$$

where I_A and I_B are the moments of inertia for fragments A and B. The remaining energy in each fragment is vibrational,

$$E_V(B) = E(B) - E_T(B) - E_R(B) \tag{5-14}$$

$$E_V(A) = E(A) - E_T(A) - E_R(A) \tag{5-15}$$

5.2.2. The Rigid Fragment Limit

In the rigid fragment impulsive model (RFIM) the dissociation results in no vibrational excitation of the fragments,

$$E_V(A) = E_V(B) = 0 \tag{5-16}$$

The available energy is, therefore, partitioned only between fragment rotation and translation,

$$E_{avail} = \frac{1}{2}\mu_{AB}g^2 + \frac{(J_A)^2}{2I_A} + \frac{(J_B)^2}{2I_B} \tag{5-17}$$

$$E_{avail} = E_T(tot) + E_R(A) + E_R(B) \tag{5-18}$$

where g is the relative velocity of A and B. Since the dissociation must conserve angular momentum (initially assumed to be zero) the translational energy is constrained,

$$E_T(tot) = \frac{E_{avail}}{1 + \frac{(b_A)^2 \mu_{AB}}{I_A} + \frac{(b_B)^2 \mu_{AB}}{I_B}} \tag{5-19}$$

where b_A and b_B are the exit impact parameters (and should be equivalent to b_α and b_β above). Hence, unlike the soft fragment model, the translational energy of the products predicted by the rigid fragment model is intimately dependent on the choice of the dissociative geometry. Once the translational energy has been determined, the rotational energy of the fragments can be expressed in terms of $E_T(tot)$,

$$E_R(A) = E_T(tot) \frac{(b_A)^2 \mu_{AB}}{I_A} \tag{5-20}$$

$$E_R(B) = E_T(tot) \frac{(b_B)^2 \mu_{AB}}{I_B} \tag{5-21}$$

5.2.3. Modified Impulsive Models

There have been several attempts to increase the flexibility of the impulsive model. One, the equilibrium geometry model, takes into account the internal excitation caused by the sudden geometrical changes that occur during the dissociation. [129] This vibrational excitation can be estimated from a Franck-Condon analysis of the geometries of the dissociating parent and the separated fragments. The impulsive model calculation is then performed with this fraction removed and the final results combined. This method was successful in describing the partitioning of energy in the dissociation of NOCl into NO and Cl.

If the fraction of the available energy in product translation falls between the soft and rigid fragment impulsive models then an empirical parameter, α, can be introduced as

a measure of the "softness" of the molecule as it dissociates. [125] The "scaled-reduced-mass impulsive approximation" defines α as follows

$$\alpha = \frac{(\mu_{eff} - \mu_{\alpha\beta})}{(\mu_{AB} - \mu_{\alpha\beta})} \tag{5-22}$$

where μ_{eff} is the reduced mass that correctly predicts the fraction of energy in product translation according to equation 15. The parameter α ranges from 0 to 1 corresponding to the two limiting impulsive models. The authors also found that for the UV dissociation of alkyl halides that α=0.44 successfully predicted the correct $<E_T>$.

5.3. Statistical Models

The most well-known statistical theory of unimolecular reactions is RRKM theory, [23, 21] in which accurate reaction rates are easily obtained with minimal knowledge about the potential energy surface. RRKM theory can be extended to give reasonable RTV partitioning of products only when there is a small barrier to recombination. In this case, it is assumed that product energy distributions are similar to the distribution among T, R, and V at the critical configuration. This method makes no attempt to match up the disappearing modes in the parent molecule with rotations of the fragments, and hence underestimates the rotational and translational excitation of the products. (See Figure 5-4).

Other statistical theories predict product state distributions using information about the product states themselves. The *prior* distribution, [43] and Phase Space Theory (PST) [44] rely solely on information about the product states to partition energy. A significant problem with these methods is that they tend to overestimate product rotational excitation above the vibrational threshold [130] while underestimating product vibrations. [19] This has been understood in terms of the vibrational modes of the parent molecule that can develop asymptotically into both product rotations and vibrations. The Separate Statistical Ensembles theory (SSE) [45] attempts to correct these deficiencies by using some of the information about energy partitioning in the parent molecule

to obtain product state partitioning, but below the vibrational threshold, SSE and PST do not differ at all.

5.3.1. A new statistical method for partitioning fragment energy

The basic assumption of our method of partitioning the statistical reservoir is that the energy is distributed statistically in the *parent* molecule. The breaking of the bond is viewed as an instantaneous event, which prevents any further rearrangement of energy. Following this reasoning, it makes sense to partition the statistical energy into T, R, and V using information only from the parent, and not information from the products as in PST and the prior distribution.

The method we use to divide the statistical reservoir into T, R, and V is very similar to the way it is done in SSE. Product vibrations can develop out of all parent vibrational modes, while product rotations and translations develop only out of those modes of the parent molecule that disappear during the course of the reaction. A schematic of this idea is shown in Figure 5-3.

We utilize three ensembles. The vibrational ensemble includes all vibrational modes of the parent and overlaps with the other two ensembles. The rotational ensemble includes those disappearing modes that lead to rotational excitation of the products. These modes can include methyl torsions, skeletal bends, etc. The third ensemble is a translational ensemble that includes modes that disappear into product translations. Identification of which modes belong in which ensemble can be a subtle matter for large parent molecules, but three basic rules can be easily applied:

- Parent torsions and skeletal bends go into the "rotational" ensemble,
- Parent skeletal stretches go into the "translational" ensemble, and
- *all* parent vibrational modes go into the "vibrational" ensemble.

The energy reservoir that we are treating statistically is partitioned in the following manner:

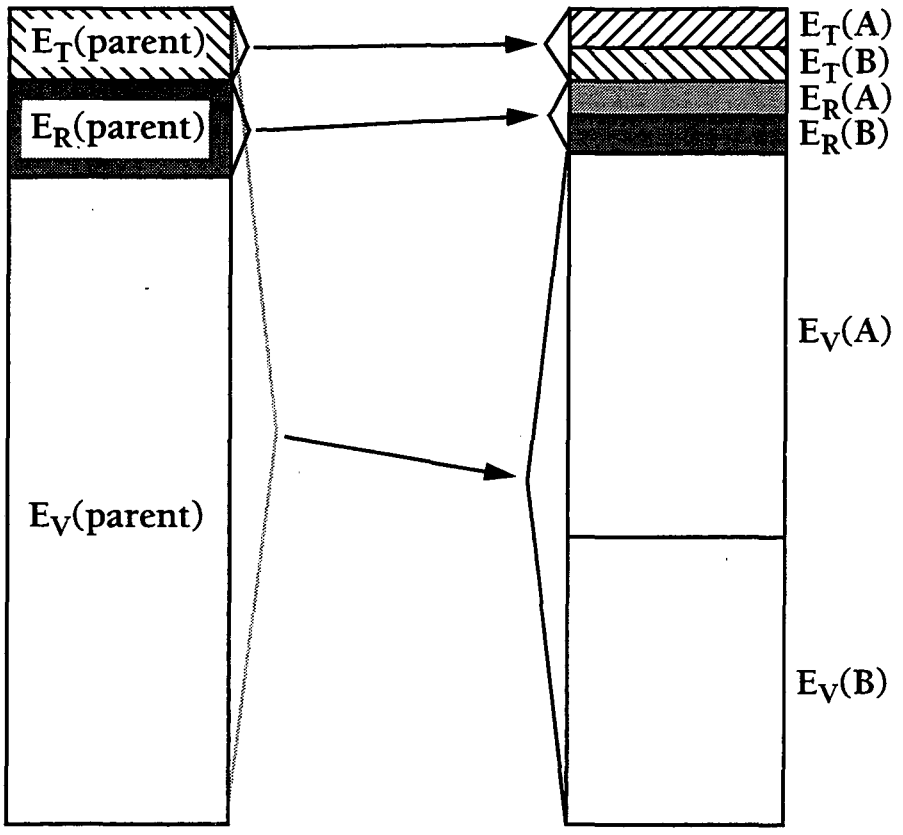

Figure 5-3. Energy partitioning in the statistical reservoir

Schematic diagram illustrating the partitioning of energy in the statistical reservoir into T, R and V of the fragments. The left side of the diagram represents the vibrational modes of the parent molecule. The shaded modes disappear during the course of the reaction. The right side of the diagram represents partitioning of energy in the fragments. All parent modes contribute to fragment vibrations, while only those modes from the T and R ensembles can contribute to fragment T and R.

$$\langle E_R^{stat} \rangle = \frac{\int_0^{E^{stat}} dE_V \int_0^{E^{stat}-E_V} dE_T \int_0^{E^{stat}-E_V-E_T} dE_R \rho_P(E_V)\rho_R(E_R)\rho_T(E_T)\delta\left(E^{stat}-E_V-E_T-E_R\right)E_R}{\int_0^{E^{stat}} dE_V \int_0^{E^{stat}-E_V} dE_T \int_0^{E^{stat}-E_V-E_T} dE_R \rho_P(E_V)\rho_R(E_R)\rho_T(E_T)\delta\left(E^{stat}-E_V-E_T-E_R\right)} \tag{5-23}$$

where ρ_P, ρ_R, and ρ_T are the densities of states for the P (parent), R, and T ensembles of parent vibrational modes. The P ensemble is made up of all vibrational modes of the parent molecule. In the harmonic approximation, the densities of states can be com-

puted easily using the Beyer-Swinehart algorithm. The expressions for $\langle E_V^{stat} \rangle$ and $\langle E_T^{stat} \rangle$ are similar to the one for the rotational energy that is given above.

Essentially, we are assuming here that the energy above the barrier is going to be distributed statistically between the three ensembles, where the ensemble for vibrations can sample from the other two ensembles. The statistics (and hence the energy distribution) are governed by the vibrational frequencies of the parent as well as a judicious choice of modes for membership in each ensemble.

Dividing $\langle E_T^{stat} \rangle$ between the two fragments is easily accomplished by conserving linear momentum:

$$E_T^{stat}(A) = \frac{\langle E_T^{stat} \rangle}{\left(1 + \frac{m_A}{m_B}\right)} \tag{5-24}$$

$$E_T^{stat}(B) = \frac{\langle E_T^{stat} \rangle}{\left(1 + \frac{m_B}{m_A}\right)} \tag{5-25}$$

$\langle E_R^{stat} \rangle$ is similarly partitioned by requiring conservation of angular momentum:

$$E_R^{stat}(A) = \frac{\langle E_R^{stat} \rangle}{\left(1 + \frac{I_A}{I_B}\right)} \tag{5-26}$$

$$E_R^{stat}(B) = \frac{\langle E_R^{stat} \rangle}{\left(1 + \frac{I_B}{I_A}\right)} \tag{5-27}$$

In these equations, the moments of inertia, I_A and I_B, are calculated by approximating both fragments are spherical tops, with moments of inertia that are the averages of the real moments of inertia for that fragment.

The only remaining difficulty is to divide the vibrational energy from the statistical reservoir between the two fragments. It seems reasonable to view the impulse as an instantaneous event, so that the energy is frozen in the parent modes. The energy in the modes that develop into fragment vibrations should then be assigned to the appropriate fragment. Identifying these modes and obtaining their frequencies seems to be impossible for all but the simplest of molecules. By approximating the frequencies of these modes by the frequencies of the fragment modes themselves, one obtains the following expression for the vibrational energy partitioned into fragment A from the statistical reservoir:

$$\langle E_V^{stat}(A)\rangle = \frac{\int_0^{E_V^{stat}} dE_A \int_0^{E_V^{stat}-E_A} dE_B \rho_A(E_A)\,\rho_B(E_B)\,\delta\left(E_V^{stat}-E_A-E_B\right)E_A}{\int_0^{E_V^{stat}} dE_A \int_0^{E_V^{stat}-E_A} dE_B \rho_A(E_A)\,\rho_B(E_B)\,\delta\left(E_V^{stat}-E_A-E_B\right)} \tag{5-28}$$

where ρ_A and ρ_B are the vibrational densities of states of fragments A and B respectively.

Partitioning of the statistical reservoir is made with a number of important assumptions. We use vibrational densities of states in the harmonic approximation, and we assume that both of the fragments can be well approximated by totally symmetric tops. The harmonic approximation to the vibrational density of states does moderately well, due in part to fortuitous cancellation of the effects of coupling and anharmonicity. Anharmonicity tends to raise the density of states at energies near the dissociation limit, and coupling between modes tends to separate nearly degenerate vibrational levels. The cancellation of the two effects makes the harmonic approximation to the density of states a reasonable approximation.

The approximation of both fragments as spherically symmetric tops is a necessary approximation if we are trying to satisfy conservation of angular momentum while being subject to the constraint of having minimal information about the geometry of the transition state. An additional approximation is that the parent is assumed to have no rotational motion prior to the dissociation, which is a good approximation for the rotationally cold conditions of most molecular beam experiments.

5.4. The Barrier Impulsive Model

In the various versions of the original impulsive model, all the available energy is released as a repulsion localized in the reaction coordinate. For the present model, the available energy for the impulsive reservoir is replaced with the height of the exit barrier. We utilize the rigid fragment impulsive model (RFIM) to partition the energy (see equations 5-16 through 5-21) from this reservoir . The two reservoirs (statistical and impulsive) are then combined to give average translational energies for the two fragments as follows:

$$E_T(A) = E_T^{stat}(A) + E_T^{imp}(A) \tag{5-29}$$

$$E_T(B) = E_T^{stat}(B) + E_T^{imp}(B) \tag{5-30}$$

Similar equations are used for rotational and vibrational energies.

5.5. Results and Discussion

In this section, we compare the predictions of the barrier impulsive model to a number of the theories discussed in the previous sections. We have chosen to focus on the energy partitioning in the α-cleavage in carbonyls excited to their $^1(n,\pi^*)$ state by absorption of an ultraviolet photon. The excitation involves the promotion of a non-bonding electron the oxygen to an anti-bonding pi orbital on the CO moiety. The molecules then dissociate over a barrier that results from an avoided crossing between the $^3(n,\pi^*)$ and $^3(\sigma,\sigma^*)$ configurations in non-planar geometries. [131] Since the dissocia-

tion ultimately involves the cleavage of only a single bond, the impulsive model can be used in a straightforward way as a repulsion along the breaking bond. In addition the transition state geometry should not be a substantial departure from the reactant geometry unlike "ring" transition states that involve multiple bonds being made and broken. This facilitates the choice of a dissociative geometry in order to obtain exit impact parameters and moments of inertia. We have chosen to perform calculations on acetone and acetic acid due to experimental data available for comparison. Additionally, the lack of measured anisotropy in the photodissociation of both of these compounds suggests that the excited state may exist for sufficient time to allow full or partial randomization of the initial excitation energy. Thus, the use of a statistical method for treating the energy in excess of the barrier is justified.

5.5.1. Acetone Dissociation

The photodissociation of acetone into CH_3CO and CH_3 has been carried out at a number of wavelengths in the ultraviolet. Although the product internal state information is far from complete, the translational energy of the photofragments has been measured at each wavelength. The excitation at 193 nm is to the 3s Rydberg state, and the molecule crosses to the $^{1,3}(n,\pi^*)$ state prior to dissociation. [132, 133]

For the impulsive reservoir of the BIM model, a barrier height of 13.4 kcal/mole was used based on the measurements of Zuckermann *et al.* [134] The rigid fragment extension, described in Section 5.2.2, was chosen with a non-planar dissociative geometry consistent with the geometry of the $^{1,3}(n,\pi^*)$ excited state. The impulse was assumed to be through the C_{3v} symmetry axis of the CH_3 group and therefore, resulted in no CH_3 rotational excitation. Both the soft fragment impulsive model (SFIM) and RFIM calculations utilized the same exit impact parameters and moments of inertia as were used in the BIM calculation. The statistical reservoir was partitioned using ground state acetone vibrational frequencies [135] as an approximation to those of the $^{1,3}(n,\pi^*)$ excited state. The assignments of the vibrational modes were also taken from Ref. 135. Of the 24 modes of acetone, 6 disappear upon dissociation, evolving into product translation and rotation. We assigned 2 of these modes the symmetric and antisymmetric C-C stretch

to the translation ensemble. Two methyl rocking modes, a methyl torsion and the C-C-C skeletal bend were assigned to the rotational ensemble. The Beyer-Swinehart algorithm was used to calculate the vibrational density of states for all ensembles. The moments of inertia for the CH_3CO fragment were determined from the *ab initio* equilibrium geometry calculated by Baird and Kathpal. [136] Vibrational frequencies were taken from RRKM calculations of Watkins and Word. [137][1]

Figure 5-4 shows the comparison of the two limiting impulsive models, SFIM and

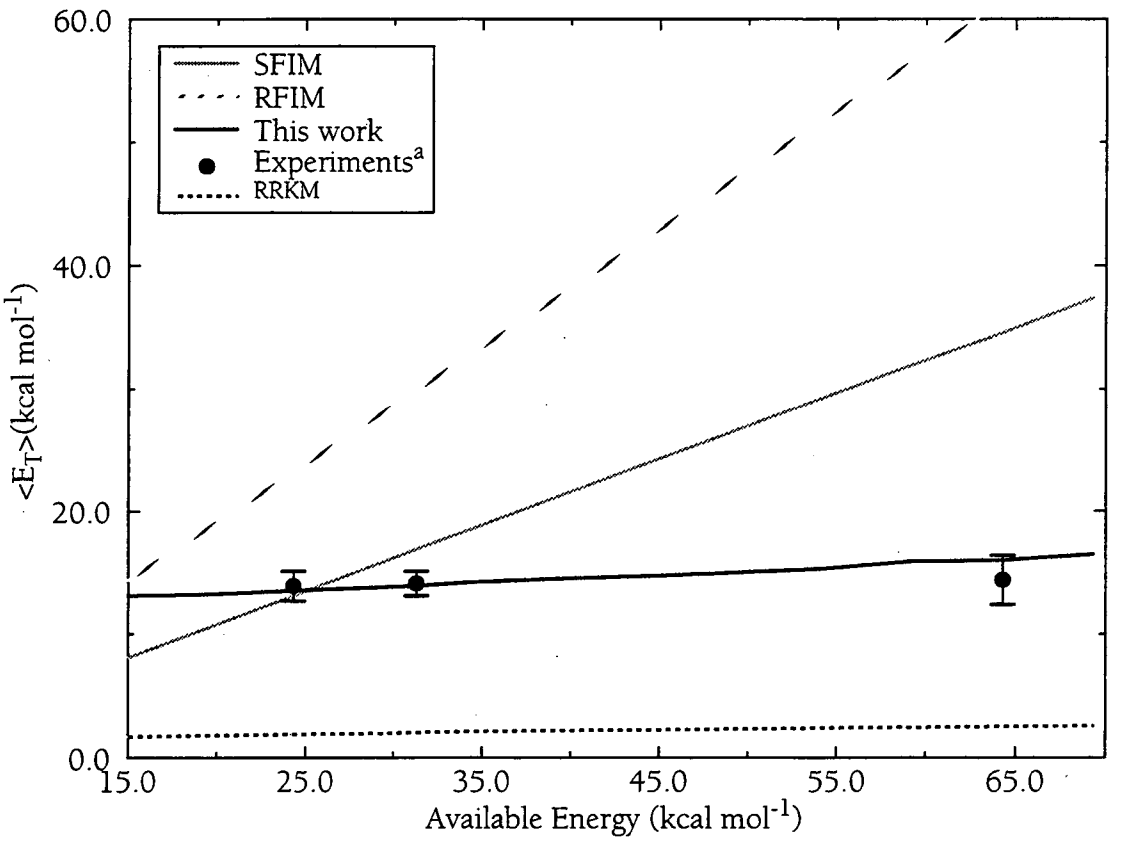

Figure 5-4. Comparison of BIM with other impulsive and statistical theories

Calculated translational energies as a function of available energy for the photodissociation of acetone. The experiments (a) are from references 119 and 120.

RFIM, and BIM with the experimentally determined average translation energies at

1. The vibrational frequencies were derived from acetaldehyde and adjusted to agree with the pre-exponential factor for the CO + CH_3 reaction.

three wavelengths. The predictions of RRKM theory is also shown as a representative barrierless statistical calculation. Both pure impulsive models rise linearly with available energy as expected. In acetone photodissociation at 266 nm (E_{avail}=23.5 kcal/mole) the average translational energy was measured to be 13.9 kcal/mole and the SFIM prediction is 12.8 kcal/mole. [121] Although the SFIM calculation underestimates $<E_T>$ at 266 nm it overestimates it at 248 nm where the SFIM predicts 16.9 kcal/mole but the experimental $<E_T>$ is only 14.1 kcal/mole. [120] At both these wavelengths the RFIM partitions far too much available energy into translation. It is interesting to note that at an available energy near 14 kcal/mole, assuming the trend continues, then the product translational energy would agree more with the RFIM prediction. The barrier impulsive model successfully predicts the magnitude of $<E_T>$ at each wavelength but also shows the correct dependence of $<E_T>$ on the available energy. There are several points worth commenting on. The first is the choice of the rigid fragment model for treating the impulsive reservoir. This suggests that the impulse is not effectively coupled into the vibrational modes of the products which is reasonable given the geometry at the transition state. Secondly, the fact that $<E_T>$ changes gradually with available energy suggests that either there is complete randomization of energy or the unrandomized energy is not localized in the reaction coordinate.

5.5.2. Acetic Acid Dissociation

The present model was also used to compare predicted energy partitioning with experimental results in the photodissociation of acetic acid at 218 nm and 200 nm. [138, 139] Both wavelengths involve $^1(n,\pi^*)$ excitation but differ by ~12 kcal/mole in the energy available for dissociation. Table 5-1 shows the BIM results and includes predictions of SFIM and RFIM. The barrier height was assumed to be 13.0 kcal/mole and the dissociative geometry was non-planar. Vibrational frequencies were taken from Herman and Hofstadter [140] with the mode assignments of Haurie and Novak. [141] The C-O(H) stretch and the COO bend were assumed to evolve into product translation while the OH torsion and rocks were partitioned into rotation. The OH and CH_3CO vibrational density of states were calculated using the method of Beyer-Swinehart.

	$E_R(OH)$	$E_V(OH)$	$E_T(OH)$	$E_{int}(CH_3CO)$	$E_T(CH_3CO)$
Experiment[a]					
218 nm	1.21[b]	<0.2	9.81	12.9	3.89
200 nm	1.36	<0.4	10.4	23.73[c]	4.11
This work					
218 nm	1.39	0.23	9.79	12.73	3.87
200 nm	2.05	0.80	10.15	22.99	4.01
RFIM					
218 nm	0.14	0	19.4	0.78	7.67
200 nm	0.21	0	27.72	1.12	10.95
SFIM					
218 nm	0.08	0.63	11.30	11.53	4.46
200 nm	0.12	0.90	16.14	16.47	6.38

Table 5-1. Comparison of theoretical predictions to experiments on Acetic Acid photodissociation

Product Energy Partitioning for Acetic Acid Photodissociation at 200 nm and 218 nm

a. References 121 and 120.
b. All energies are expressed in kcal mol^{-1}
c. Inferred from E_{avail} and all other measured quantities.

There is very good agreement between BIM and experiment. Not only does the model accurately predict the partitioning at 218 nm, high product translational energy and low OH internal excitation, but it is also consistent with the additional energy at 200 nm being deposited primarily in the ro-vibrations of the CH_3CO fragment. Although the SFIM and RFIM also predict low OH rotation and vibration they grossly overestimate the fraction of available energy appearing as product translation.

5.6. Conclusions

We have presented a simple model which allows the prediction of energy partitioning in the dissociation of polyatomics molecules that possess a substantial exit barrier. This is extremely useful in comparing average product translational energy from photofragment translational spectroscopy experiments with internal energy measurements. We expect that this model will work for systems like the two shown above that satisfy several criteria: 1) IVR should occur prior to dissociation, 2) the molecules should be large

enough to contain many modes that are not directly involved in the dissociation, and 3) the transition state should permit facile treatment of the impulsive reservoir.

6 Concluding Remarks

We conclude this dissertation by summarizing the results presented in the preceding chapters, by discussing the impact of these results on both the experimental and theoretical aspects of the field of chemical dynamics, and by suggesting future directions for research in this field.

6.1. The Zero-Point Energy Problem

We have investigated a method for correcting the zero-point energy (ZPE) problem in classical trajectory simulations and have found that the method introduces some problems into the dynamics, making it impractical for use in simulations of reactive systems. The most noticeable effect of the BMH method is what it does to the power spectra of trajectories that have violated the ZPE conditions. Another troubling aspect of the BMH method is that it can mis-identify surfaces which are nearly flat following the inflection points after a barrier as harmonic wells with zero-point energy above the true barrier height. The falsely-identified well can restrict reactive trajectories (that satisfy the ZPE in all other vibrational modes) from continuing on into the product valley. Although the problem is most apparent in systems with very low masses, it is possible that a chemically relevant potential energy surface could exhibit the same behavior when used with BMH trajectory simulations.

Our feeling is that all methods that utilize local information about the potential energy surface (first and second derivatives) in an attempt to correct for what is really a global phenomenon on the surface will suffer similar deficiencies. We do not hold out much

hope for a solution to the ZPE problem that actively modifies the classical equations of motion for individual trajectories. It seems that a solution for the problem lies either in a mixed semiclassical/classical method like the one proposed by Alimi *et al.* [142], or in a rethinking of how initial conditions are sampled and how final conditions for the ensemble of trajectories are analyzed. There is still debate on whether the ZPE problem is simply an artifact of how we perform these aspects of classical simulations, and until the problem is well understood, solutions to the problem will be appropriate for only a limited set of situations.

6.2. The Unimolecular Reactions of Ketene

In Chapters 3 and 4, we developed reduced dimensionality models for the isomerization of ketene via the stable oxirene structure, and for the dissociation of triplet ketene over a barrier to form ${}^3B_1\ CH_2 + {}^1\Sigma^+\ CO$. In both of these reactions, the reactant is highly vibrationally excited (but rotationally cold) ketene prepared by exciting ground-state ketene to the first excited singlet state and allowing it to undergo internal conversion or intersystem crossing onto the appropriate electronic surface. The quantum microcanonical rates for both reactions were obtained rigorously (for the active degrees of freedom within the barrier region) using methodology developed by Miller *et al.* over the past few years. The uncoupled degrees of freedom were treated separately (either as harmonic oscillators, or within an appropriate basis-set).

The Absorbing Boundary Conditions (ABC) developed by Seideman and Miller [31] allowed us to construct a Green's function with the correct outgoing wave boundary conditions by absorbing all flux which leaves the barrier region on the surface. A negative imaginary potential is added to a grid representation of the Hamiltonian, making it possible to calculate the cumulative reaction probability *directly*, i.e. without calculating all of the state-to-state reaction amplitudes in the S-matrix. This made performing the calculation of ketene isomerization rates a feasible undertaking because the asymptotic (ketene) regions of the potential energy surface support millions of states at the energies of interest. This would have prevented us from using the earlier methods for reactive scattering based on the Kohn variational principle. [29, 30]

A second technical development that contributed to the feasibility of these calculations was the grid-based discrete variable representation (DVR) developed by Colbert and Miller. [32] A DVR of the ABC Hamiltonian is sparse in multiple degrees-of-freedom, allowing us to use some of the newly developed techniques (such as QMR [36]) for inverting and diagonalizing sparse linear systems.

The advance that made it possible to complete these calculations within a graduate career was introduced by Manthe and Miller [37] in the form of a reaction probability operator, $\hat{P}(E)$. This operator has only a few non-zero eigenvalues corresponding to reaction probabilities for individual vibrational levels of the transition state. The great advantage of this property is that the iterative Lanczos technique [38, 39, 40] can be applied to find the eigenvalues of $\hat{P}(E)$ very efficiently. For large grids with small cumulative reaction probabilities, this saves great amounts of computer time.

The calculated microcanonical rates presented in chapters 3 and 4 exhibited good qualitative agreement with the experiments performed by Moore and co-workers. We were able to say with some certainty that the features in the energy dependence of the rate of ketene isomerization are due to a combination of overlapping tunneling and Feshbach resonances in a strongly bent region on the potential energy surface. Our calculations showed many narrow resonances at energies below the experimental energies, and a combination of narrow (tunneling) and wide (Feshbach) resonances at experimentally relevant energies. The poor agreement between the exact energies, amplitudes and widths of the resonant features is probably a result of a poor model for the true potential energy surface. However, it would be very interesting to see what the experiments show at energies below the barrier to ketene dissociation (the current low energy limit). This would help us to refine the potential energy surface for future calculations.

In the microcanonical rate for the dissociation of triplet ketene, we saw good overall agreement with the experimental rates, but were missing the step-like features that are apparent in the energy dependence of the experimental rates. We were able to recover the step-like features by using a barrier frequency four times lower than the one pre-

dicted by *ab initio* calculations. A two degree-of-freedom calculation was performed to find out if coupling between the CCO bend and the reaction coordinate could give rise to the steps, but the results were essentially unchanged from the one degree-of-freedom calculation. Once again, we were forced to conclude that we either have a poor model for the true potential energy surface, or that there are additional features on the surface that have not yet been discovered by the *ab initio* groups.

6.3. The Barrier Impulsive Model

In Chapter 5, we developed a simple model for partitioning energy between rotational, vibrational and translational degrees of freedom in the unimolecular dissociations of large molecules. It was designed for reactions where the reaction coordinate primarily involves the rupture of a single bond. The model simplifies to the impulsive model when the available energy is just enough to clear the transition state, and simplifies to an SSE-like [45] statistical model in the absence of a barrier to recombination. Agreement of this model with experimental data is excellent, and the information that is traditionally available for these kinds of reactions (energies, frequencies, and geometries of the parent molecule, transition state, and fragments) is all that is required to make predictions. It has already proven itself quite useful in settling a dispute over the stepwise or concerted nature of the dissociation of Acetone into $2CH_3 + CO$, [119] and performed quite well against the impulsive [41, 42] and prior [43] models in predicting the vibrational energy in the CO fragment of the 193 nm photodissociation reactions of $(CH_3)_2CO$ and $(C_2H_5)_2CO$. [143]

The Barrier Impulsive Model was developed to give "coarse grained" details about the partitioning of energy in the products of the dissociation of large molecules. This is most useful when comparing to the average product translational energy from photofragment translational spectroscopy experiments. In these experiments, the barrier impulsive model can be used with the product translational distribution to learn something about internal energy distribution within the fragments.

6.4. Future Directions

We view this dissertation as an early exploration of the kinds of model building and approximate theory construction that chemical dynamicists will have to engage in as we move towards larger reactions with more atoms in each molecule. We would like to leave the reader with our thoughts on three directions for future work that are suggested by the calculations reported in this dissertation.

6.4.1. On Potential Energy Surfaces

Perhaps the most disappointing and educational aspect of the work on ketene is our dependence on good *ab initio* surfaces on which to calculate the dynamical quantities of interest. The energy dependence of the rate of ketene isomerization is strongly dependent on the coupling between the active degrees of freedom, and the geometry and energy of the outer transition state can greatly influence the spacing of the tunnelling resonances observed in our calculations. In the calculations of the rate of dissociation for ketene on it's triplet surface, the *ab initio* barrier frequency appeared to be four times as large as what we would expect from the appearance of step-like features in the experimental rates. These deficiencies point either to *ab initio* results that didn't accurately represent the geometries, energies, and frequencies at the structures of interest, or they highlight serious problems in how we construct surfaces from the *ab initio* data.

When we use a potential energy surface, that surface has come to us via a grid of points in the coordinate space of the molecule. The traditional and well-known surfaces (particularly for small reactions) are built by fitting functional forms which have the correct behavior to this grid of energies in coordinate space.

For larger reactions, the information communicated to us from *ab initio* chemists is in the form of geometries, energies and frequencies at a very small number of critical points (local minima, transition states, global minima, etc.). The frequencies are typically obtained via finite difference methods in a small grid of configurations surrounding these critical points. In cases where the locations of the critical points are not known, grids are used to search for them. Once we have the information at the critical points,

we again utilize functional forms that have the correct behavior and fit the energies, frequencies, and geometries of critical points these functional forms to the *ab initio* information.

What strikes us most about this whole process is that within the DVR-ABC methodology, we take energies at a grid of configurations, fit them to a functional form (and introduce substantial errors in the process), and then use the functional form to obtain energies at another grid of configurations. It would seem that there is at least one unnecessary step in this process. Given the recent increases in the speed of some kinds of *ab initio* calculations (particularly the work of White and Head-Gordon [144, 145]), it would be of particular interest to do away with the surface fitting altogether, and simply calculate the potential energy directly at every grid point in the DVR grid. It would be of great intellectual interest to be able to calculate reaction rates rigorously from first principles where the only approximation is the Born-Oppenheimer approximation.

Alternatively, M.A. Collins [146, 147] has proposed a simple method for placing *ab initio* calculations at configurations where a dynamicist would be most interested in having knowledge of the surface. The surface is interpolated between the known *ab initio* energies, and a very high-quality surface is obtained without fitting, and with relatively few *ab initio* calculations. The attraction of both methods is the absence of the surface-fitting step which has given such unsatisfactory results in the past.

6.4.2. Approximate Theories

Now that experiments are performed on larger molecules than those with just a few atoms, it is becoming less useful to collect or understand the huge amount of detailed state-to-state information available for these reactions. Often the experiments will simply measure broad translational energy distributions or the vibrational and rotational temperatures of the product molecules. For very large systems, spectra which are not assignable and which have broad overlapping features may be all the experimental data that is available.

The ABC methodology allows us to calculate averaged quantities like the thermal rate directly, without summing or averaging over initial or final states. Indeed, this has been a great leap forward in the utility of quantum mechanical calculations of dynamical quantities. However, experimental chemical dynamics seems to be moving on to systems for which exact quantum calculations would be next to impossible. Photofragment translational spectroscopy has been used to obtain information of the photodissociation of acetone (with 24 vibrational degrees of freedom), and diethyl ketone (with 42 vibrational degrees of freedom). What would be of great use to the experimentalists carrying out these reactions are approximate theories to increase their understanding of how energy is partitioned in the fragments following the dissociation event.

To date, the approximate theories in use by experimentalists (including the barrier impulsive model presented in this dissertation), are fairly crude and have only limited applicability. Further refinements of these theories would be of great use to many experimental gas phase chemists. Similar theories would also be useful in predicting averaged quantities for large bi-molecular reactions, and for reactions that involve substantial molecular rearrangements during the course of the reaction.

6.4.3. Reduced Dimensionality Models

As theoretical chemists push towards understanding the dynamics of larger and larger systems, we are going to have to develop reduced dimensionality methods not only for quantum mechanical calculations, but also for *classical* simulations of biologically interesting reactions. The challenge of reduced dimensionality models is in knowing which modes to fix or average over, and which modes capture most of the essential aspects of the reaction coordinate. A clever choice of coordinate systems can sometimes make this task easier than it is in other coordinate systems.

There is currently a great deal of interest in developing methods to study the structure and dynamics of protein chains. The standard methods of simulating classical molecular dynamics require integration time steps that are many times smaller than the time scale of highest frequency motion in the protein, while the actual folding dynamics is thought

to take place in times that are several orders of magnitude longer than this time scale. [148] A few methods have been introduced for performing the simulations in a subspace of the full dimensionality, [149] but a coordinate system that aids in the choice of the "important" degrees of freedom has not yet been developed.

If one wishes to understand the quantum mechanics of very large coupled systems (like proteins or clusters), then approximate methods for separating the active degrees of freedom from the rest of the problem must be developed. Jungwirth and Gerber have proposed a mixed classical-quantum method for doing time-dependent quantum dynamics on separable potentials obtained from trajectory simulations. [150, 151] Their method builds the coupling (obtained classically) into separable time-dependent potential energy surfaces for each vibrational mode, and uses TD-SCF to propagate the one-dimensional wave function on these surfaces.

Both methods described above are currently limited in their applicability to relatively stiff systems where the normal modes are good descriptions of the full motion of the molecules under consideration. An extension of either of these methods to reactive systems, or to "floppy" molecules will greatly aid in the push to understand the dynamics of complex chemical systems.

The coming years will be exciting times at the triple point between biology, physics and chemistry. One of the most important areas of research at this junction will be the application of the principles of chemical reaction dynamics to biologically relevant reactions, and I look forward with great excitement to future developments in this field.

Bibliography

[1] J.I. Steinfeld, J.S. Francisco, and W.L. Hase, *Chemical Kinetics and Dynamics*, (Prentice Hall, Englewood Cliffs, New Jersy, 1989).

[2] R.N. Porter and L.M. Raff, "Classical Trajectory Methods in Molecular Collisions," in *Dynamics of Molecular Collisions, Part B*, W. H. Miller, ed., pages 1–52, (Plenum Press, New York, 1976).

[3] N. Cartwright, *How the Laws of Physics Lie*, (Oxford University Press, New York, 1983).

[4] I. Hacking, *Representing and intervening: Introductory topics in the philosophy of natural science*, (Cambridge University Press, New York, 1983).

[5] P.M. Churchland, "The Ontological Status of Observables: In praise of Superempirical Virtues," in *Images of Science: Essays on Realism and Empiricism*, (University of Chicago Press, Chicago, 1985).

[6] B. Van Fraassen, *The Scientific Image*, (Clarendon Press, New York, 1980).

[7] S.M. Auerbach, *Modern Integral Equation Techniques for Quantum Reactive Scattering Theory*, PhD thesis, (University of California at Berkeley, 1993).

[8] Y.T. Lee, *Science* **236**(4803), 793–8 (1987).

[9] D.M. Neumark *et al.*, *J. Chem. Phys.* **82**, 3045 (1985).

[10] Sang Kyu Kim, E.R. Lovejoy, and C.B. Moore, *J. Chem. Phys.* **102**(8), 3202–19 (1995).

[11] E.R. Lovejoy, Sang Kyu Kim, and C.B. Moore, *Science* **256**, 1541–4 (1992).

[12] E.R. Lovejoy and C.B. Moore, *J. Chem. Phys.* **98**(10), 7846–54 (1993).

[13] E.R. Lovejoy, S.K. Kim, R.A. Alvarez, and C.B. Moore, *J. Chem. Phys.* 95(6), 4081–4093 (1991).

[14] I. Garcia-Moreno, E.R. Lovejoy, and C.B. Moore, *J. Chem. Phys.* 100(12), 8890–8901 (1994).

[15] I. Garcia-Moreno, E.R. Lovejoy, and C.B. Moore, *J. Chem. Phys.* 100(12), 8902–6 (1994).

[16] W.H. Green, A.J. Mahoney, Qi-Ke Zheng, and C.B. Moore, *J. Chem. Phys.* 94(3), 1961–9 (1991).

[17] I.C. Chen and C.B. Moore, *J. Chem. Phys.* 94(1), 263–269 (1990).

[18] I.C. Chen and C.B. Moore, *J. Chem. Phys.* 94(1), 269–274 (1990).

[19] S. K. Kim, Y. S. Choi, C. D. Pibel, Q. Zheng, and C. B. Moore, *J. Chem. Phys.* 94(3), 1954–60 (1991).

[20] R.G. Gilbert and S.C. Smith, *Theory of unimolecular and recombination reactions*, (Blackwell Scientific Publications, Boston, 1990).

[21] P.J. Robinson and K.A. Holbrook, *Unimolecular Reactions*, (Wiley-Interscience, New York, 1972).

[22] I.W.M. Smith, *Kinetics and Dynamics of Elementary Gas Phase Reactions*, (Butterworths, Boston, 1980).

[23] W. Forst, *Theory of Unimolecular Reactions*, (Academic, New York, 1973).

[24] J.M. Bowman, *J. Chem. Phys.* 95(13), 4960–4968 (1991).

[25] W.H. Miller, *J. Am. Chem. Soc.* 101, 6810 (1979).

[26] J.M. Bowman, B. Gazdy, and Q. Sun, *J. Chem. Phys.* 91(5), 2859–2862 (1989).

[27] W. H. Miller, W. L. Hase, and C. L. Darling, *J. Chem. Phys.* 91(5), 2863–8 (1989).

[28] B.R. Johnson, National resource for computation in chemistry. In *NRCC Proceedings*, number 5, page 86, (University of California, Berkeley, 1979).

[29] J.Z.H. Zhang, S.-I. Chu, and W.H. Miller, *J. Chem. Phys.* 88(10), 6233–9 (1988).

[30] J.Z.H. Zhang and W.H. Miller, *J. Chem. Phys.* 91(3), 1528–47 (1989).

[31] T. Seideman and W.H. Miller, *J. Chem. Phys.* 97(4), 2499–2514 (1992).

[32] D.T. Colbert and W.H. Miller, *J. Chem. Phys.* 96(3), 1982–91 (1992).

[33] D.O. Harris, G.G. Engerholm, and W.D. Gwinn, *J. Chem. Phys.* **43**, 1515 (1965).

[34] J.C. Light, I.P. Hamilton, and J.V. Lill, *J. Chem. Phys.* **82**(3), 1400–9 (1985).

[35] Y. Saad and M.H. Schultz, *SIAM J. Sci. Stat. Comput.* 7(3), 856–69 (1986).

[36] R.W. Freund, *SIAM J. Sci. Stat. Comput.* **13**(1), 425–48 (1992).

[37] U. Manthe, T. Seideman, and W.H. Miller, *J. Chem. Phys.* **101**(6), 4759–68 (1994).

[38] J.H. Wilkinson and C. Reinsch, "Linear algebra," in F. L. Bauer, editor, *Handbook for automatic computation*, volume 2, (Springer-Verlag, New York, 1971).

[39] C. Lanczos, *J. Res. Natl. Bur. Stand.* **45**, 255 (1950).

[40] J.K. Cullum and R.A. Willoughby. *Lanczos algorithms for large symmetric eigenvalue computations*, volume 3 of *Progress in scientific computing*, (Birkhauser, Boston, 1985).

[41] G.E. Busch and K.R. Wilson, *J. Chem. Phys.* **56**, 3626 (1972).

[42] A.F. Tuck, *Journal of the Chemical Society, Faraday Transactions* **73**, 689 (1977).

[43] R.D. Levine and J.L. Kinsey, In R.B. Bernstein, editor, *Atom-Molecular Collision Theory - A Guide for the Experimentalist*, (Plenum, New York, 1979).

[44] P. Pechukas and J. C. Light, *J. Chem. Phys.* **42**, 3281 (1965).

[45] C. Wittig, I. Nadler, H. Reisler, M. Noble, J. Catanzarite, and G. Radhakrishnan, *J. Chem. Phys.* **83**, 5581 (1985).

[46] M. Hénon and C. Heiles, *Astron. J.* **69**, 73 (1964).

[47] J.M. Bowman, G.C. Schatz, and A. Kuppermann, *Chem. Phys. Lett.* **24**, 378 (1974).

[48] G. Baym, *Lecutres on Quantum Mechanics*, (Addison-Wesley, Menlo Park, CA, 1990).

[49] J.J. Sakurai, *Modern Quantum Mechanics*, (Addison-Wesley Publishing Company, Inc., Redwood City, California, 1985).

[50] T. Uzer, B.D. MacDonald, Y. Guan, and D.L. Thompson, *Chem. Phys. Lett.* **152**(4-5), 405–8 (1988).

[51] Y. Guan, T. Uzer, B.D. MacDonald, and D.L. Thompson, "Dissociation of overtone-excited hydrogen peroxide near threshold; a quasiclassical trajectory study," in J.M. Bowman and M. Ratner, editors, *Advances in Molecular Vibrations and Collision Dynamics*, volume 1B, pages 81–104, (JAI Press, Greenwich CT, 1991).

[52] H.-R. Dubal and F.F. Crim, *J. Chem. Phys.* **83**(8), 3863–72 (1985).

[53] T.M. Ticich, T.R. Rizzo, H.-R. Dubal, and F.F. Crim, *J. Chem. Phys.* **84**(3), 1508–20 (1986).

[54] D. Lu and W.L. Hase, *J. Chem. Phys.* **89**(11), 6723–35 (1988).

[55] W.L. Hase and D.G. Buckowski, *J. Comput. Chem.* **3**(3), 335–343 (1982).

[56] O.K. Rice and H.C. Ramsperger, *J. Am. Chem. Soc.* **50**, 617 (1928).

[57] L.S. Kassel, *J. Phys. Chem.* **32**, 1065 (1928).

[58] R.A. Marcus and O.K. Rice, *J. Phys. Colloid Chem.* **55**, 894 (1951).

[59] R.A. Marcus, *J. Chem. Phys.* **20**, 359 (1952).

[60] D. Lu and W.L. Hase, *J. Chem. Phys.* **91**(12), 7490–7 (1989).

[61] G. Nyman and J. Davidsson, *J. Chem. Phys.* **92**(4), 2415–22 (1990).

[62] R.C. Brown and E.J. Heller, *J. Chem. Phys.* **75**(1), 186–8 (1981).

[63] J.C. Gray and D.G. Truhlar, *J. Chem. Phys.* **76**(11), 5350–5 (1982).

[64] H.-W. Lee and M.O. Scully, *J. Chem. Phys.* **77**(9), 4604–10 (1982).

[65] V.M. Azriel, G.D. Billing, L.Y. Rusin, and M.B. Sevryuk, *Chem. Phys.* **195**(1-3), 243–258 (1995).

[66] M.C. Gutzwiller, *Chaos in Classical and Quantum Mechanics*, (Springer-Verlag , New York, 1990).

[67] W.H. Miller, N.C. Handy, and J.E. Adams, *J. Chem. Phys.* **72**(1), 99–112 (1980).

[68] B.A. Waite and W.H. Miller, *J. Chem. Phys.* **73**, 3713 (1980).

[69] D.M. Neumark, A.M. Wodtke, G.N Robinson, C.C. Hayden, K. Shobatake, R.K. Sparks, T.P. Schafer, and Y.T. Lee, *J. Chem. Phys.* **82**, 3067 (1985).

[70] D.M. Neumark, A.M. Wodtke, G.N. Robinson, C.C. Hayden, and Y.T. Lee, *J. Chem. Phys.* **82**, 3045 (1985).

[71] J.T. Muckerman, *J. Chem. Phys.* 54(3), 1155–1164 (1971).

[72] R. Steckler, D.G. Truhlar, and B.C. Garrett, *J. Chem. Phys.* 82, 5499–5505 (1985).

[73] G.C. Lynch, R. Steckler, D.W. Schwenke, A.J.C. Varandas, et al., *J. Chem. Phys.* 94(11), 7136–7149 (1991).

[74] C.A. Parr and D.G. Truhlar, *J. Phys. Chem.* 75, 1844 (1971).

[75] F. London, "Probleme der modernen physik," in *Sommerfeld Festschrift*, page 104 (1928).

[76] S. Sato, *J. Chem. Phys.* 23, 592 (1955).

[77] P.J. Kuntz, E.M. Nemeth, J.C. Polanyi, S.D. Rosner, and C.E. Young, *J. Chem. Phys.* 44, 1168 (1966).

[78] H.F. Schaefer III, *J. Phys. Chem.* 89, 5336 (1985).

[79] S. Flugge, *Practical Quantum Mechanics*, volume 1, (Springer-Verlag, New York, 1971).

[80] M. Karplus and R.N. Porter, *Atoms & Molecules: An Introduction For Students of Physical Chemistry*, (Benjamin Cummings, Menlo Park, 1970).

[81] G.H. Peslherbe and W.L. Hase, *J. Chem. Phys.* 100(2), 1179–89 (1994).

[82] K.F. Lim and D.A. McCormack, *J. Chem. Phys.* 102(4), 1705–1715 (1995).

[83] D.A. McCormack and K.F. Lim, *J. Chem. Phys.* 103(5), 1991–1992 (1995).

[84] A.P. Scott, R.H. Nobes, H.F. Schaefer, and L. Radom, *J. Am. Chem. Soc.*, 116(22), 10159–10164 (1994).

[85] G. Vacek, J.M. Galbraith, Y. Yamaguchi, H.F. Schaefer, *et al.*, *J. Phys. Chem.* 98(35), 8660–8665 (1994).

[86] H. Eyring, *J. Chem. Phys.* 3, 107 (1935).

[87] M.G. Evans and M. Polanyi, *Trans. Faraday Soc.* 31, 875 (1935).

[88] W.H. Miller, *Ann. Rev. Phys. Chem.* 41, 245 (1990).

[89] Y.S.M. Wu and A. Kuppermann, *Chem. Phys. Lett.* 205(6), 577–586 (1993).

[90] C.C. Chou and F.S. Rowland, *J. Chem. Phys.* 50(12), 5133–40 (1969).

[91] K. Tanaka and M. Yoshimine, *J. Am. Chem. Soc.* 102, 7655 (1980).

[92] W. J. Bouma et al., *J. Org. Chem.* 47, 1869 (1982).

[93] L. Wolff, *Justus Liebigs Ann. Chem.* **325**, 129 (1902).

[94] L. Wolff, *Justus Liebigs Ann. Chem.* **394**, 23 (1912).

[95] I.G. Csizmadia, J. Font, and O.P. Strausz, *J. Am. Chem. Soc.* **90**, 7360 (1968).

[96] D.E. Thornton, R.K. Gosavi, and O.P. Strausz, *J. Am. Chem. Soc.* **92**, 1768 (1970).

[97] K.-P. Zeller, *Angew. Chem. Int. Ed. Engl.* **11**, 781 (1977).

[98] G.Z. Whitten and B.S. Rabinovitch, *J. Chem. Phys.* **41**, 1883 (1964).

[99] D.C. Tardy, B.S. Rabinovitch, and G.Z. Whitten, *J. Chem. Phys.* **48**, 1427 (1968).

[100] J.V. Michael, J.R. Fisher, J.M. Bowman, and Q.Y. Sun, *Science* **249**(4966), 269–271 (1990).

[101] S. Takada, A. Ohsaki, and H. Nakamura, *J. Chem. Phys.* **96**(1), 339–48 (1992).

[102] S.M. Auerbach and W.H. Miller, *J. Chem. Phys.* **100**(2), 1103–12 (1994).

[103] N.C. Handy, private communication.

[104] T. Seideman and W.H. Miller, *J. Chem. Phys.* **96**(6), 4412–22 (1992).

[105] T. Seideman and W.H. Miller, *J. Chem. Phys.* **97**(4), 2499–2514 (1992).

[106] W.H. Miller and T. Seideman, in J. Broeckhove and L. Lathouwers, editors, *Time-dependent quantum molecular dynamics*, volume 299, NATO ARW, (Plenum, New York, 1992).

[107] W.H. Thompson and W.H. Miller, *Chem. Phys. Lett.* **206**, 123–129 (1993).

[108] D. Baxter, J. Saltz, M. Schultz, S. Eisenstat, *et al*, "An experimental study of methods for parallel preconditioned Krylov methods," in G. Fox, editor, *Third Conference on Hypercube Concurrent Computers and Applications*, volume 2, pages 1698–711, (ACM, New York, 1988).

[109] H.O. Karlsson, *J. Chem. Phys.* **103**(12), 4914–4919 (1995).

[110] J. R. Taylor, *Scattering Theory: the Quantum theory on nonrelativistic collisions*, (Wiley, New York, 1972).

[111] W.D. Allen and H.F. Schaefer III, unpublished results.

[112] W.D. Allen and H.F. Schaefer III, *J. Chem. Phys.* **89**(1), 329–44 (1988).

[113] J.D. Gezelter and W.H. Miller, *J. Chem. Phys.* **103**(18), 7868 (1995).

[114] C.E. Klots, *J. Phys. Chem.* **75**, 1526 (1971).

[115] G. Brocks, A. van der Avoird, B.T. Sutcliffe, and J. Tennyson, *Mol. Phys.* **50**(5), 1025–43 (1983).

[116] P.A. Stockman, R.E. Bumgarner, S. Suzuki, and G.A. Blake, *J. Chem. Phys.* **96**(4), 2496–510 (1992).

[117] H.S. Johnston, *Gas Phase Reaction Rate Theory*, (Ronald Press Company, New York, 1966).

[118] J. Troe and C.B. Moore, communicated to the author by C.B. Moore.

[119] S.W. North, D.A. Blank, J.D. Gezelter, C.A. Longfellow, and Y.T. Lee, *J. Chem. Phys.* **102**(11), 4447–4460 (1995).

[120] S.W. North, C.A. Longfellow, and Y.T.Lee, unpublished results.

[121] G. Hancock and K.R. Wilson, in the *Fourth International Symposium on Molecular Beams*, Cannes France (1973).

[122] X. Zhao, W.B. Miller, E.J. Hintsa, and Y.T. Lee, *J. Chem. Phys.* **90**(10), 5527 (1989).

[123] X. Zhao, E.J. Hintsa, and Y.T. Lee, *J. Chem. Phys.* **88**, 801 (1988).

[124] D. Krajnovich, F. Huisken, Z. Zhang, Y.R. Shan, and Y.T. Lee, *J. Chem. Phys.* **77**, 5977 (1982).

[125] A.M. Wodtke, E.J. Hintsa, and Y.T. Lee, *J. Chem. Phys.* **90**, 3549 (1986).

[126] L.J. Butler, R.J. Buss, R.J. Brudzynski, and Y.T. Lee, *J. Chem. Phys.* **87**, 5106 (1983).

[127] S.J. Riley and K.R. Wilson, *Faraday Discuss. Chem. Soc.* **53**, 132 (1972).

[128] K.E. Holdy, L.C. Klotz, and K.R. Wilson, *J. Chem. Phys.* **52**, 4588 (1970).

[129] R.C. Mitchell and J.P. Simons, *Disc. Faraday Soc.* **44**, 208 (1967).

[130] I. Nadler, M. Noble, H. Reisler, and C. Wittig, *J. Chem. Phys.* **82**, 2608 (1985).

[131] M. Reinsch and M. Klessinger, *J. Phys. Org. Chem.* **3**, 81 (1990).

[132] G.A. Gaines, D.J. Donaldson, S.J. Strickler, and V.Vaida, *J. Phys. Chem.* **92**, 2762 (1988).

[133] D.J. Donaldson, G.A. Gaines, and V.Vaida, *J. Phys. Chem.* 92, 2766 (1988).

[134] H. Zuckermann, B. Schmitz, and Y. Haas, *J. Phys. Chem.* 92, 4835 (1988).

[135] P. Cossee and J.H. Schachtschneider, *J. Chem. Phys.* 44(1), 97 (1966).

[136] N.C. Baird and H.B. Kathpal, *Canadian Journal of Chemistry* 55, 863 (1977).

[137] K.W. Watkins and W.W. Word, *International Journal of Chemical Kinetics* 6, 855 (1974).

[138] S.S. Hunnicutt, L.D. Waits, and J.A. Guest, *J. Phys. Chem.* 93, 5188 (1989).

[139] S.S. Hunnicutt, L.D. Waits, and J.A. Guest, *J. Phys. Chem.* 95, 562 (1991).

[140] R.C. Hermen and R. Hofstadter, *J. Chem. Phys.* 7, 460 (1939).

[141] M. Haurie and A. Novak, *Spectrachimica Acta* 21, 1217 (1965).

[142] R. Alimi, A. Garcia-Vela, and R.B. Gerber, *J. Chem. Phys.* 96(3), 2034–8 (1992).

[143] G.E. Hall, H.W. Metzler, J.T. Muckerman, J.M. Preses, and R.E. Weston Jr., *J. Chem. Phys.* 102(17), 6660–8 (1995).

[144] C.A. White and M. Head-Gordon, *J. Chem. Phys.* 101(8), 6593–6605 (1994).

[145] C.A. White and M. Head-Gordon, *Chem. Phys. Lett.* 230(1-2), 8–16 (1994).

[146] J. Ischtwan and M.A. Collins, *J. Chem. Phys.* 100(11), 8080–8 (1994).

[147] M.J.T. Jordan, K.C. Thompson, and M.A. Collins, *J. Chem. Phys.* 102(14), 5647–57 (1995).

[148] T.E. Creighton, *Protein Folding*, (W.H. Freeman and Company, New York, 1992).

[149] A. Askar, B. Space, and H. Rabitz, *J. Phys. Chem.* 99(19), 7330–7338 (1995).

[150] P. Jungwirth and R.B. Gerber, *J. Chem. Phys.* 102(15), 6046–56 (1995).

[151] P. Jungwirth and R.B. Gerber, *J. Chem. Phys.* 102(22), 8855–64 (1995).

LAWRENCE BERKELEY NATIONAL LABORATORY
UNIVERSITY OF CALIFORNIA
TECHNICAL & ELECTRONIC INFORMATION DEPARTMENT
BERKELEY, CALIFORNIA 94720